

Investigations on the Mechanisms of Ultrasonic Wire Bonding

Von der Fakultät für Maschinenbau
der Gottfried Wilhelm Leibniz Universität Hannover
zur Erlangung des akademischen Grades
Doktor-Ingenieur
genehmigte

Dissertation

von
Yangyang Long
geb. am 07. Februar 1988 in Shandong

2019

1. Referent: Prof. Dr.-Ing. Jörg Wallaschek
2. Referent: Prof. Dr.-Ing. Hans Jürgen Maier
3. Referent: Prof. Dr.-Ing. Ludger Overmeyer

Tag der Promotion: 23. April 2019

Preface

This dissertation was completed during my time at the Institute of Dynamics and Vibration Research (IDS), Leibniz Universität Hannover, Germany. Here I would like to express my great thankfulness to the head of the institute - Prof. Dr.-Ing. Jörg Wallaschek. Thanks to him for giving me the chance to conduct my research on such an interesting topic at this great-equipped, well-collaborated and advanced institute in a relaxed atmosphere. I would also thank him for his supervision and continuous encouragements to me. Without his encouragements, I would never know that I could publish a review paper as a PhD student. And then I made it! With his supervision and encouragements, I overpassed many difficulties and successfully finished the work of this dissertation. I would also like to thank Prof. Dr.-Ing. Hans Jürgen Maier and Prof. Dr.-Ing. Ludger Overmeyer for being the reviewer and the committee chair of my defense. Thank them for their time and valuable comments!

At IDS, I was specifically integrated in the group of "Piezo- and Ultrasonic Technology". Many many thanks to my group leader Dr.-Ing. Jens Twiefel, a very nice, smart, patient and experienced leader. We had very often meetings and "endless" talks, during which I learned a lot. For all the problems I've met, Dr.-Ing. Jens Twiefel can always take me to different aspects and different directions and thus enlighten me with new ideas. During the past years, we worked together on many papers and Deutsche Forschungsgemeinschaft (German Research Foundation) proposals, which are a great success to me. Under the supervision of Dr.-Ing. Jens Twiefel, our group members are quite collaborative. I first want to thank Michael Weinstein who is an expert on control. Every time when I had problems with control as well as other issues, he was always willing to help no matter how he busy was. His help is greatly appreciated! I also thank Igor Ille, another expert on control in our group, for his help and the PLL controller he made. Thanks to Gabriel Ertz and Andreas Schmelt for reading my dissertation and their valuable comments. My gratefulness is also given to Viktor Hofmann, Fushi Bai, Peter Bruns and Joscha Roth for exchanging ideas. I would also thank the other colleagues at IDS and my students who did their Bachelor theses, student research projects, Master theses and HiWis with me. Thanks for their help on both scientific and non-scientific issues.

This work was conducted under the collaboration with the Institute of Micro Production Technology (IMPT) and Laser Zentrum Hannover e.V. (LZH). Thanks to Dr.-Ing. Marc Christopher Wurz and Folke Dencker for their help on preparing specimens and the analyses with electron microscopy. Thanks to Dr.-Ing. Jörg Hermsdorf and Friedrich

Schneider for their help on the laser illumination.

Many thanks to the financial support from German Research Foundation and the Ministry of Science and Culture of Lower Saxony, Germany. Thanks to Hesse Mechatronics GmbH for providing the bonding head.

Last but not the least, I give my deep gratefulness to my family, my father Zhonghua Long, my mother Yufen Wang, my sisters Juanjuan Long, Nana Long and Yuanyuan Long, and my niece Shiyong Liu. Thanks to them for their long-term understandings, support and the happiness brought to me!

Yangyang Long

Hannover, April 2019

Contents

List of Symbols	VIII
Kurzfassung	X
Abstract	XI
1 Introduction	1
2 State-of-the-art	4
2.1 History of US wire bonding	4
2.1.1 Invention of the technology	4
2.1.2 Historical understanding of the joining mechanism	6
2.2 Bonding mechanisms	7
2.2.1 Pre-deformation and activation of US vibration	9
2.2.1.1 Pre-deformation	9
2.2.1.2 Activation of US vibration	10
2.2.2 Friction	10
2.2.2.1 Friction behavior	10
2.2.2.2 Tangential force modeling at the wire/substrate interface	12
2.2.2.3 Removal of contaminants	14
2.2.2.4 The sliding at the wire/tool interface	16
2.2.3 Ultrasonic softening	17
2.2.3.1 State-of-the-art in understanding ultrasonic softening	17
2.2.3.2 Macroscopic deformation in wire bonding	18
2.2.3.3 Microwelds	20
2.2.4 Interdiffusion	21
2.2.4.1 Interdiffusion	21
2.2.4.2 Recrystallization and Recovery	23
2.3 Other impact factors	24
2.3.1 Process parameters	24
2.3.2 Surface condition	25
2.4 Energy flow	26
3 Objectives	29
3.1 Analysis of the state-of-the-art	29

3.2	Objectives	30
3.3	Methods of solution	30
4	Investigations on relative motion	32
4.1	Experimental setup	32
4.1.1	US wire bonding platform	32
4.1.2	High-speed observation system	34
4.1.3	Laser illumination	35
4.2	Investigation of relative motions	37
4.2.1	Relative motion at the wire/substrate interface	38
4.2.2	Relative motion at the wire/tool interface	39
4.3	Quantification of the relative motions	41
4.4	Impacts of process parameters	43
4.5	Micro-slip at the wire/tool interface	48
4.5.1	Change of wire surface topography	49
4.5.2	EDAX analysis of wear	52
4.5.3	Accumulations of aluminum on the bonding tool	55
4.6	Conclusion	56
5	Experimental investigations on oxide removal	57
5.1	Experimental setup	57
5.1.1	Observation of the wire/substrate interface	57
5.1.2	Specimen preparation	58
5.2	Oxide removal for non-coated wire	59
5.2.1	Real-time observation	59
5.2.1.1	Central contact region	59
5.2.1.2	End contact region	63
5.2.2	Validation of real-time observation by microscope	66
5.2.2.1	Validation by laser confocal microscope	66
5.2.2.2	Validation by SEM	67
5.2.3	Impact of process parameters	69
5.2.4	Movement of oxide particles	72
5.3	Oxide removal with coated wire or glass	73
5.3.1	Oxide removal mechanisms	73
5.3.1.1	Cracks, detachment and milling	73
5.3.1.2	Metal penetration through the oxide layer	74
5.3.1.3	Oxide flow and metal splash	75
5.3.1.4	Pushing	76
5.3.1.5	Impact of the coated oxide on bonding strength	77
5.3.2	SEM observation of metal-glass bonding interfaces	78
5.3.3	Validation of oxide removal mechanisms	81
5.3.3.1	Validation by a thick Al_2O_3 layer	81
5.3.3.2	Validation by coating on both wire and glass	82

5.3.3.3	Validation by copper wire on glass	84
5.3.3.4	Validation by micro-particles	85
5.3.4	Summary of the oxide removal process	86
5.4	Oxide particles	87
5.4.1	Real-time observation of flying particles	87
5.4.2	SEM observation	88
5.5	Conclusion	89
6	Energy flow	91
6.1	Simplification	91
6.2	Quantification of energies	92
6.2.1	Energy of the transducer	92
6.2.2	Energy of the voice coil actuator	94
6.2.3	Friction energy	94
6.2.3.1	Cleaning coefficient	95
6.2.3.2	Friction energy due to vibration	96
6.2.3.3	Friction energy due to plastic deformation	97
6.2.4	Kinetic energy of wire vibration	98
6.2.5	Energy for APE	98
6.2.6	Energy for microwelds formation and breakage	99
6.2.7	Energy emitted into the environment	100
6.3	Global energy flow	101
6.4	Impact of process parameters	102
6.5	Conclusion	104
7	Discussion on results	105
8	Conclusion and outlook	107
8.1	Conclusion	107
8.2	Outlook	109
	Reference	110

List of Symbols

Latin notation

c_p	The mass heat capacity of the wire material
C_m	The mechanical capacitance of the transducer
C_p	The electrical capacitance of the transducer
d	The diameter of the wire
D_v	The distance accumulated by the vibration induced relative displacement in horizontal direction
$E_{add-p-friction}$	The additional friction energy caused by the additional large normal force
$E_{defor,wire}$	The energy for the wire deformation
$E_{envi-loss}$	The energy emitted to the environment
$E_{p-friction}$	The plastic deformation induced friction energy
E_{p-mw}	The plastic deformation induced energy for microwelds formation, deformation and breakage
$E_{tran-input}$	The electrical input energy of the transducer
$E_{tran-loss}$	The electrical loss energy of the transducer
$E_{tran-output}$	The electrical output energy to the transducer
$E_{tran-stor}$	The storage energy of the transducer
$E_{v-friction}$	The vibration induced friction energy
E_{v-mw}	The vibration induced energy for microwelds formation, deformation and breakage
$E_{v,wire}$	The kinetic energy of wire vibration
$E_{VCA-loss}$	The loss energy from the voice coil actuator
$E_{VCA-output}$	The output energy from the voice coil actuator
$E_{VCA-stor}$	The storage energy of the voice coil actuator
F_T	The tangential force
F_N	The normal force
$F_{add,N}$	The additional normal force required to deform the wire
$i(t)$	The instantaneous current at the process time t
l	The length of the wire within the recording window
L_m	The mechanical inductance of the transducer
L_{VCA}	The inductance of the voice coil actuator
m	The mass of the wire underneath the tool tip
P	The laser power input at the bonding site

R_{808}	The reflectance of the material for 808 nm light
R_m	The mechanical resistance of the transducer
R_{VCA}	The resistance of the voice coil actuator
S_N	The tool tip displacement in vertical direction
S_p	The plastic deformation induced relative displacement in horizontal direction
t	The bonding process time
$u(t)$	The instantaneous voltage at the process time t
$v(t)$	The instantaneous vibration speed of the wire at the process time t
W_{NF}	The work of the normal force

Greek notation

$\varphi(t)$	The area ratio of microwelds area over the whole contact area
μ_{met-ox}	The friction coefficient of metal-oxide contact
μ_{mw}	The equivalent friction coefficient for microwelds formation, deformation and breakage
ω	Angular frequency
ρ	The density of the wire material

Abbreviation

<i>APE</i>	Acoustoplastic Effect
<i>DDS</i>	Direct Digital Synthesizer
<i>EDAX</i>	Energy dispersive X-ray spectroscopy
<i>EFTEM</i>	Energy-Filtered Transmission Electron Microscopy
<i>IMCs</i>	Intermetallic compounds
<i>PSD</i>	Phase sensitive demodulation
<i>QBSD</i>	Quad-backscattered diffraction
<i>SE</i>	Second electron
<i>SEM</i>	Scanning electron microscope
<i>TEM</i>	Transmission Electron Microscope
<i>US</i>	Ultrasonic

Kurzfassung

Untersuchungen zu den Mechanismen des Ultraschall-Drahtbondens

Ultraschall-Drahtbonden ist eine vorherrschende Verbindungstechnik in der Mikroelektronik-Verpackungsindustrie. Die genauen Mechanismen, insbesondere die der Reibungs- und Entfestigungsphase, sind trotz ihrer breiten Anwendung seit mehr als ein halbes Jahrhundert nach ihrer Erfindung noch unklar. Mit dem Ziel, die große Lücke zu einem guten Verständnis der Mechanismen zu schließen, konzentriert sich diese Dissertation auf die relativen Bewegungen an den Draht/Substrat- und Draht/Werkzeug-Grenzflächen sowie auf den Oxidentfernungsprozess. Darüber hinaus wird ein Energieflussmodell von der elektrischen Eingangsenergie zu den verschiedenen an den Mechanismen beteiligten Energien entwickelt und quantifiziert.

Die Relativbewegungen an den beiden Grenzflächen wurden durch ein Echtzeitbeobachtungssystem untersucht, mit dem die Mikrometerbewegungen des Werkzeugs und des Drahtes erfasst wurden. Die Bewegungen wurden dann verfolgt und quantifiziert. Zusätzlich wurden die Einflüsse der Prozessparameter wie Normalkraft, Ultraschall-Leistung und Prozesszeit analysiert. Dabei wird der kombinierte Effekt von Normalkraft und Ultraschall-Leistung hervorgehoben. Durch eine weitere Untersuchung der Änderungen der Oberflächentopographie und der Elementverteilung wurde nachgewiesen, dass sich die relativen Verschiebungsamplituden an verschiedenen Stellen der Draht/Werkzeug-Grenzfläche unterscheiden. Mit der Substitution des Metallsubstrats durch ein transparentes Glas wurde der Verbindungsprozess sichtbar gemacht und verschiedene Bereiche einschließlich der Kontakt-, Reibungs-, Haft-, Mikroschweiß- und Oxidbereiche detektiert. Der Oxidentfernungsprozess wurde untersucht, wobei teilweise zusätzliche Beschichtungen entweder am Draht oder am Substrat aufgebracht wurden, um die Vorgänge besser sichtbar zu machen. Ein vollständiger Entfernungsprozeß einschließlich Risse, Ablösung, Mahlen und Transport wurde untersucht. Der Transport umfasst weiterhin Durchdringen, Oxidfluss, Schieben und Metallspritzen. Die Quantifizierung von Energiefluss zeigt, dass die größten Anteile der Ultraschall-Energie zur schwingungsinduzierten Reibung an den beiden Grenzflächen und zur schwingungsinduzierten Bildung, Verformung und Bruch von Mikroschweißungen fließen. Aus dem Energiefluss zur Draht/Substrat-Grenzfläche und zur Bildung von Mikroschweißungen wird die optimale Kombination aus der Normalkraft und der Ultraschallleistung bestimmt.

Schlagwörter: Ultraschall-Drahtbonden, Verbindungsmechanismen, relative Bewegung, Oxidentfernung, Energiefluss

Abstract

Ultrasonic (US) wire bonding is a predominating interconnection technique in the microelectronic packaging industry. Despite its long-term usage and wide applications, the mechanisms, especially those of the friction and softening phases, are still unclear more than half a century after its invention. Targeting on reducing the big gap to a good understanding of the mechanisms, this dissertation focuses on the relative motions at the wire/substrate and wire/tool interfaces, and the oxide removal process. In addition, an energy flow model from the electrical input energy to the different energies involved in the mechanisms is developed and quantified.

The relative motions at the two interfaces were investigated by a real-time observation system with which the micrometer-motions of the tool and the wire were captured. The motions were then tracked and quantified. In addition, the influences of the process parameters including the normal force, US power and process time were analyzed and the combined effect of the normal force and US power was emphasized. By a further investigation on the changes of the surface topography and elements distribution, it was proved that the relative displacement amplitudes at different locations of the wire/tool interface differ. With the substitution of the metal substrate by a transparent glass, the bonding process was visualized and different areas including the contact, friction, stick, microwelds and oxides areas were detected. The oxide removal process was studied with artificial coatings on either the wire or the substrate. A complete removal process including cracks, detachment, milling and transportation was studied. The transportation further includes penetration, oxide flow, pushing and metal splash. The quantification of energy flows shows that most US energy flows to the vibration induced friction at the two interfaces and the vibration induced formation, deformation and breakage of microwelds. Based on the energy flow to the wire/substrate interface and to the formation of microwelds, the optimal combination of the normal force and the ultrasonic power is determined.

Key words: ultrasonic wire bonding, bonding mechanisms, relative motion, oxide removal, energy flow

1 Introduction

Ultrasonic (US) wire bonding is a predominating interconnection technique in electronic packaging industry. Nowadays, more than a million bonds per second are achieved worldwide by this technique, which are widely applied in ICs, transistors, power devices and many special fields [1,2], as shown in **Fig. 1.1**. Due to the increasing number of electric products, the number of US bonds will keep increasing in the near future [3] despite the large amounts of applications of emerging packaging techniques, e.g. Through Silicon Vias, 2^{1/2}D interposers, etc. Wire bonding has gained itself a large market with a turnover of billions of dollars a year [4].

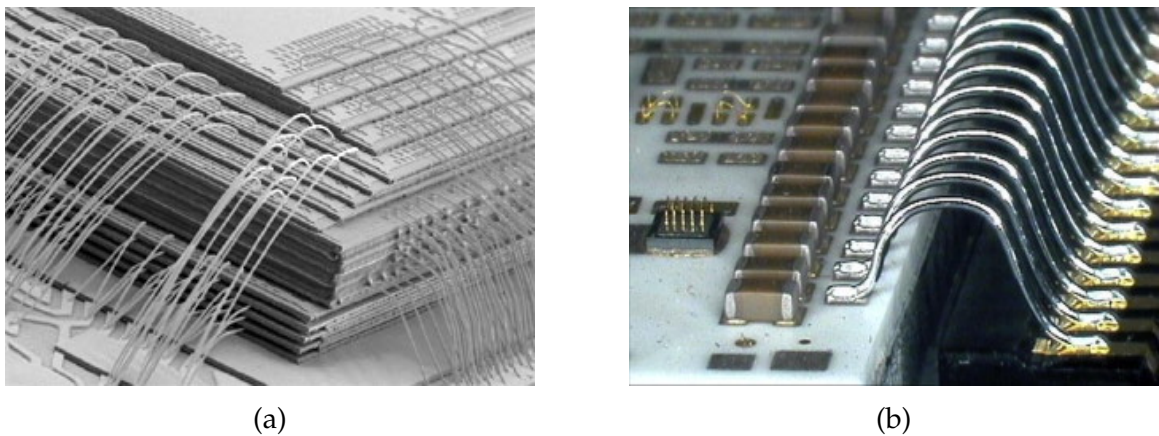


Fig. 1.1: (a) Ball-wedge bonding in ICs [5] (b) Wedge-wedge bonding in power devices [6]

In general, the US wire bonding technology can be subdivided into ball-wedge bonding and wedge-wedge bonding, depending on the bond shapes. Except that an additional electric flame-off step and an external heating source are required for ball-wedge bonding, the main processes of the two techniques are similar. A sketch of the wedge-wedge bonding process is shown in **Fig. 1.2**. In the figure, the blue part is the chip and the green plate is the lead frame. Specifically in step (b) and (d), reliable bonds between a metal wire and a metalization layer are produced by applying a normal force and US vibration within a short time.

The fundamental mechanisms behind the bond formation, however, are still not fully understood, despite that the wire bonding technology has been extensively used for decades. This prevents a further enhancement of the process with regard to both qua-

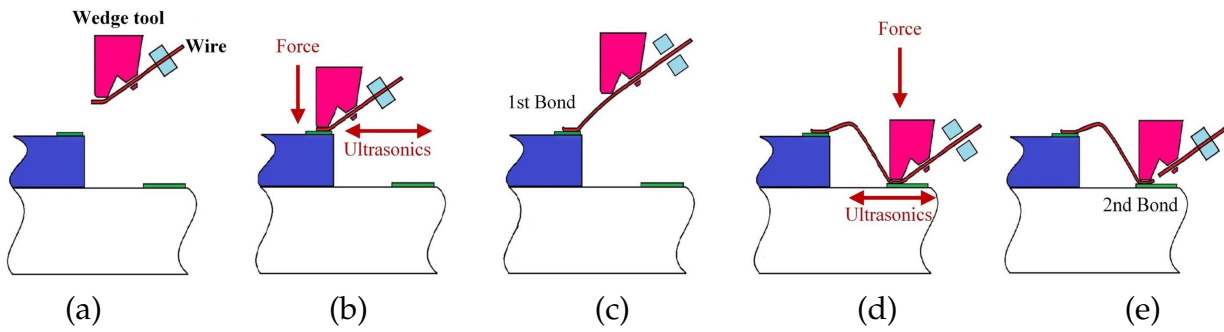


Fig. 1.2: Illustration of a typical US wire bonding process (a) searching for the 1st bond location on the die (b) activation of normal force and US vibration for the 1st bond formation (c) searching for the 2nd bond location on the lead frame (d) activation of normal force and US vibration for the 2nd bond formation (e) ripping-off wire for the next connection

lity and speed. The objective of this dissertation is to reduce the gaps to a better understanding of the mechanisms via detecting the phenomena occurring at the two interfaces within the bonding domain - the wire/tool interface and the wire/substrate interface. The following gaps are to be reduced in this dissertation:

- The relative motion behavior at the wire/tool interface: even though the vibration of the tool and the wire have been measured by laser vibrometer, the results cannot provide enough information. The laser beam measurements only allows the determination of the wire vibration at the positions of the measurement spots. Furthermore, the relative motion between the wire and the tool is assumed to be complex rather than a simple sliding between two rigid bodies. The relative motion at this interface is important as it influences the amount of energy that is transferred to the wire, the wear of tool and wire, and the potential damage to the bonding interface and the substrate.
- The contamination removal process: oxides, carbon, water vapor and other contaminants exist at the wire/substrate interface and inhibit direct metal-metal contact. They must be removed before microweld formation. In spite of its importance, very limited work has been performed on the removal process and very limited knowledge has been obtained, even from a qualitative view. A deeper understanding can accelerate the removal process, which leads to an earlier metal-metal contact, so that the bonding process can be enhanced.
- The energy flows during the bonding process: the ultrasonic wire bonding is a very complicated process including relative motion, vibration induced friction, plastic deformation induced friction, oxide removal, ultrasonic softening, microwelds formation and interdiffusion. Different amounts of energy are consumed for each phenomenon. A quantitative description of energy flows during the bonding process greatly helps a better understanding and further enhancements of the bonding process.

This dissertation is structured as follows: a detailed state-of-the-art survey is first presented in Chapter 2 to describe the mechanisms within a four-phases process model; specific open questions and objectives are then elaborated in Chapter 3; the relative motion at the wire/tool interface will be experimentally investigated and quantified in Chapter 4 with regard to both continuous plastic deformation and vibration; in Chapter 5, the contamination removal process will be analyzed via the real-time observation of the wire/substrate interface and coated oxide layer; based on the findings in the previous chapters, the energy flow model will be quantified in Chapter 6; finally, the contributions of the work will be discussed and summarized.

2 State-of-the-art

From an abstract and general point of view, the ultrasonic wire bonding process appears to be quite simple, as only a normal force and a sinusoid driving voltage need to be provided for a short time. However, when examined more in detail, it is extremely difficult to understand the process as very complicated dynamic changes take place within the very thin interfaces (the wire/tool interface and the wire/substrate interface) in a very short time. The phenomena occurring at the interfaces include expansion of the contact area, friction, contamination removal, microwelds formation and breakage, interdiffusion, recrystallization and recovery. In this chapter, the history of the US wire bonding is first introduced; the complicated changes of the phenomena are then classified and explained in four phases; finally, a detailed discussion on other issues which significantly influence the bonding process is provided. Some contents of this chapter have been published in [7].

2.1 History of US wire bonding

2.1.1 Invention of the technology

US wire bonding originated from ultrasonic welding of metal plates. The technique of ultrasonic welding, however, was discovered by accident. Back to the 1930s when resistance spot welding was utilized for metal welding, US vibration had not been applied in the field of welding. The traditional resistance spot welding has the shortcoming that the crystals are too big in the heat-affected zone as well as in the weld nugget, especially when the current is large [8]. To overcome this, Siemens [9] applied ultrasonic vibration to decrease the grain size. Later on, both researchers from Germany [10] and the USA [11] found out that the weld can be made by solely US vibration without the use of a welding current. Since then, ultrasonic welding became popular.

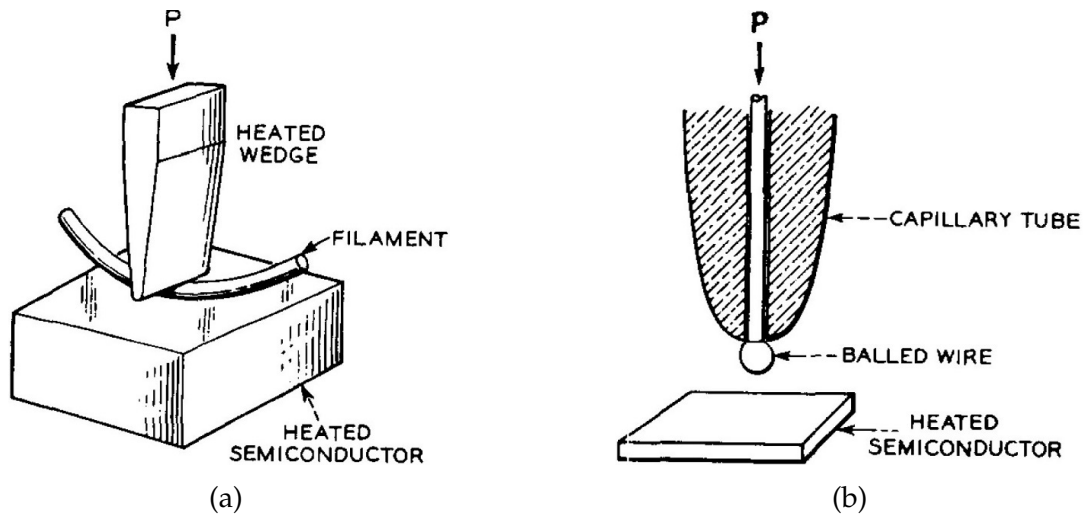


Fig. 2.1: (a) Thermo-compression wedge bonding (b) Thermo-compression ball bonding [12]

The first wire interconnection was made at Bell Telephone Laboratories in 1947 [2]. The concept of wire bonding, however, was not reported until 1957 by Anderson et al. [12]. Even though the process applied only pressure and heat without US vibration (thermo-compression bonding), the form of modern wedge tools and capillary tools for wire bonding were provided, as shown in Fig. 2.1. The concept of US welding was then further developed into wire bonding around 1960 [13]. In the new bonding process, which was then named either wedge-wedge bonding or US bonding, only a normal force and US vibration were utilized. Later, in 1966, the concepts of thermo-compression bonding and US bonding were combined by Coucoulas [14] to produce ball-wedge bonding, also known as thermosonic bonding. These two bonding systems appeared already similar to modern ones. In Fig. 2.2, a typical modern wedge-wedge bonding machine is shown. The bonding head has four degrees of freedom and mainly consists of a voice coil actuator and a US transducer. The bonding tool is coupled with the transducer. The working principle of the transducer will be described in Chapter 4. Additional information on modern bonding machines can be found in the book by Harman [15].

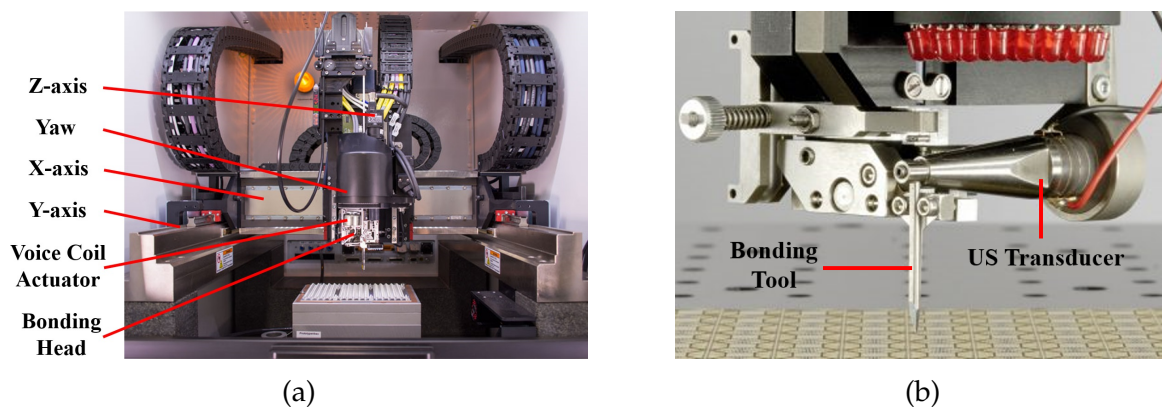


Fig. 2.2: (a) A modern bonding machine and (b) a bonding head [16]

2.1.2 Historical understanding of the joining mechanism

Shortly after the invention of US welding and US bonding (wedge-wedge bonding), researchers extensively studied the joining mechanism by checking the microstructure and the temperature at the interface. Since US wire bonding mainly applies US vibration, a sliding between the joining metal surfaces was supposed to take place. As a result, the first impression given by US welding or bonding was the occurrence of melting during the process. However, it was commonly accepted that the welding process is a solid-state bonding process where no melting occurs and the heat generated by friction only assists the adhesion [17,18]. Jones et al. [19] stated that the interface temperature is in the range of 35% ~ 50% of the melting point of the joined metals. Daniels [20] pointed out that the measurement of the temperature gives only an average value over the whole interface instead of the peak values at the asperity tips. In other words, the flash temperature (the peak temperature at a tiny spot during a short period) could be much higher.

At the beginning of the 1970s, US bonding was performed in liquid nitrogen to investigate the role of temperature on bond formation [21,22]. Unexpectedly, the bonding quality at $-195\text{ }^{\circ}\text{C}$ was equivalent to that at room temperature. Due to the ultra-low temperature of liquid nitrogen and the high heat conductivities of the joining metals and the wedge tool, the occurrence of a high temperature should not occur in their experiment. This suggests that the significance of temperature during the bonding process is not high. With the amplitude measurement of the bonding partners by a laser interferometer (see Fig. 2.3), Joshi [22] even argued that there was no vibration induced relative motion between the wire and the substrate. Fig. 2.3, however, does not provide any information on time and displacement. The joining of metals was then attributed to the US softening effect and local surface slips [23].

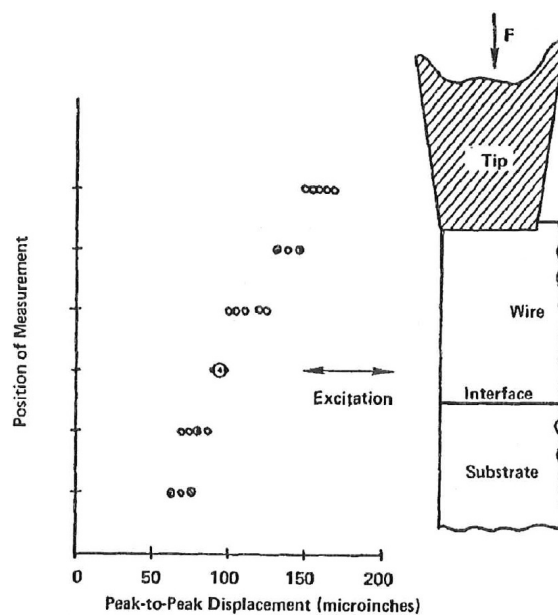


Fig. 2.3: Vibration amplitude measurements of US bonding partners [22]

By observing the silicon substrate surface, Winchell and Berg [24] found a periodic groove structure that has the same size as the tool tip amplitude. This suggested that a reciprocal sliding exists at the wire/substrate interface. Different from Joshi's conclusion [22], Osterwald [25] performed real-time measurements on the displacements of the bonding partners by laser vibrometers and a reciprocating sliding at the wire/substrate interface was detected. In 2009, Gaul et al. [26] captured the reciprocating sliding by a high-speed camera. Finally, the occurrence of a vibration induced relative motion between the wire and the substrate during the bonding process was confirmed.

In contrast to the discussion on the relative motion, which has found a final answer, the discussion on the temperature increment at the wire/substrate interface has not yet stopped. In general, the average temperature increment is less than 80 °C depending on the process parameters, as detected by Joshi [22]. The highest temperature that has been detected for US bonding is about 300 °C which was obtained in a series of bonding experiments operated from 40 kHz to 780 kHz [27]. Due to the resolution and reaction time of the sensors, the flash temperature has not yet been detected. Other arguments for the existence of a high temperature came from theoretical calculations on depletion of dislocations close to grain boundaries [28] and on atom diffusion distance [29]. Since the impact of ultrasound on dislocation movements and atom diffusion is still unclear, these topics need further study. Despite these uncertainties, the importance of temperature for a high quality bond was strengthened by many researchers [23,30,31]. A high temperature could contribute to the material softening, microwelds formation, interdiffusion and recrystallization & recovery. The specific contributions of the temperature to these factors, however, need more studies to be quantified.

2.2 Bonding mechanisms

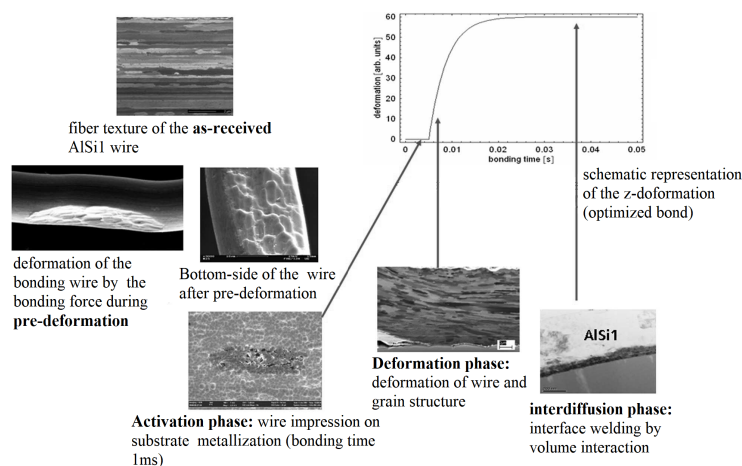


Fig. 2.4: Different phases during US wire bonding from [32]

Very complicated phenomena take place at the bonding interface and their dynamic changes are quite fast. To explain these phenomena, the bonding process was classified

into different phases. The commonly used classification was developed from Osterwald [25] and Mayer et al. [33]. A representative illustration of the phases is provided in Fig. 2.4. Even though there are small differences among the classifications from different researchers, they have a common feature: the phases (either four or five) are in a temporal sequence. Based on the theories and experimental results from the literature, this kind of classification lacks an important characteristic: the overlap among different phases. Therefore, a new classification of the bonding process is proposed in Fig. 2.5.

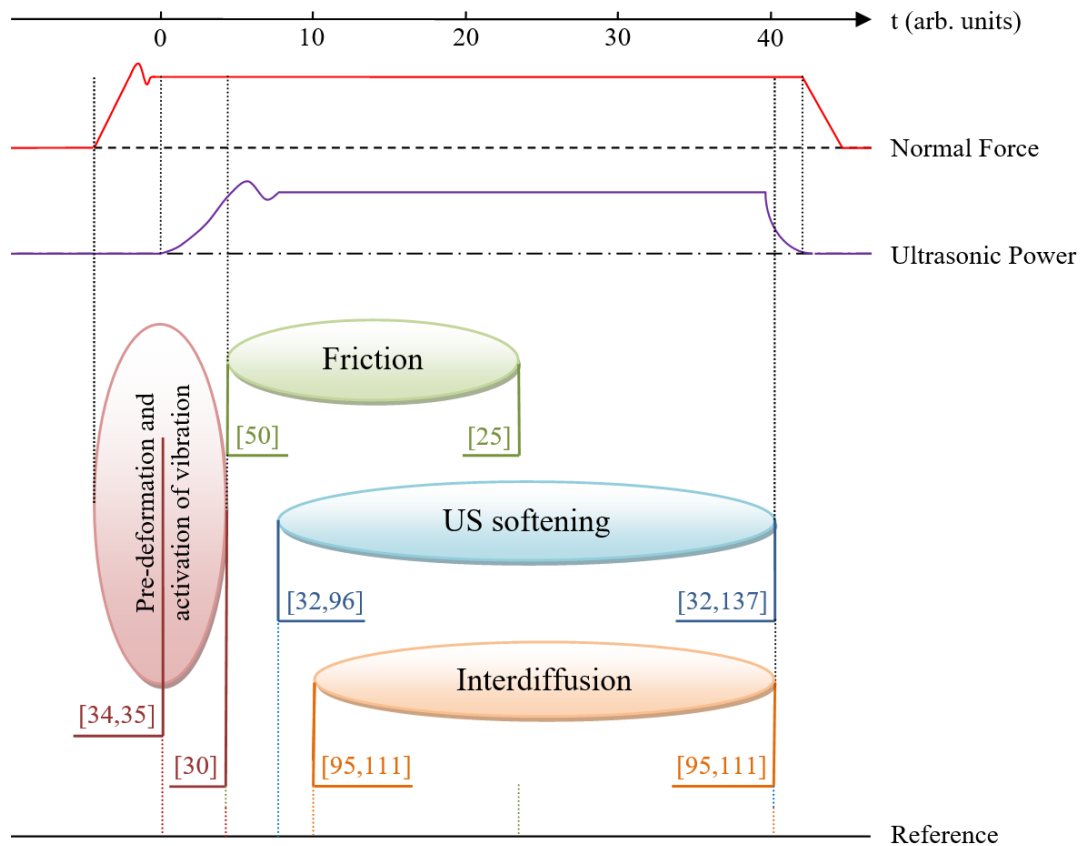


Fig. 2.5: Phase division of the bonding process with the overlap characteristic

1. The first phase contains two steps: the loading of a touch-down force and the activation of US vibration. The touch-down of the tool causes a plastic deformation of the wire and US vibration is activated afterwards. Since there is no relative motion between wire and substrate during the starting period of US vibration, the activation is classified as part of the first phase so that the friction phase can be better explained.
2. After the vibration amplitude of the tool exceeds a threshold value, the wire starts to slide on the substrate. During the sliding (friction), oxides are removed and pure metal surfaces are exposed.
3. Due to the US softening effect, the bulk material of the wire as well as the asperities are continuously deformed. This leads to the approaching of local surfaces where oxides have been removed. When the atoms from these local surfaces form metallic bonds, a microweld is achieved.

4. Once a microweld is formed, interdiffusion begins and lasts until the end of the process. In the meantime, recrystallization and recovery take place.

The last three phases overlap each other as they take place at the same time but at different locations of the interface. In the following subsections, these phases will be sequentially explained in detail.

2.2.1 Pre-deformation and activation of US vibration

2.2.1.1 Pre-deformation

At the first or the second bonding site, the bonding tool is loaded onto the wire with a normal force. This force is applied during the touch-down of the tool and is usually larger than the normal force applied during US vibration. It is referred to as the touch-down force. Due to the dynamic loading, the peak value of the touch-down force is normally 25% larger than the nominal touch-down force [34]. The loading time varies from ~ 0.05 ms to ~ 4 ms, according to the literature [34,35].

The touch-down force causes a plastic deformation and cold-working of the wire. The plastic deformation transforms the wire/substrate interface from line contact to elliptic area contact. The size of this elliptic area can be increased by a larger touch-down force. Another important effect of the plastic deformation is the generation of cracks in the oxide scale covering the pure metal surface, especially for brittle oxide like aluminum oxide (Al_2O_3). The cracks greatly facilitate the subsequent removal process of the oxides [36]. According to [37], only 1% or less asperities deformation is required to cause the breakage of aluminum oxide scale. This implies that the oxide scale can be easily broken up at the tips of asperities. The cracking of the oxide scale also takes place at the peripheral region of the contact where the deformation of the wire is large [21]. This is totally different for copper oxide, the hardness of which is only one tenth of that of aluminum oxide. It is hardly cracked [38]. Due to the high deformation rate during the force loading process, the wire is cold worked. The cold working of wire increases the hardness of the wire and generates large amounts of vacancies at the wire/substrate interface.

The pre-deformation of wire also remarkably influences the following process. Osterwald [25] argued that a greater touch-down force results in a longer oxide removal process since a larger wire/substrate contact area is generated. By evaluating the penetration of wire into the asperity valleys of the substrate, Althoff et al. [39] stated that a large pre-deformation is preferred when the substrate material is softer than the wire material. And a smaller touch-down force shall be set when the substrate materials are harder. A good penetration/coupling induces a large initial real-contact area so that the potential microwelds area is increased.

2.2.1.2 Activation of US vibration

After the normal force is loaded, the US vibration is activated. After turning on the US power supply, the driving current amplitude of the transducer needs several milliseconds to reach its peak value (in most cases, there is an overshoot of the nominal value). The vibration amplitude of the tool needs time to increase as well. In the beginning when the vibration amplitude is small, the wire is unable to slide the substrate which is constrained by the static friction force between the wire and substrate. The wire does not slip on the substrate until the tangential force reaches the maximum static friction force between the wire and substrate. It should be pointed out that the friction coefficient at the wire/tool interface is larger than that at the wire/substrate interface due to the material and surface topography. Therefore, sliding always starts at the wire/substrate interface. Due to the tangential force at the two interfaces, an elastic deformation of the wire takes place as shown in Fig. 2.6. The period from turning on the US power supply to the first stick/slip transition is termed the activation of US vibration.

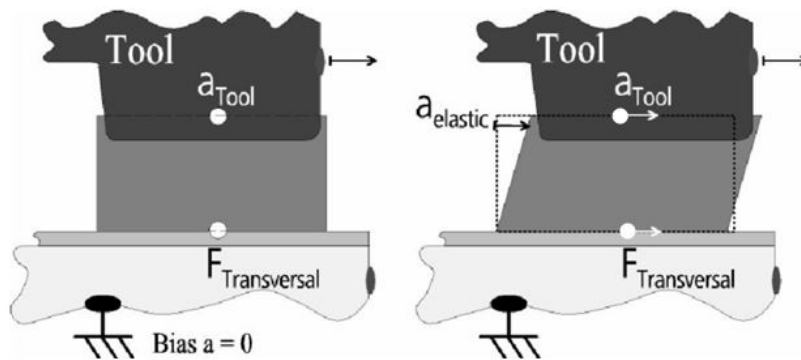


Fig. 2.6: Elastic deformation of wire [30]

In modern state-of-the-art wire bonding machines, the US vibration is always activated after the normal force loading. A reverse sequence has been studied by Xu et al. [40] during Au and Cu ball-wedge bonding processes. The US power was first turned on and set to a smaller value than the commonly applied power. The application of pre-US power helps to remove oxides at the central contact area and facilitates the formation of microwelds as well as the formation of Au-Al/Cu-Al intermetallic compounds (IMC). Finally, an improvement of the bonding strength was achieved. The advantage of adding a pre-US power was also validated by Descartin et al. [41].

2.2.2 Friction

2.2.2.1 Friction behavior

Due to the low stiffness of the wire compared to that of the tool and the substrate, the friction or sliding of wire on substrate is complicated. In general, the combination of two models are used to describe the friction behavior between the wire and the substrate: a)

the Mindlin model [42] and b) the stick-slip model [43]. These two models are discussed in the following.

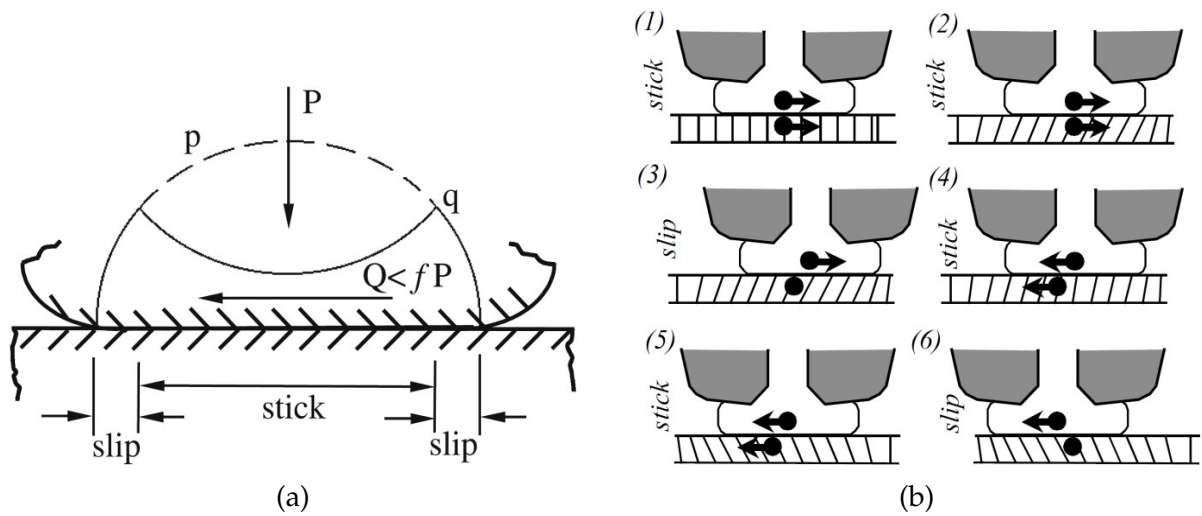


Fig. 2.7: A representative illustration of (a) Mindlin model [44] (b) Stick-slip model [45]

The **Mindlin model** was originally used to calculate the interface slip when an oscillatory force was applied to two compressed elastic bodies [42]. It is usually used to explain the micro-slip behavior of the wire when the US power is less than a threshold value of a corresponding normal force. An adapted model for ball bonding is illustrated in **Fig. 2.7** (a), in which a ball is pressed on a flat surface and a tangential force is applied. At the central contact area, the ball sticks to the substrate as the tangential stress q is smaller than the maximum sticking stress fP , where f is the maximum static friction coefficient and P is the normal stress. Within the stick area, the tangential stress becomes larger and the normal stress becomes smaller with the increasing radial distance to the center point. In the slip area, the tangential stress becomes equal to fP and the peripheral area of the ball is able to slip on the substrate. According to Winchell and Berg [24], there is a band area between the stick area and the peripheral slip area, where the bond is formed. Since there is no sliding in the central contact area, the oxide within this area cannot be removed and thus a bond is not formed. In the peripheral slip area, no bond can be formed as the tangential stress would destroy the bond. However, in this model [24] the tangential stress over the whole interface was considered to be a constant value.

The **stick-slip model** was originally used to describe the friction between two metals [43]. It was shown that the stick-slip behavior always existed, regardless of whether lubricants were placed into the interface. This sliding behavior for wire bonding is illustrated in **Fig. 2.7** (b) and takes place when the US power is large enough to cause gross-slip. Since the substrate is not an ideal rigid body, a small elastic deformation will be caused by the sticking force between the wire and the substrate. Both contact points move at the same tangential velocity and there is no relative motion (1-2). When the sticking force reaches the threshold value, the wire starts to slip on the substrate (3). At the end of the first phase, when the tangential displacement of the wire has reached its maximum value, the motion is reversed and the same situation occurs again (4-6). Such a motion continues

from cycle to cycle. The bonding process performed under such a situation can produce a high quality bond, as most oxides are removed and more friction energy is generated for microwelds formation.

The stick-slip model must be combined with the Mindlin model to explain the sliding behavior of the wire, since micro-slip already occurs during the stick stage of the stick-slip motion. The relative displacement in the peripheral contact area is usually larger than that in the central contact area.

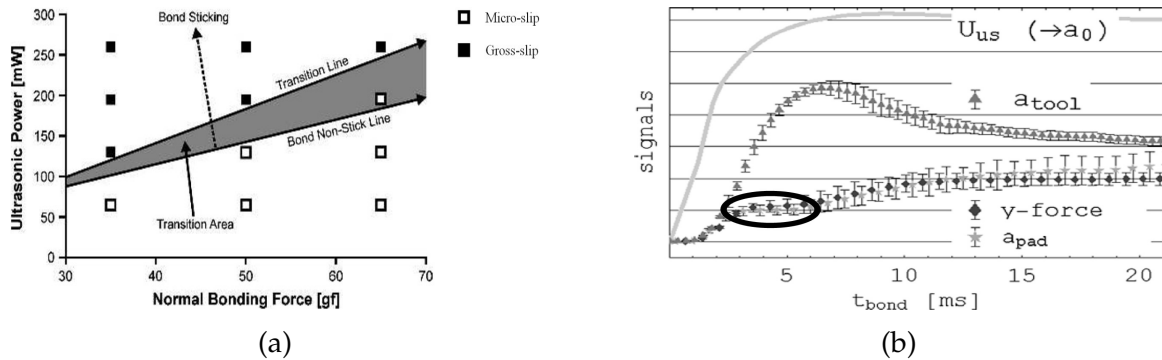


Fig. 2.8: (a) Impact of process parameters on the friction behavior of the wire (after [46])
(b) Friction plateau on the pad vibration course during the bonding process [47]

Whether the wire goes into gross-slip motion is dependent on the process parameters. In general, large US powers and small normal forces result in gross-slip. An illustration of the impact of the process parameters on the sliding behavior of the wire during thin wire bonding process was provided in Fig. 2.8 (a) [46]. During the measurement of the pad amplitude, a plateau was found [47], as marked in Fig. 2.8 (b). According to the authors, this plateau indicated the start of dynamic friction (relative motion) and that the cleaning energy accumulated during the plateau period was required to remove the contaminants [47].

2.2.2.2 Tangential force modeling at the wire/substrate interface

As mentioned at the beginning of Section 2.2, the friction phase and the softening phase overlap. This leads to a high level of difficulty in modeling the tangential force since both friction and microwelds connection coexist. In general, there are three different regions within the contact area: metal-oxide contact area, metal-metal contact area and microwelds area. It is hard to distinguish the metal-metal contact area from the microwelds area by observing the interface, because the breakage of microwelds also results in metal-metal contact. On this background, two analytical models were developed to estimate the tangential force.

The first model was established by Mayer and Schwizer [48,49] who considered the metal-metal contact as microwelds connection. The relative displacement amplitude between the wire and the substrate and the instantaneous tangential force are expressed as the following equations:

$$A_{rel}(F_T) = A(F_T) - A_{pad}(F_T) = A(0) - cF_T \quad (2.1)$$

$$F_{T,friction}(t) = [1 - \gamma(t)]\mu F_N + \gamma(t)\sigma S \quad (2.2)$$

where A_{rel} is the amplitude of the relative motion between wire and substrate; A is the vibration amplitude of the wire; A_{pad} is the vibration amplitude of the substrate/pad; $A(0)$ is the vibration amplitude of the bonding tool in free air; c is the compliance of the bonding system; $\gamma(t)$ is the ratio of the microwelds area over the whole contact area; σ is the average yield stress of all microwelds and S is the total contact area. In this model, the average shear stress of microwelds throughout the bonding process was assumed to be the yield stress of microwelds.

Based on the work of Mayer and Schwizer, Gaul et al. [47, 50] proposed a similar model for wedge-wedge bonding, but in their model the microwelds connection was considered as metal-metal contact. The instantaneous tangential force is expressed as:

$$F_T(t) = [(1 - \varphi(t))\mu_{ox} + \varphi(t)\mu_{met}]F_{NB} \quad (2.3)$$

where $\varphi(t)$ is the ratio of the metal-metal contact area over the whole contact area; F_{NB} is the normal force; μ_{ox} and μ_{met} are the friction coefficient of the metal-oxide contact and the metal-metal contact, respectively. The results of this analytical model in the beginning stage of the bonding process are consistent with the results measured by shear force tests. The assumption behind this model is that the microwelds connection was considered to be friction with a large friction coefficient.

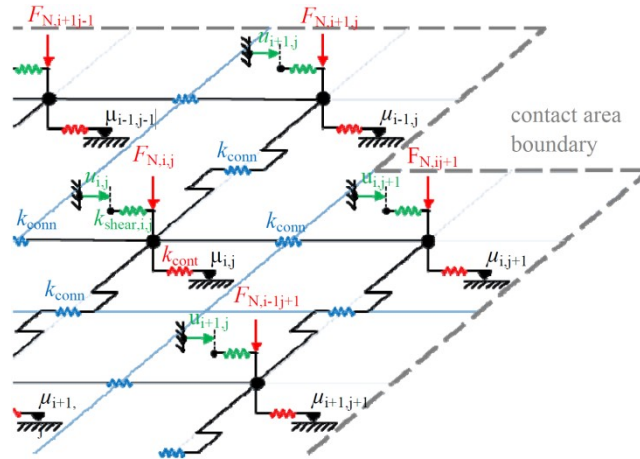


Fig. 2.9: Friction model with point-contact element [39]

A numerical model was developed by Althoff et al. [39, 51] and is shown in **Fig. 2.10**. In this model, the microwelds formation was assumed to be caused by high friction energy. In other words, the model was used to calculate the friction energy at the wire/substrate interface. The contact area was obtained by Finite Element Method (FEM). The calculation of the friction force for each point element was based on the corresponding shear stiffness

k_{shear} , connection stiffness k_{conn} and the friction coefficient μ at time t . This model was validated by the real-time measurements of a micro piezo-sensor.

Many other researchers [52–58] tried to use FEM alone to calculate the stress distribution or temperature increment. Due to the high nonlinearities, the large number of impact factors and many unknown mechanisms, these models had to be simplified to achieve convergence. The results, however, can still provide certain information as the dynamic changes at micro/nano-scale are not always experimentally measurable.

Due to the direct connection and the consistence with the experiments, the model of Mayer and Schwizer as well as that of Gaul et al. are used as a basis in this work. Instead of the two assumptions behind the microwelds, an equivalent friction coefficient corresponding to microwelds formation, deformation and breakage will be estimated and applied. Details will be provided in Chapter 6.

Another mechanism that should be pointed out here is the vibration induced friction reduction, which is commonly considered when vibration and sliding are encountered. As indicated by the work of Storck et al. [59], the friction is reduced at a macroscopic time-scale, while the friction on a real-time basis still obeys Coulomb’s Law. Since the models used in this dissertation are formulated on a real-time basis, the friction reduction by US vibration is not taken into consideration.

2.2.2.3 Removal of contaminants

The most commonly used wire materials for wedge-wedge bonding are aluminum alloys (like AlSi1 and AlMg0.5 for thin wire bonding), and pure Al and Cu (for thick wire bonding). The surface of pure aluminum is normally covered by a layer of Al_2O_3 with an average thickness of 5 nm. This layer is brittle and dense enough to prevent further oxygen invasion. The oxide surface normally attracts two hundred layers of dipole molecules, like water vapor [60]. As opposed to Al_2O_3 , the copper oxide Cu_2O is soft and has a loose structure. Oxygen can penetrate into the oxide layer and oxidize the inner metal. As a result, the copper oxide layer increases continuously. With the reaction to water vapor, $Cu(OH)_2$ can even be detected on top of the oxide layer [61]. The same situation exists when the substrate is made of copper. The deposition of a metal barrier layer, a thin organic film or a thin inorganic film can be applied to reduce the substantial oxidation of the copper pad [62–64]. Before microwelds are formed, these contaminants (mainly oxides)

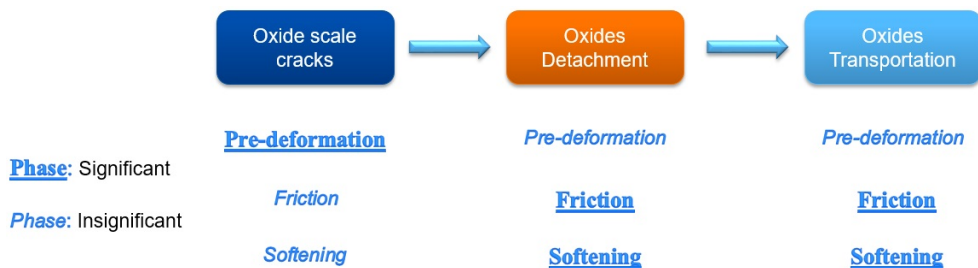


Fig. 2.10: The procedure of oxide removal with the effect of corresponding phases

must be removed to expose pure metal-metal contact. According to the literature, the oxide removal process consists of three steps and is shown in **Fig. 2.10**. The font style of the phases represents their significance on the corresponding step of the removal process.

As mentioned in Section 2.2.1.1, the pre-deformation causes cracks in the aluminum oxide layer. The detachment and transportation of the oxides are a result of vibration and continuous plastic deformation. The specific roles of vibration induced reciprocal relative motion and continuous plastic deformation induced relative motion on the oxide detachment and transportation, however, are still unclear. Gaul et al. [30] argued that the vibration induced reciprocal relative motion causes the detachment of oxides and that the deformation induced relative motion is responsible for transporting the oxides to the peripheral region. This claim, however, requires further theoretical analysis and experimental validation. Currently, the detachment and transportation of oxides are believed to be caused by the combined effect of vibration and plastic deformation.

Based on the classic wear law, the wear depth of aluminum oxide during a 120 ms bonding process was calculated to be only 0.6 nm [36]. This implies the importance of cracks for the detachment of the oxide layer. It is preferred that the detachment takes place at tall asperities where cracks of the oxide layer have occurred during the pre-deformation stage [65]. Maeda et al. [66] observed the distribution of oxides at the wire/substrate interface after the bonding process and found that most oxide particles piled up at the peripheral contact area. Furthermore, some particles rolled like a snowball during the transportation process and eventually became much larger. Not all the oxides are transported to the peripheral region. By checking the cross-section of a bond with Transmission Electron Microscope (TEM) [28,67], some oxides were found to remain within the central contact area and they prevented bond formation. The same situation also happens during ball-wedge bonding [68,69]. The transportation path of oxides remains unknown.

Compared to ball-wedge bonding, the wedge-wedge bonding process is less sensitive to contaminants [2]. Krzanowski and Murdeshwar [28] tried to bond a 75 μm aluminum wire on different metal substrates covered by a 40 nm carbon layer. Except the bonds on a smooth stainless steel surface, the pull strengths of the bonds did not decrease. This indicates that a soft and smooth surface helps to squeeze oxides into the peripheral region since the asperities are easier to deform. A hard and rough surface stores the contaminants at the bottom of valleys while pure metal at the asperity tips can be exposed. The oxide-free area on a smooth hard surface seems to be the smallest since contaminants could cover both valleys and tips. Another study was conducted with a layer of titanium on the substrate surface [70]. It was shown that the bonding strength significantly decreased when the titanium layer exceeded 10 nm as excessive oxides within the contact area detrimentally affected the bond formation. An interesting result was that a 2 nm titanium layer enhanced the bonding quality. This might be due to the formation of a mixed oxide layer which can be easily removed.

2.2.2.4 The sliding at the wire/tool interface

Compared to the wire/substrate interface, the sliding at the wire/tool interface has been studied less extensively. Even the question of whether there is a relative motion at this interface has not yet been answered by previous works. However, the sliding at this interface also significantly influences the bonding quality. A severe relative motion at this interface could damage the microwelds at the wire/substrate interface or even cause cratering at the substrate, especially in the later stage of the bonding process. As a result, a better control on the relative motion at the wire/tool interface could be essential to the enhancement of the bonding process.

The first detection of a relative motion at the wire/tool interface was in ball-wedge bonding. Based on the 3rd and 5th harmonic signals of a micro-sensor, Mayer et al. [33] and Schwizer et al. [71] confirmed the existence of a slip between the ball and the capillary. Gaul et al. [72] observed the wire/tool interface during a thin wire bonding process with a high speed camera, but they did not find a relative motion, except in the case of over-bonding. The illumination of the experiment, however, was from the back side of the bonding site, which led to an unclear interface. Takahashi et al. [54] stated that a friction slip at the wire/tool interface must take place in the latter stage of a bonding process. This is due to the formation of microwelds that constrain the motion of the wire. Evidence of this was only found for thick wire bonding.

Indirect evidence came from the observation of the bonding tool after tens of thousands of bonds. A buildup of wear debris is usually found on the tool for aluminum wire bonding [57] while a severe wear on the tool can be observed for copper wire bonding [74,75]. In addition, flying flakes due to the relative motion were observed during copper wire bonding [75]. Another piece of evidence came from the velocity measurements of the wire and the tool by laser vibrometers [73]. A clear difference between the two velocities throughout the whole bonding process was detected. A dynamic model (see Fig. 2.11) was established based on these measurements to describe the stick-slip behavior at the two interfaces. In this model, an equivalent mechanical model was used to describe the

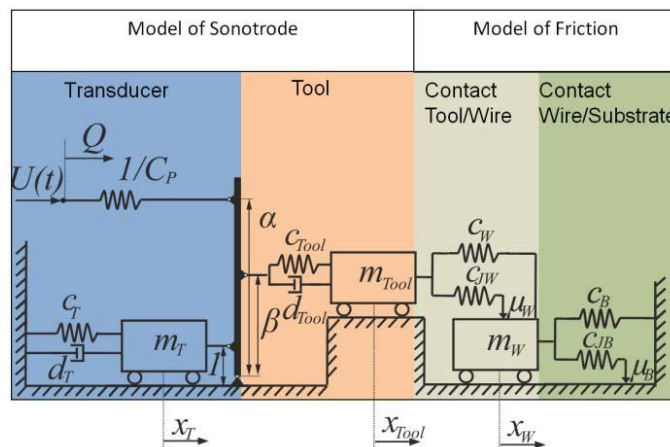


Fig. 2.11: A dynamic model for thick wire bonding process [73]

dynamics of the transducer which is coupled with the tool. In the figure, c stands for stiffness, d for damping, m for mass, α and β for the transducer force factors and μ stands for the friction coefficient.

Since the wear during copper wire bonding significantly decreases the tool lifetime, different methods have been proposed to improve the tool lifetime. First of all, the lifetime of the tool can be greatly enhanced by using wear optimized process parameters. This has been stated as the most efficient way [74,76,77]. Secondly, the life time can be improved by changing the shape of the tool. Xu et al. [78] designed a tool with three ridges within the groove. These ridges effectively decrease the relative motion between tool and wire. A tool with a big open angle was proposed by both Xu et al. [79] and Eichwald et al. [80]. Even though such designs are not favored by customers due to their appearances, wear can be greatly reduced.

2.2.3 Ultrasonic softening

2.2.3.1 State-of-the-art in understanding ultrasonic softening

The softening effect brought by US vibration was discovered almost at the same time as wire bonding. It first appeared in a short note in 1955 from Blaha and Langenecker [81]. They detected a large flow stress reduction when an 800 kHz vibration was imposed during the tensile test of a single Zinc crystal. Thus the flow stress reduction caused by US vibration was first called Blaha effect. Later the name Acoustoplastic Effect (APE) became more popular.

After the discovery of APE, many researchers tried to explain the underlying mechanism. The two main hypotheses are stress superposition and acoustic softening. The stress superposition hypothesis proposed by Nevill and Brotzen [82] suggested that the APE was solely caused by a superposition of an alternating stress on a static stress. In addition to this stress superposition, Blaha and Langenecker [83] further stated the significant effect of acoustic waves. It was proposed that the acoustic energy could be effectively absorbed by the defects within crystals so that the defects can easily move away from their pinned positions. In the following four decades, arguments on the two hypotheses have not stopped.

Two main points support for the hypothesis of stress superposition: 1) the force reduction is linearly proportional to the vibration amplitude and is independent of the vibration frequency; 2) the dimensional difference between the wave length and the defects is so large that the resonance activation of defects cannot be caused [82]. Even though the supporters for the acoustic softening hypothesis could not explain these points, many phenomena detected later indicate that the mechanism behind APE is more complex than a simple stress superposition. In 1962, it was found that excessive US energy causes a hardening effect [84]. The efficiency of acoustic waves to decrease a material's yield stress was then stated as being 10^7 times higher than that of heating, since only defects are assumed

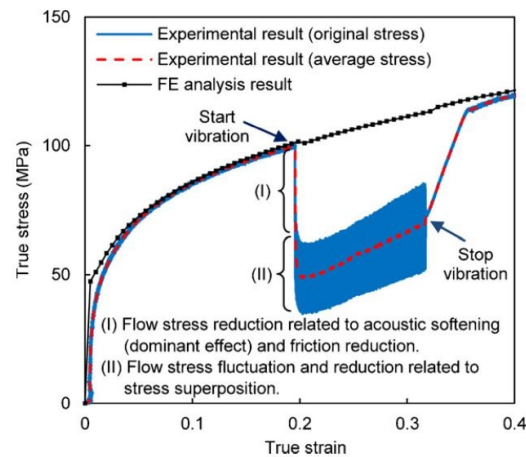


Fig. 2.12: The stress superposition and acoustic softening component of APE [90]

to absorb the acoustic energy instead of the whole crystal [85]. When vibration was superimposed in a direction that has no component on the basal slip system of a zinc crystal, APE was still detected [86]. Based on their experimental results, Sapozhnikov and Kustov [87] stated that the flow stress reduction consists of a fast time independent component due to dislocations activation and a slow time dependent component due to dynamic recovery. All of these findings support the acoustic softening hypothesis. As a consequence, the hypothesis of acoustic softening was commonly accepted. After entering the 21st century, the application of piezo-sensors allowed for the separation of stress superposition from the whole APE [88, 89]. A representative illustration is shown in **Fig. 2.12** from [90]. The oscillatory stress induced flow stress reduction is clearly observed in the signal of the sensor. The majority of the stress reduction caused by acoustic softening is also clear to see.

2.2.3.2 Macroscopic deformation in wire bonding

In the US wire bonding process, a transversal oscillating stress is superimposed on a normal static stress and the APE takes place. With the effect of both transversal stress superposition and acoustic softening, the yield stress of the wire is greatly decreased and continuous plastic deformation of the wire occurs. The plastic deformation is usually measured in the vertical (z) direction and such a measurement during thin wire bonding is shown in **Fig. 2.13** (a). The wire deformation depends on the normal force and the US power. The impact of these parameters for a thick copper wire bonding process is shown in **Fig. 2.13** (b). In general, a larger force and higher US power result in a larger z -deformation. Due to the complex mechanism and the nonlinearity of APE, the deformation of the wire is hard to calculate theoretically. Instead, it was predicted by neural network methods [91, 92]. The macroscopic deformation of wire leads to a larger wire/substrate contact area.

The continuous plastic deformation induces material flow (or relative motion) at the wire/substrate interface which is supposed to play an essential role in the detachment and the transportation of oxides. The specific effect of material flow on the oxide removal paths depends on the process parameters. After the chemical etching of wires, which

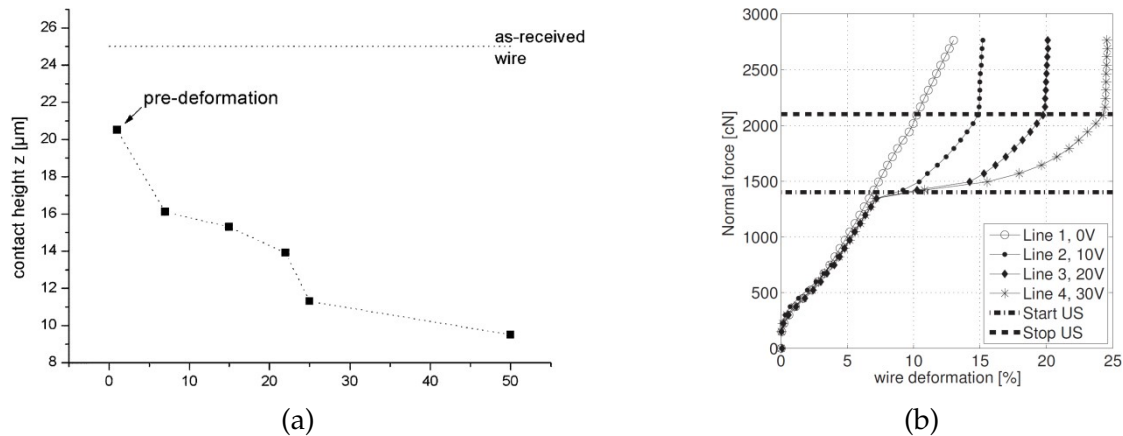


Fig. 2.13: z-deformation for (a) thin wire bonding [32] (b) thick wire bonding [92]

were bonded under different parameters, Ji et al. [93] observed different patterns of joint marks. These marks indicated different oxide (contamination) removal paths caused by different reciprocating relative motions and material flows. In addition, the surface hardness and smoothness of the bonding partners significantly influence the cleaning effect of the material flow. The authors claimed that a soft and smooth surface magnified this effect [28].

It is essential to further investigate the specific role of the material flow and reciprocating relative motion in the cleaning process. A current bottle neck point that needs to be addressed to enhance the bonding speed while keeping the high bonding quality is the enhancement of the self-cleaning efficiency of the bonding process. Efficiency means both the cleaning speed and effective removal of contaminations. If the contamination removal process were better understood, the bottle neck point might be overcome by either adjusting the process parameters or changing the topographies of the contact surfaces.

Another issue that should be noted is the hardness of the wire after the bonding process. The acoustic softening effect is a temporary effect that is only active when US power is on. Once the US power is turned off, the softening effect disappears immediately. According to [84], the exposure of a material to a very high level of US power leads to a hardening which permanently remains after the termination of US vibration. This can be explained by the density of defects. When US energy is imposed to the material, defects (especially dislocations) are activated from their pinned positions and move to the grain boundaries. Simultaneously, new defects are generated within crystals. When the US energy exceeds a certain level, the newly generated defects are more than those which have moved to the grain boundaries. This is not obvious when the US power is on since the newly generated defects are also activated by the acoustic waves and do not increase the yield stress. However, after switching off the US power, the crystals contain a higher density of defects. Thus the yield stress of the material increases and a hardening results. In the case of wire bonding, however, the situation becomes even more complicated as recrystallization and recovery are involved. The recrystallization and recovery greatly influence the final defect density. The final hardness of the wire depends on the defect density and on the

size of crystals. Both properties are a result of the competition between defect generation and depletion, and recrystallization and recovery. The recrystallization and recovery will be discussed in Section 2.2.4.

2.2.3.3 Microwelds

From a macroscopic point of view, APE leads to continuous plastic deformation while from a microscopic point of view, APE results in more contact surfaces since the material becomes softer. Krzanowski and Murdeshwar noted that the asperities get softened and flattened during the bonding process [28]. Murali et al. stated that the deformation of the asperities is the most significant factor on the bonding quality [94].

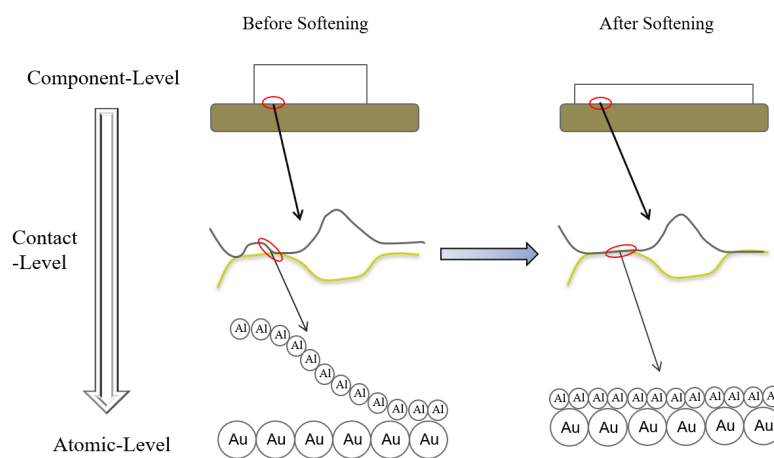


Fig. 2.14: The APE induced changes on macro- and atomic-level

Under the combined effect of acoustic softening, normal force and relative motion, the local surfaces of wire and substrate get closer and closer. The Van der Waals force determines the interaction between the two surfaces when they are sufficiently close. When the atoms of the two surfaces finally "contact" each other, metallic bonds form (see Fig. 2.14). This change has been experimentally proved by a TEM observation [95]. A local mated area enclosed by metallic bonds is called a microweld. Based on the detection of a sudden drop of the contact resistance, the first microweld was found to form 2-5 ms after the activation of ultrasound depending on process parameters [96]. After the oxide removal and pure metal contact at more locations, more microwelds form. The final amount and the sizes of microwelds determine the shear strength of the bond.

The real-microwelds are usually not the residues which can be directly observed by microscope after shear tests, as shown in Fig. 2.15 (a). Such wire residues usually consist of many microwelds, as shown in Fig. 2.15 (b). A common method for measuring the real microwelds area is via contact resistance measurements [96,97]. It was stated that the contact resistance method is more accurate than microscope observations [96]. It is further stated that the microwelds area grows linearly over the process time, which is supported by the measurements of the contact resistance [96].

In the work of Maeda et al. [99], the breakage (separation) of microwelds was first pro-

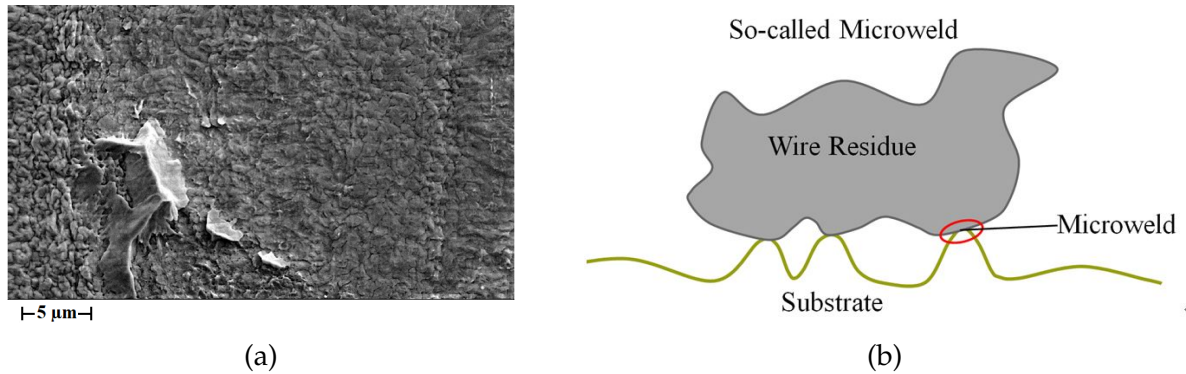


Fig. 2.15: (a) The wire residues (so-called microwelds) exposed after shear test (after [98])
 (b) Sketch of microwelds underneath a wire residue

posed. The bonding strength was stated to be determined by the competition between the formation and breakage rate of microwelds. Other than that, nearly no other article mentioned the concept of breakage. The lack of research on microwelds breakage might be due to the difficulty of measurement and the highly dynamic changes of microwelds during the bonding process. As described before, the commonly used methods for microweld measurement are via off-line microscope observation and on-line contact resistance measurement. The observation of microwelds can only be conducted after shear tests by which all microwelds are damaged. Furthermore, it is impossible to distinguish whether a microweld was destroyed by shear tests or had been destroyed before shear tests. Contact resistance measurements give the integrated information on the total area of microwelds. As long as the breakage rate is lower than the formation rate, the contact resistance measurement cannot determine the existence of breakage. The formation and breakage, which occur simultaneously, greatly increase the difficulty of analyzing microwelds breakage. It is assumed that in the beginning, local microwelds are broken by the relative motion. As time goes by, the topographies of the contact surfaces change and more microwelds are formed. When the total strength of the microwelds can afford to the tangential stress induced by the relative motion at a local area, less microwelds are destroyed and some microwelds remain. This assumption, however, needs further investigations.

2.2.4 Interdiffusion

2.2.4.1 Interdiffusion

One of the most intense discussions in the history of wire bonding was on the existence of interdiffusion. Thermal energy was usually considered as the main activation energy for interdiffusion. However, thermal activation is not sufficient for the diffusion distance during wire bonding. Based on thermal diffusion theory, the diffusion distance in 60 ms at 200 °C was calculated to be only 1 Å [100] which is far from the real range (tens to hundreds of nanometers [31,95,101]). A couple of old publications [18,29] stated that no

interdiffusion was detected, which might be due to the preparation of the specimen and the limited capability of old microscope machines.

Nowadays, interdiffusion during the bonding process is an indisputable fact. The discovery that self-diffusion or interdiffusion is enhanced by ultrasound was made even earlier in other fields. By inserting a rod into a cylinder hole connected to a US transducer, Kulemin and Miskevich [102] detected the enhanced interdiffusion between dissimilar materials in 1971. The interdiffusion speed was found to be even higher when a higher vibration frequency was applied. The main works on US assisted diffusion were summarized by Abramov [103]. The author underlined the importance of a high density of dislocations and further stated that the enhancement of diffusion takes place when the strain amplitude surpasses a threshold value.

Once a microweld is formed, interdiffusion starts immediately. The accelerated diffusion in wire bonding is attributed to the following mechanisms:

- **The stress and strain at the interface.** The high frequency vibration of the wire bonding process causes a very high acceleration. For a 58 kHz bonding process with a vibration amplitude of 6 μm , the acceleration is $\sim 80,000$ times higher than that of gravity. The large stress and strain can greatly enhance the diffusion rate at the interface [104,105].
- **The large number of vacancies.** The interactions among the moving dislocations generate a large number of vacancies [102,103]. Furthermore, the deformation at the interface creates a large number of vacancies as well. According to [95], the diffusion activation energy at these vacancies is 0.36 eV which is much smaller than the value of 0.69 eV by sequentially arranged atoms. As a result, the generation of the large amounts of vacancies accelerates the diffusion at room temperature.
- **The large amount of grain boundaries.** During the bonding process, recrystallization takes place at the region close to the interface. It results in a polycrystalline interface where the grain size is much smaller than that before bonding. This big change at the interface generates a large amount of grain boundaries where diffusion easily occurs [29].
- **The existence of transitory dislocations.** Due to the US energy, a large number of dislocations which only have a transitory existence are generated, which was proposed by Rhines et al. (cited in [106]). These dislocations provide energy for metal transportation so that the diffusion rate is enhanced.

The interdiffusion leads to a mixture of atoms which can react with each other and form Intermetallic compounds (IMCs) when dissimilar materials are bonded. The interdiffusion can be observed by the thickness of such an IMC layer. The most common IMCs in wire bonding are Au-Al IMCs and the interdiffusion rates between the two metals are highly ranked among all bonding materials. A 60 gf (0.588 N) normal force and a 150 mW US power within 20 ms could cause a large diffusion distance, which is as high as 200 nm

[31]. Compared to Au-Al IMCs, the formation of Cu-Al IMCs is much slower [107] and the formation of Au-Cu is even negligible [108]. The slow formation of IMCs indicates a lower speed of interdiffusion due to the misfit of atoms. According to [95], the formation of IMCs starts at different local spots and then extends to the whole interface. This seems reasonable since the formation of IMCs should start at the early formed microwelds and extend to other locations. A periodic diffusion path was observed by Ji et al. [109] while no other articles reported similar results. It was claimed that the growth of IMCs is determined by the Eshelby tensor at the interface [101,110] and the growth can be predicted by a thermomechanical model [111].

2.2.4.2 Recrystallization and Recovery

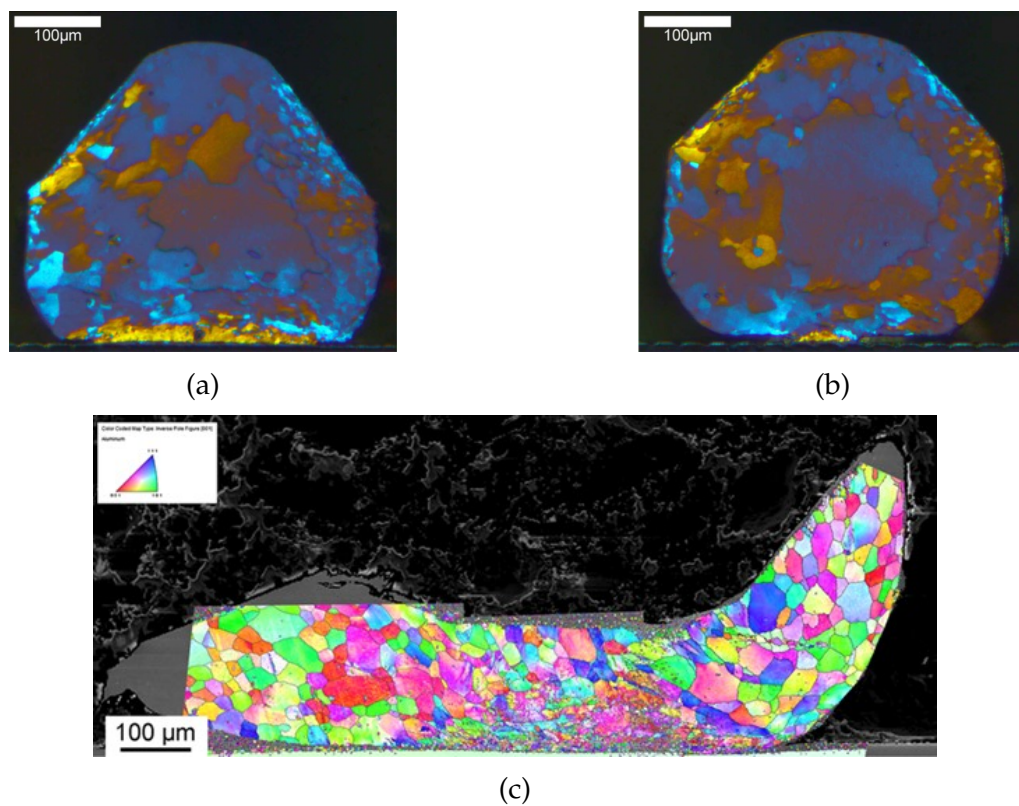


Fig. 2.16: Recrystallization at the cross section cut at (a) the middle in the wire direction [112] (b) the end in the wire direction [112] (c) the middle in the direction normal to the wire [113]

During the bonding process, dynamic recrystallization and recovery take place, especially at the bonding interface. According to Krzanowski and Murdeshwar [28], recrystallization occur more easily in materials with a high stacking fault energy (SFE). SFE is the excess energy associated with stacking faults and determines the mobility of dislocations [114]. A high SFE decreases the required energy for recrystallization. Compared to copper, silver and gold, aluminum has a much higher SFE at room temperature [115]. The occurrence of recrystallization or recovery is in general dependent on the local defect density. If the defect density is high enough to act as a nucleus, a recrystalline tends to form.

Otherwise, recovery arises to reduce the defect density. Throughout the whole bonding process, recrystallization and recovery co-occur.

The distribution of crystals on a 400 μm wire after the recrystallization and recovery is shown in **Fig. 2.16**. In general, the crystals close to the bonding interface are very tiny. The area of the tiny crystals exhibits a half-elliptic shape in both directions (the wire direction and the direction perpendicular to the wire). This region can be enlarged by increasing the US input power [112]. Some of the tiny grains are even in the range of nano-scale and possess a lower hardness than the micro-crystals. These tiny grains were found to be crucial for high reliability [113].

As stated in Section 2.2.3.2, the final hardness of the wire depends on the defect density and the sizes of crystals. Both recrystallization and recovery decrease the density of defects while new defects are generated by deformation and ultrasound. When the amount of newly generated defects is larger than the amount of reduced ones, the defect density is higher after the bonding process [108]. Otherwise, the density of defects decreases [91]. A higher defect density usually increases the material hardness. On the other hand, recrystallization changes the size distribution of grains. In general, the smaller the grains are, the higher yield stress the material has. When the grain goes to nano-range, however, the hardness decreases. With the competition among these factors and with the material's inherent properties (e.g. original defect density and SFE) [90], the final hardness of the wire is determined.

2.3 Other impact factors

2.3.1 Process parameters

During the bonding process, the normal force, US power and process time have significant influences on the process. These factors are usually used to control the bonding process. The determination of "process window", i.e. parameter regions for normal force, US power and process time, is an important step in the set-up of industrial production machines. Since the influences of these factors are highly dependent on each specific bonding machine or even the specific bonding tool, the influences can hardly be quantified. However, a qualitative description of the influences is provided in the following.

First of all, it must be noted that the normal force and the US power are highly interdependent. To transfer a desired amount of US energy to the wire and the bonding interface, a proper normal force has to be selected. Otherwise, most of the US energy dissipates. In general, a medium level of a normal force and an US power should be chosen [116,117]. A small normal force cannot transfer enough US energy to the wire and a large normal force constrains the wire from vibrating. If the applied US power is too small, only a micro-slip is caused and the contact area is small, as insufficient energy is used to soften

the wire; the oxides within the central contact area are unable to be removed and microwelds only form at the peripheral area. These result in a low bonding strength. Too high an US power leads to substantial friction at the wire/tool interface and could destroy the existing microwelds, especially when the US power at the latter stage of the bonding process is too high. A relatively large normal force and a high US power could accelerate the self-cleaning process so that the bonding time can be reduced [50]. When both the normal force and the US power are too high, however, the wire and even the substrate are over-deformed and problems like heel weakening or cratering can occur. A proper process time needs to be set as well. If the process time is not sufficient for microwelds growth, the required bonding quality cannot be achieved. When the process time is too long, the process enters an over-bonding stage, in which a large relative displacement amplitude takes place at the wire/tool interface and some of the existing microwelds can be damaged. According to [118], the influence of the process time is more significant when the US power is low. After the bonding conditions are specified, a design of experiments (DOE) shall be conducted to find the process window, within which a good bonding quality is achieved and the influence of the process parameters on the bonding quality is insignificant [119,120].

2.3.2 Surface condition

The surface conditions, including the material hardness, the smoothness and the existing contaminants, significantly influence the bonding quality.

In general, a smooth and soft surface offers larger process windows [119] while a rough surface facilitates the bond formation as long as the roughness is smaller than a critical value [121]. The effect of the surface roughness on Al-Al and Al-Au bonding was first analyzed by Riben et al. [122] and a surface roughness of less than 3 μ inch (0.0762 μ m) was suggested to provide good bondability. In another work [28], it was claimed that the roughness of an aluminum substrate is irrelevant to the bonding quality. The different results might come from the surface hardness which was not mentioned and the pull tests

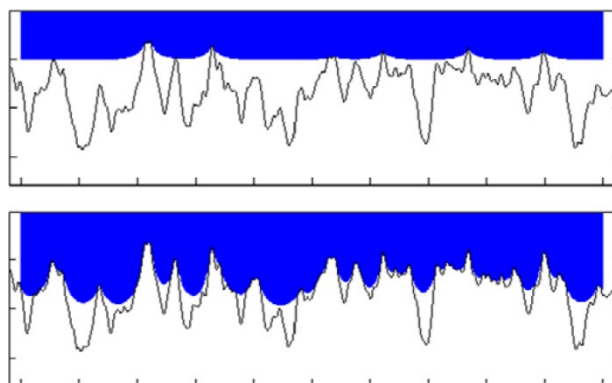


Fig. 2.17: Penetration of a soft material into a hard material without and with softening effect [39]

which highly depend on the deformation of the bond heel. By evaluating the Al bonds on Nickel-Phosphorus films, Onuki et al. [123] stated that the shear strengths of the bonds were independent of the film hardness and on the film roughness when it was less than $0.3 \mu\text{m}$. The hardness range of the tested films, however, seems to be very high so that the influence is ignorable. In the analysis of Al-Cu bonding [121], it was found that the bonding strength decreased and became sensitive to the roughness when the roughness exceeded a certain value. Despite the achieved higher bonding strength and reliability with smooth surfaces, Khaja et al. [124] found that a smooth surface required a longer process time as the friction induced thermal energy decreases. This is also supported by the theoretical model and experimental results of Jeng and Horng [125], who claimed that the substrate roughness is important for the contact temperature increment and thus for a good bond. The asperity deformation of the bonding partners was emphasized by Murali et al. [94] and the roughness must be controlled to make the required deformation achievable. The influence of the roughness can be attributed to the penetration of the bonding partners when one is softer than the other, as shown in **Fig. 2.17**. When the roughness is smaller than a threshold value, the soft wire can easily penetrate the valleys so that the real metal-metal contact area increases. This area becomes much smaller if the roughness is larger than a threshold value.

As mentioned before, common contaminants like oxides, carbon and water vapor have to be taken into account as they are often present on the contact surfaces before bonding. Among these contaminants, oxides are the most critical contaminant. For aluminum wire bonding, the oxide scale is easy to remove due to its high hardness and small thickness. Even for ball-wedge bonding which is more sensitive to contaminants, a 20 nm aluminum oxide layer does not decrease the bonding quality [126]. When the oxide layer is softer and thicker, like copper oxide, the removal process becomes more difficult. As a result, a copper substrate that is covered by a protection layer, like aluminum, is preferred [38, 64].

Relatively few works investigated the influence of the surface roughness and smoothness on the removal of contaminants. The main study on this was conducted via a deposition of a 40 nm carbon layer on different substrates with different roughnesses and hardnesses [28]. With this amount of carbon contaminant, a smooth and hard substrate did no longer offer a good bond since both the valleys and tips were covered by carbon. An increase in the roughness allowed a larger mated metal contact area and led to a higher bondability. A soft substrate was hardly influenced by the carbon layer.

2.4 Energy flow

Based on the above described state-of-the-art knowledge, a chart of energy flows was derived. It is shown in **Fig. 2.18** and helps to better understand the bonding process. The energy flows in (b) correspond to the components and the interfaces of the wire bonding system in (a).

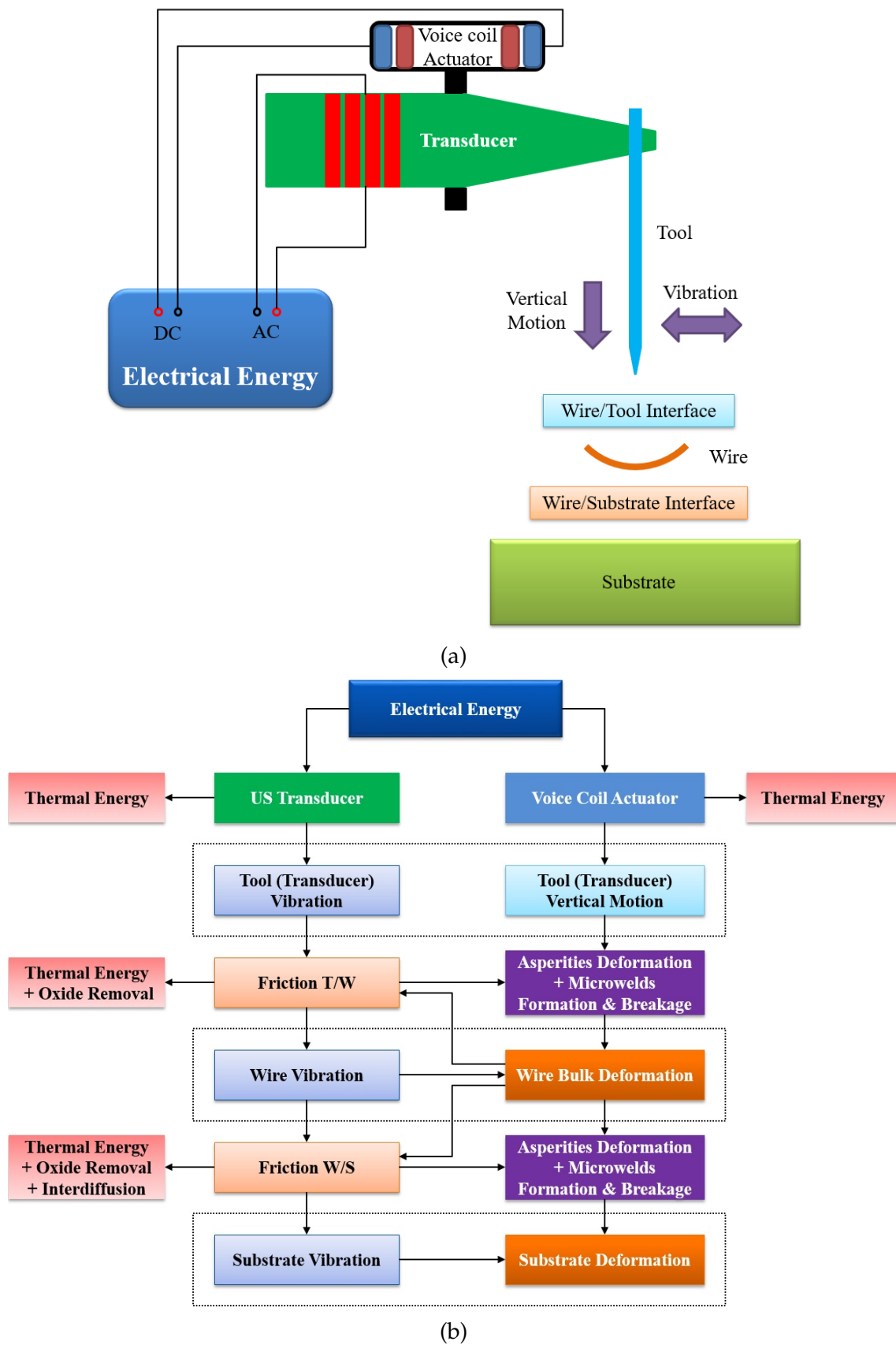


Fig. 2.18: (a) Wire bonding system (b) Energy flow during the US wire bonding process

The electrical energy from the power supply flows to the two components of the bonding head: the US transducer and the voice coil actuator. The US transducer generates the US vibration and the voice coil actuator generates the normal force. A certain amount of electrical energy is dissipated in these two components and converted to thermo- and radiation energy. The main energy flow is directed to generate vibration and vertical motion on the tool via which the energy is transferred to the bonding domain.

The vibration energy of the tool is first transferred to the wire/tool interface. On one hand, the sliding of the tool on the wire generates heat and induces the removal of oxide. On the other hand, the friction leads to the deformation of asperities as well as to the formation and breakage of microwelds. The vibration is then sequentially transferred to the wire. A certain amount of energy is required for the kinetic motion of the wire while another amount of energy is needed to soften the wire. The rest of the energy passes to the wire/substrate interface. As with in the wire/tool interface, the energy flows into heat generation, oxide removal, deformation of asperities, the formation and breakage of microwelds. Additionally interdiffusion takes place at this interface. Since the wire/substrate interface is the bonding interface, more energy is used for asperity deformation as well as microwelds formation and breakage. It must be noted that the sliding friction significantly influences the microwelds formation and the newly formed microwelds reversely affect the friction. The energy to the substrate causes the vibration and deformation of the substrate.

The energy from the voice coil actuator is essential to the bonding process. This energy is transferred to the wire for the plastic deformation of asperities and the bulk material of the wire. Due to the big volume difference, most energy flows to the bulk deformation of the wire. The bulk deformation induced material flow further increases the friction at the two interfaces. The remaining energy flows to the substrate for the deformation of the substrate. The recrystallization and recovery take place during the deformation of wire and substrate. The energy comes from both the transducer and the voice coil actuator.

3 Objectives

Based on the description of the mechanisms which are involved in the bonding process, it is clear that a big knowledge gap exists for the friction phase and the softening phase, even from a qualitative point of view. In this chapter, specific open questions are stated by analyzing the state-of-the-art. The objectives of the dissertation are then determined. Finally, hypotheses and methods for solving the open questions are proposed.

3.1 Analysis of the state-of-the-art

The state-of-the-art of knowledge on the bonding mechanisms has been discussed in the previous chapter and a four phases model has been used to structure the temporal sequence. The pre-deformation and activation of vibration phase as well as the interdiffusion phase has been extensively modeled and experimentally studied. The friction phase and the softening phase are still not well understood due to their complexity and because of the highly dynamic changes which occur during these phases of the bonding process.

To achieve a high bonding strength and reliability, the wire bonding process is usually performed under conditions of gross-slip. As a result, the friction at the wire/substrate interface was analytically described by a stick-slip model [49,50]. The vibration amplitude of the substrate can usually be ignored as it is much smaller than that of the wire, especially for heavy wire bonding where a large vibration amplitude of the transducer is provided. As a result, the vibration induced relative motion at the wire/substrate interface can be roughly considered to be dominated by the vibration of the wire. At the wire/tool interface, however, the relative motion depends on the motion of both the wire and the tool. Even though the real-time velocities of the wire and the tool have been measured by laser vibrometers [73], the information which can be exposed is limited due to the size of the laser beam, the deformation of the wire and the positions of the measurement spots. In addition, the relative motion at the wire/tool interface is more complex than the sliding between two rigid bodies, enlightened by the Mindlin model [42] description on the micro-slip behavior at the wire/substrate interface. This is a difficult issue to deal with since the wire/tool interface is not touchable by any investigation tools during the bonding process.

A more difficult open question is about the contaminant removal mechanism during both

the friction and the softening phases. It is only known that pre-deformation causes cracks and the discretized oxides are then detached and transported by the vibration induced relative motion and the plastic deformation induced material flow, as shown in Fig. 2-9. The details on the crack generation and distribution, the impact of vibration and material flow on the detachment and transportation of oxides, have not yet been detected. Also, the impact of process parameters on the detachment and transportation of oxides, the transportation paths and the motion behavior of oxides, need further studies. When these open gaps can be reduced, it might be possible to develop some methods for enhancing the removal speed and clean area.

The US bonding process is not quantitatively understood. As mentioned in Chapter 2, the bonding process includes relative motion, vibration induced friction, plastic deformation induced friction, oxide removal, ultrasonic softening, microwelds formation and interdiffusion. Even though the different mechanisms have been extensively measured and modeled, it is still difficult to describe them in a quantitative way. Until now, only the vibration induced friction energy was calculated. There has been no model which states energy flows from the electrical power supply to the different mechanisms. A quantification of such an energy flow model greatly will result in a better understanding and further enhancements of the bonding process.

3.2 Objectives

Based on the analysis of the state-of-the-art, the objectives of this dissertation are defined as follows:

- Quantify the relative motion at the wire/tool interface and the wire/substrate interface;
- Clarify the oxide removal process;
- Determine the impacts of vibration induced relative motion and the continuous plastic deformation induced relative motion on the oxide removal process;
- Quantify the energy flows during the bonding process;

3.3 Methods of solution

Experimental investigation on relative motion

The most prominent phenomenon - the relative motion behaviors at the two interfaces will be investigated experimentally. The technique of optical high-speed observation will be applied to record the relative motion behaviors. After the recording, the motion of tool and wire during the bonding process will be automatically tracked by a computer

vision technique. Finally, both the deformation induced relative motion and the vibration induced relative motion are supposed to be separated and quantified.

Experimental investigation of the oxide removal process

The oxide removal process is usually detected by observing the distribution of oxides after the bonding process and the removal of wire. Only little information can be exposed by this method. Instead, in this work the oxide removal process will be directly observed by replacing the metal substrate with a transparent glass. The natural oxide covered on aluminum is only five nanometers and could be hardly observed. To solve this problem, a relative thick layer of oxide will be deposited on the wire or the substrate. By analyzing the changes of the coated layer during the bonding process, the whole removal process from cracking to transportation will be clarified. The functions of vibration induced relative motion and the continuous plastic deformation induced relative motion on the oxide removal process will be specified by varying the coatings.

Analytical calculation of energy flows

Due to the complicated changes at the contact interfaces, it is currently not possible to develop a model of the bonding process which can include all the factors and phenomena. If the above methods are applicable, however, the energy flows during the bonding process can be calculated and used to quantitatively describe the bonding process. Based on the information recorded by the high-speed videos, the friction energies at the two interfaces and the kinetic energy of the wire can be calculated. In addition, the vertical displacement of the tool shall also be recorded by the videos. Therefore, the work done by the voice coil actuator can be obtained. With additional information including the final microwelds area, final interface area and the total work for the bulk deformation of the wire, an approximation of the other energies is achievable.

4 Investigations on relative motion

In order to determine the relative motions at the wire/tool interface and the wire/substrate interface during the bonding process, the motions of the wire and the tool were recorded in real-time. The motion paths of the wire and the tool were then tracked and quantified by a mean-shift technique. The normal force and the US power were varied to study their impacts on the relative motion behaviors. In addition, the different relative displacements at the different locations of the wire/tool interface were illustrated by the change of the wire surface topography and the change of the coating elements. Some contents of this chapter have been published in [127–129].

4.1 Experimental setup

An experimental test bench including the US wire bonding platform, the high-speed observation system and the illumination system was established. The three subsystems are described in the following subsections.

4.1.1 US wire bonding platform

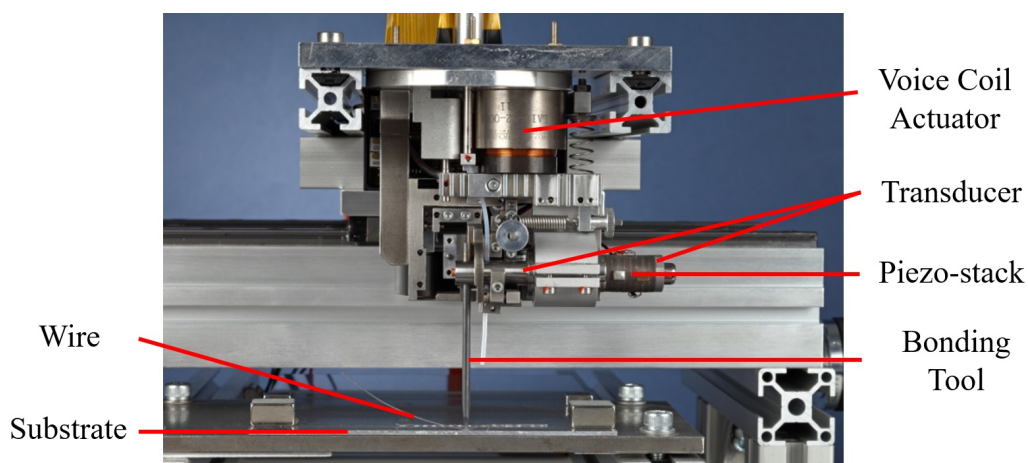


Fig. 4.1: Heavy wire wedge-wedge bonding head HBK05 from Hesse Mechatronics GmbH

In order to closely monitor the bonding process, a manual thick wire wedge-wedge bonding platform was constructed. The core part is the bonding head HBK05 provided by Hesse Mechatronics GmbH, as shown in **Fig. 4.1**. It mainly consists of a voice coil actuator, an US transducer and a $400\ \mu\text{m}$ bonding tool. The voice coil actuator is used to provide the normal force. The transducer is operated in its longitudinal mode and must be controlled to generate a large vibration amplitude during the bonding process. The bonding tool is fixed to the end of the transducer and vibrates at its bending mode.

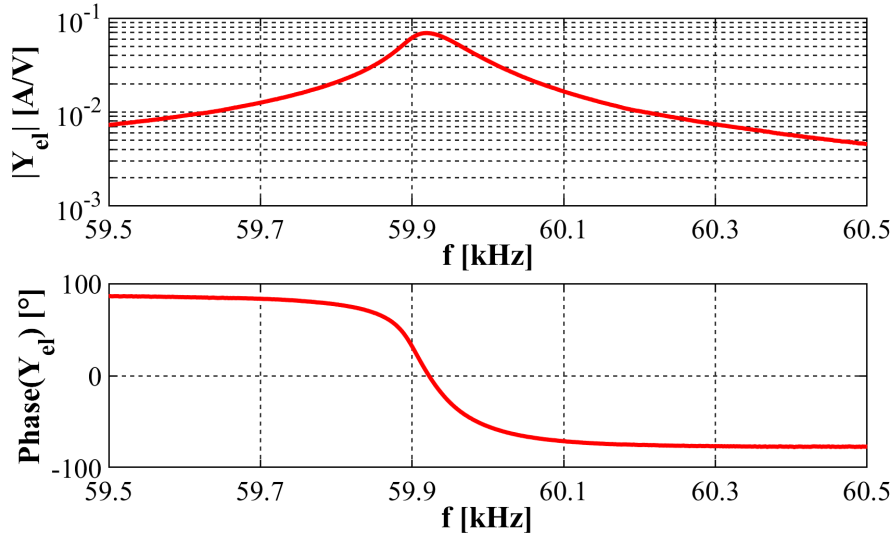


Fig. 4.2: Electrical input admittance of the transducer

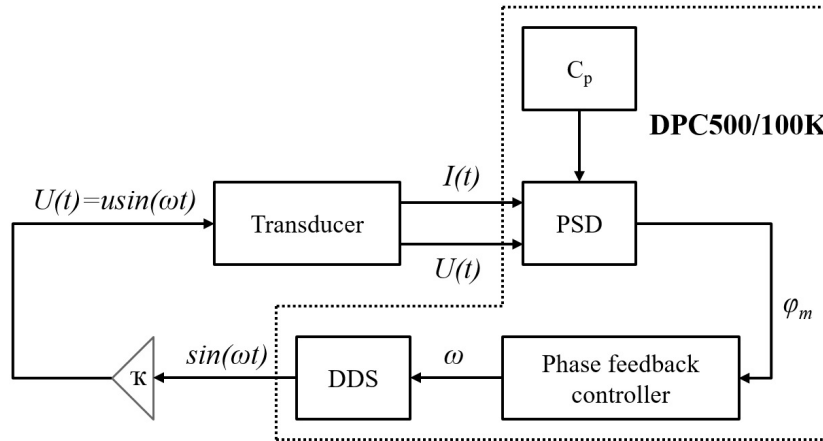


Fig. 4.3: Phase locked loop control with DPC500/100K

The transducer was excited by harmonic input voltage and the excitation frequency was swept from 59.5 kHz to 60.5 kHz with a step of 2 Hz. The absolute value of the electrical input admittance and the corresponding phase between the voltage and the current are shown in **Fig. 4.2**. From the figure, it can be seen that the eigenfrequency of the transducer is around 59.92 kHz. The transducer was controlled and driven by a digital phase controller DPC500/100K [130] and a Brüel & Kjær 2713 amplifier. The controller DPC500/100K was developed in-house. It applied a phase locked loop control to keep the transducer running at its resonance frequency throughout the bonding process. As shown in **Fig. 4.3**, the monitored values of the input voltage and current were transferred to the

controller in real time. The phase sensitive demodulation (PSD) calculated the phase difference φ_m between the voltage and the current. φ_m was sent to the phase feedback controller to calculate an angular frequency ω for achieving the new resonance frequency. The sinusoid voltage signal from the Direct Digital Synthesizer (DDS) was then amplified and used to drive the transducer.

The bonding head and the aluminum bonding substrate were installed on a linear stage. The wire used in this work is Al-H11 from Heraeus GmbH. The material of Al-H11 is annealed aluminum with a high purity (>99.999%). The 400 μm wire has a breaking load of 500~700 cN with an elongation of more than 5%. The roughness of the wire surface was measured to be $R_a = 342.5 \text{ nm}$.

4.1.2 High-speed observation system

Due to the high frequency of the vibration and the dynamic changes of the mechanisms described in Chapter 2, a high-speed observation system was required to capture the relative motions. The system in this work was constituted by a high-speed camera and a magnification system. The camera is a Phantom v710 from Vision Research Inc. The full window size of the camera is 1280 x 800 pixel. Due to the technical limitations of the camera, the large window size must be sacrificed to achieve a high recording rate. The window sizes and the corresponding frame rates used in this work are listed in **Table 4.1**. As shown in the table, the highest frame rate with the smallest window size is almost six times greater than the bonding frequency of 59.92 kHz, which means 6 frames can be obtained for each vibration cycle. In other conditions, only one frame is recorded within one, two or three vibration cycles. However, it is still possible to capture the motions. This will be shown in the further sections of this chapter as well as in the further chapters of the dissertation.

Table 4.1: Window sizes and the corresponding frame rates

Window size (pixel)	640 x 480	512 x 384	320 x 240	128 x 64
Frame rate (fps)	20,000	30,008	60,017	350,515

The CMOS sensor of the camera has a pixel size of 20 x 20 μm . The common vibration amplitude of the tool for thick wire bonding is, however, only 4-6 μm . Without magnification, this pixel size is too big to capture the motions of the tool and the wire. To compensate for this, a magnification system was integrated to enhance the resolution. Due to its simplicity and low cost, a reverse lens technique was selected. The reverse-lens magnification system includes a black bellow, a commonly used optic lens and a corresponding reverse ring to the lens. The setup of the high-speed observation system is shown in **Fig. 4.4**. The selection of a proper lens is the most essential factor to obtain a high magnification. Together with the bellow shown in **Fig. 4.4**, the use of a Canon 50 mm lens led to a magnification of 3.5X while the application of a Pentax 12.5 mm lens resulted in a magnification of 18X. An even greater magnification can be reached by selecting a



Fig. 4.4: High-speed observation system

lens with a shorter focal length. The depth of field, however, became too small and sharp images were hard to achieve. Finally, the Pentax 12.5 mm f1.4 lens and the resulting resolution of $1.1 \mu\text{m}/\text{pixel}$ was chosen as the best compromise. The depth of field with the Pentax lens was still not large enough to simultaneously focus on both the tool and the wire. For our purpose, however, a fuzzy profile of the tool was acceptable since the tool can be considered a rigid body. Therefore, the motions of both the tool and the wire can be captured by this configuration.

The sharpness of images is dependent not only on the depth of field, but also on the motion of the objects. If the objects move too much within the exposure period, it will result in blurry object contours. Since the frequency of vibration is 59.92 kHz, one vibration cycle takes $16.69 \mu\text{s}$. If the vibration amplitude is $\sim 5 \mu\text{m}$, an average speed is calculated to be $1.09 \text{ pixel}/\mu\text{s}$. During preliminary experiments, it was found that a movement of more than 2 pixels caused blur. As a result, a $2 \mu\text{s}$ exposure time was chosen as the maximum limit to obtain sharp images. At the same time, enough light had to be provided within such a short period so that bright images could be obtained.

4.1.3 Laser illumination

In order to obtain bright images in this extremely short exposure time ($2 \mu\text{s}$), enough light had to be provided during the recording. However, most of the illumination light is lost on the illumination path:

1. The majority of the light from the light source is lost due to the projection angle of the light source, the long distance between the light source and the site of interest, and the small size of the site of interest. A commonly used light source usually has a large projection angle. Since the 12.5 mm Pentax lens was selected, the distance between the bonding site and the lens was fixed. Due to this small space, the large light source could not be placed at a close distance to the bonding site. In addition, as already stated, the bonding site is very small. Considering that a window size of

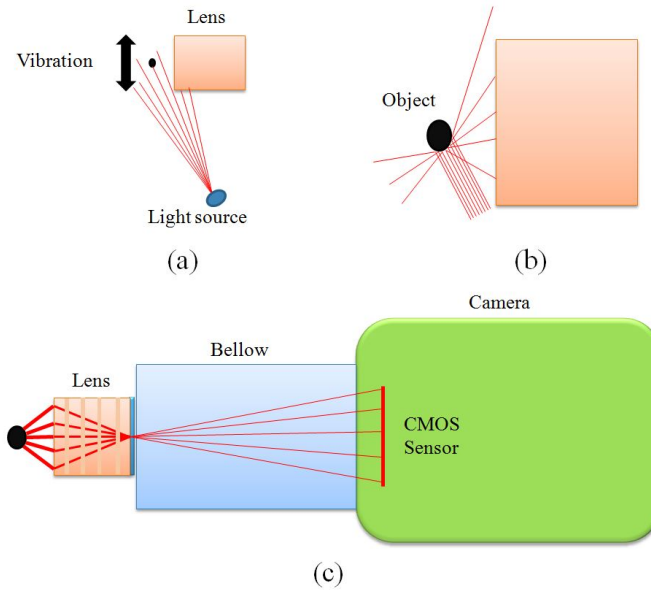


Fig. 4.5: Illumination route from the light source to the sensor

512 × 384 pixel is taken, the site of interest is only 563.2 μm × 422.4 μm. As illustrated in Fig. 4.5(a), the light reaching the bonding site becomes very small.

2. A big portion of the light from step 1 is lost due to the large injection angle and the shape of the reflection surface. For the same reason as in step 1 (the 12.5 mm distance between the object and the lens), the injection light has to come from the side of the lens. The resultant minimum injection angle is approximately 60°. Due to the plastic deformation of the wire, its surface area is not parallel to the lens. As shown in Fig. 4.5(b), only a small portion of the light from step 1 is reflected into the lens.
3. After entering the lens, the light has to pass a couple of glasses as well as the bellow. The light reaching the sensor is thus further reduced, as shown in Fig. 4.5 (c).

In order to obtain a high intensity of light, a laser was selected as the light source. In this work, a JOLD-45-CPXF-1P laser from Jenoptik AG was used. The laser has a maximum power of 45 W and a wavelength of 804 to 808 nm depending on the applied power and temperature. The laser power that reached the bonding site was around 200 mW. This illumination energy caused an temperature increment of the wire during the bonding process. If heat conductivity is not taken into consideration, the temperature increment of the wire can be calculated as:

$$\Delta T = \frac{(1 - R_{808})Pt}{\rho\pi(\frac{d}{2})^2lc_p} \quad (4.1)$$

where R_{808} is the reflectance of the material for 808 nm light; P is the laser power reaching the bonding site; t is the processing time; ρ is the density of the wire material; d is the diameter of the wire; l is the length of the wire within the recording window; c_p is the

mass heat capacity of the wire material. The calculated result for a $400\ \mu\text{m}$ aluminum wire within a 50 ms processing time is 7.76 K.

Since the tool is made of tungsten carbide and both the wire and the substrate are made of aluminum, they all have high heat conductivities (aluminum: $237\ \text{W/m}\cdot\text{K}$; tungsten carbide: $110\ \text{W/m}\cdot\text{K}$). Therefore, large amount of the heating energy within the recording region was transferred to the other regions. In addition, due to the plastic deformation of the wire during the bonding process, the absorption area of the wire decreased. Thus less laser energy entered the wire. As a result, the real temperature increment was smaller than the calculated value. This leads to the conclusion that the laser illumination induced temperature increment insignificantly influenced the bonding process.

4.2 Investigation of relative motions

The bonding domain and the positions of the recording windows are shown in **Fig. 4.6**. Since aluminum possesses a very high reflectivity, the substrate looks like a mirror and reflects the wire and the tool into the videos. To record the relative motion at the wire/substrate interface, the size and location of the recording window were selected as shown by the green rectangular (320×240 pixel) in **Fig. 4.6**. A smaller recording window, the red rectangular (128×64 pixel), was also selected so that a much higher recording rate could be obtained. In order to make the tracking of the wire motion easier, the right end of the wire was cut. Therefore in the resulted images (**Fig. 4.7** and **Fig. 4.8**), a clear edge is observed and the right part is dark, as no wire was there to reflect the illumination light. The relative motion between the wire and the tool was recorded within the blue window (512×384 pixel). It was selected due to two reasons. First, compared to the right fillet, the left fillet of the tool has a smaller radius. Locating the recording window on the left side of the tool thus facilitated the recognition of the wire/tool interface. Second, due to the continuous plastic deformation of the wire, the tool moved downwards during the bonding process. The use of a large window size confirmed that the tool always stayed inside the window throughout the entire bonding process.

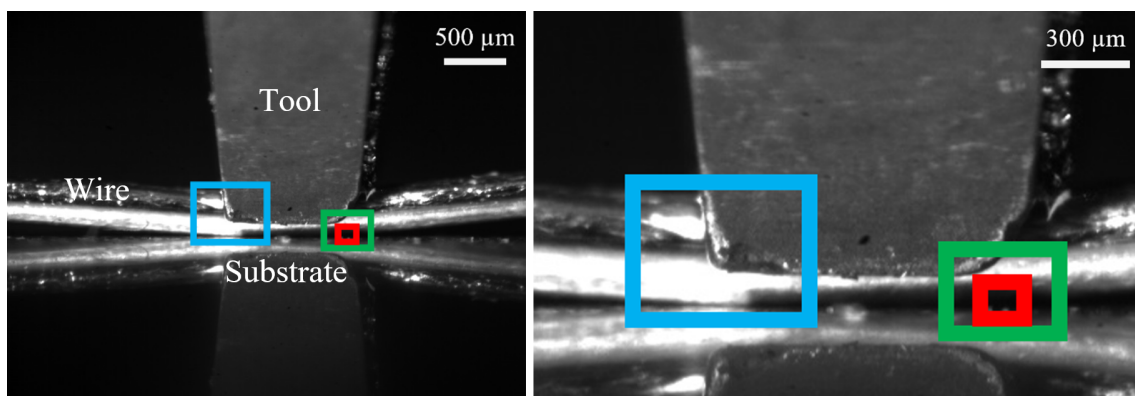


Fig. 4.6: Positions of recording windows

4.2.1 Relative motion at the wire/substrate interface

To capture the relative motion between the wire and the substrate, a relatively large window size of 320×240 pixel was first used (the green window in Fig. 4.6). A normal force of 10 N was applied to show the existence of relative motion under a large normal force. The US power was around 17.5 W and the process lasted for 50 ms. Two series of images were taken from the video to show the relative motion behavior. As shown in Fig. 4.7, the right illustrations show the boundaries of the bonding partners. The blue line represents the wire/substrate interface; the red line represents the edge of the wire; the green lines were drawn to compare the horizontal positions of the wire edge.

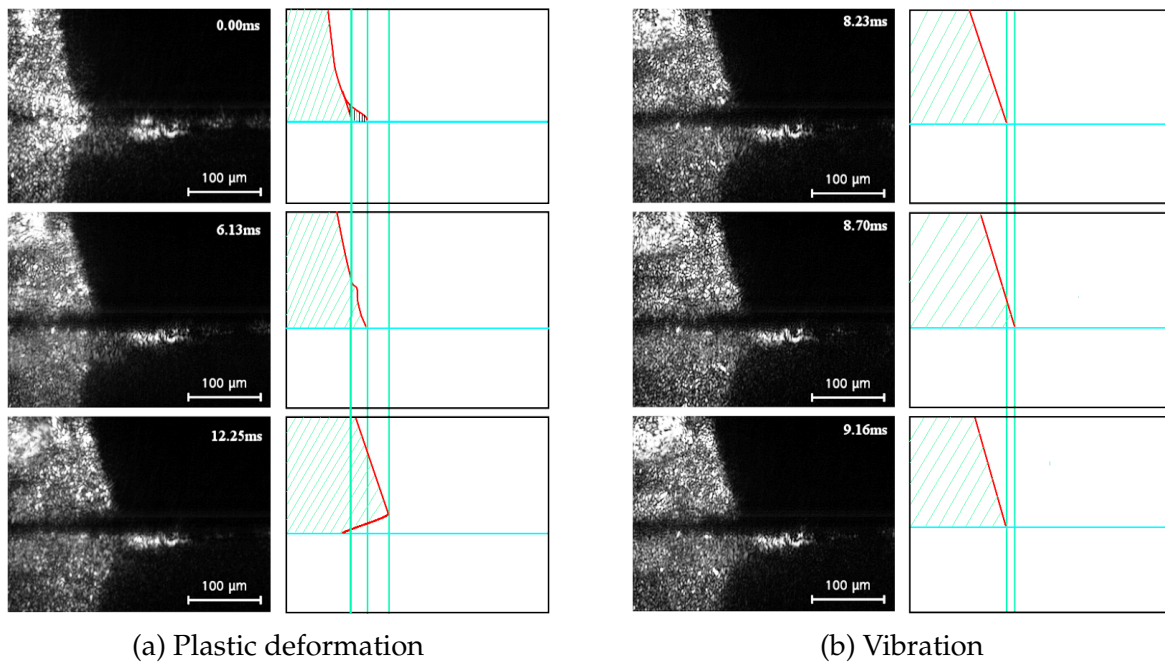


Fig. 4.7: Relative motion at the wire/substrate interface

The relative motion at the wire/substrate interface consists of two components including continuous plastic deformation and vibration. Three images at 0.00 ms, 6.13 ms and 12.25 ms were selected in Fig. 4.7 (a) to show the continuous plastic deformation. 0.00 ms indicates the start of the US vibration. By comparing the green lines (the right end of the wire), it can be seen that the wire moved rightwards in the first 12.25 ms. In the video, the continuous moving rightwards of the wire was observed. This indicates that the wire was horizontally enlarged and the plastic deformation of the wire took place. The shadow in the 0.00 ms illustration image represents a particle generated during cutting the wire. Due to the vibration, the particle was later on separated from the wire. The plastic deformation was caused by the Acoustoplastic Effect (APE).

Three images of an observation cycle were selected in Fig. 4.7 (b) to show the vibration component of the relative motion. Since the recording rate (60017 fps) of the video was similar to the bonding frequency (59920 Hz), only one frame was recorded per US vibration cycle. Due to the phase difference, the vibration of the wire could still be captured.

However, the observed vibration cycle in the video was no longer a single US vibration cycle. Instead, one observation cycle consisted of tens of US vibration cycles. For the process shown in **Fig. 4.7 (b)**, one observation cycle consisted of ~ 56 US vibration cycles. In other words, ~ 56 frames were sampled at different phases of the observation cycle to show the back and forth motion of the wire. The three images in **Fig. 4.7 (b)** corresponded to 0° , 180° and 360° of an observation cycle. The vibration induced relative motion was thus shown by the green lines. The zero-peak vibration amplitude is around $5.5 \mu\text{m}$ which is within the expected range of $4\text{--}6 \mu\text{m}$ for thick wire bonding. On the other hand, no movement of the substrate was observed, which indicates the vibration amplitude of the substrate is less than $0.55 \mu\text{m}$. As a result, the relative motion between the wire and the substrate can be measured approximately by solely tracking the vibration of the wire.

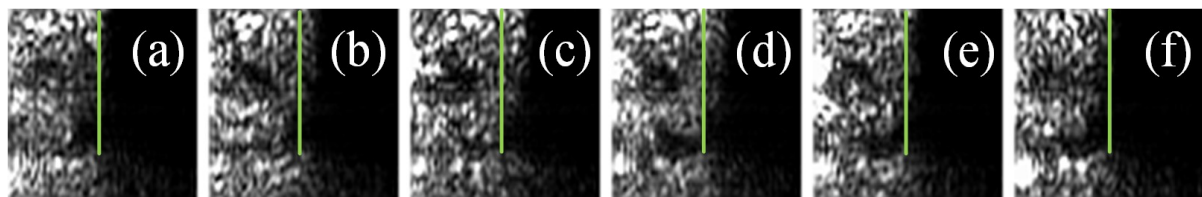


Fig. 4.8: A single vibration cycle of the wire (a) 1.97138 ms (b) 1.97424 ms (c) 1.97709 ms (d) 1.97994 ms (e) 1.98280 ms (f) 1.98565 ms (the size of each image is $71.1 \times 71.1 \mu\text{m}$)

In order to show the vibration induced relative motion within a single US vibration cycle in real time, the window size was decreased to 128×64 pixel and a recording rate of 350515 fps was achieved. The same bonding parameter setting as the last bonding process was applied. Since there was no obvious plastic deformation in the beginning, six frames at ~ 1.97 ms were taken from the video to show the vibration of the wire in a single US vibration cycle. In these images, the wire stayed in the very left part of the images and the right part of the images remained dark. To more conveniently show the relative motion, the six images were cut to 64×64 pixel as shown in **Fig. 4.8**. The vertical green line stands for the initial position of the wire edge. By comparing the green line and the wire edge, the vibration of the wire can be distinguished. The vibration amplitude shown in the figure is $4.4 \mu\text{m}$ which is also common for thick wire bonding. To the best knowledge of the author, this is the first time that the motion of the wire was observed within a single US vibration cycle.

4.2.2 Relative motion at the wire/tool interface

The recording window was set to the blue rectangular (512×384 pixel) as in **Fig. 4.6** to capture the relative motion between the wire and the tool. The corresponding recording rate was 30008 fps and one frame per two vibration cycles was obtained. Due to the phase difference between the bonding driving signal and the recording rate, the motion of the tool and the wire were captured. The exposure time was $2 \mu\text{s}$. The focal plane was the upper part of the wire. The relative motion at the wire/tool interface during the 9 N, 17.5 W bonding process is shown in the following figures.

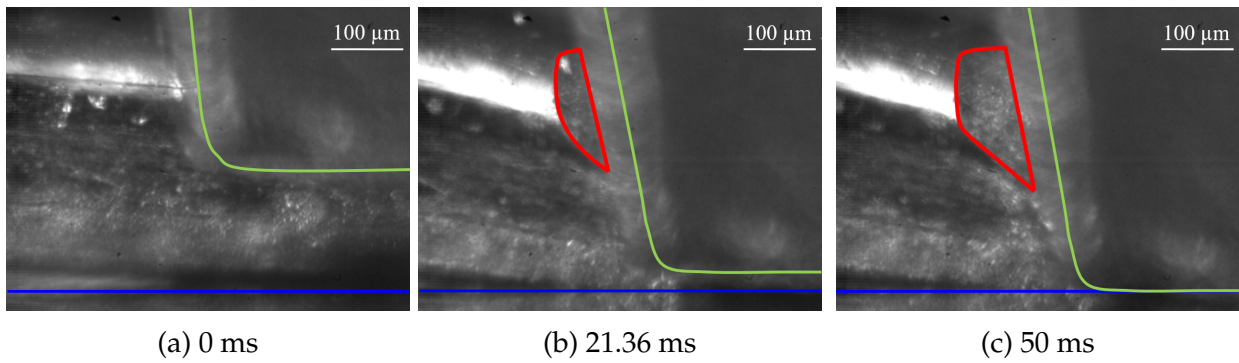


Fig. 4.9: Continuous plastic deformation induced relative motion at the wire/tool interface

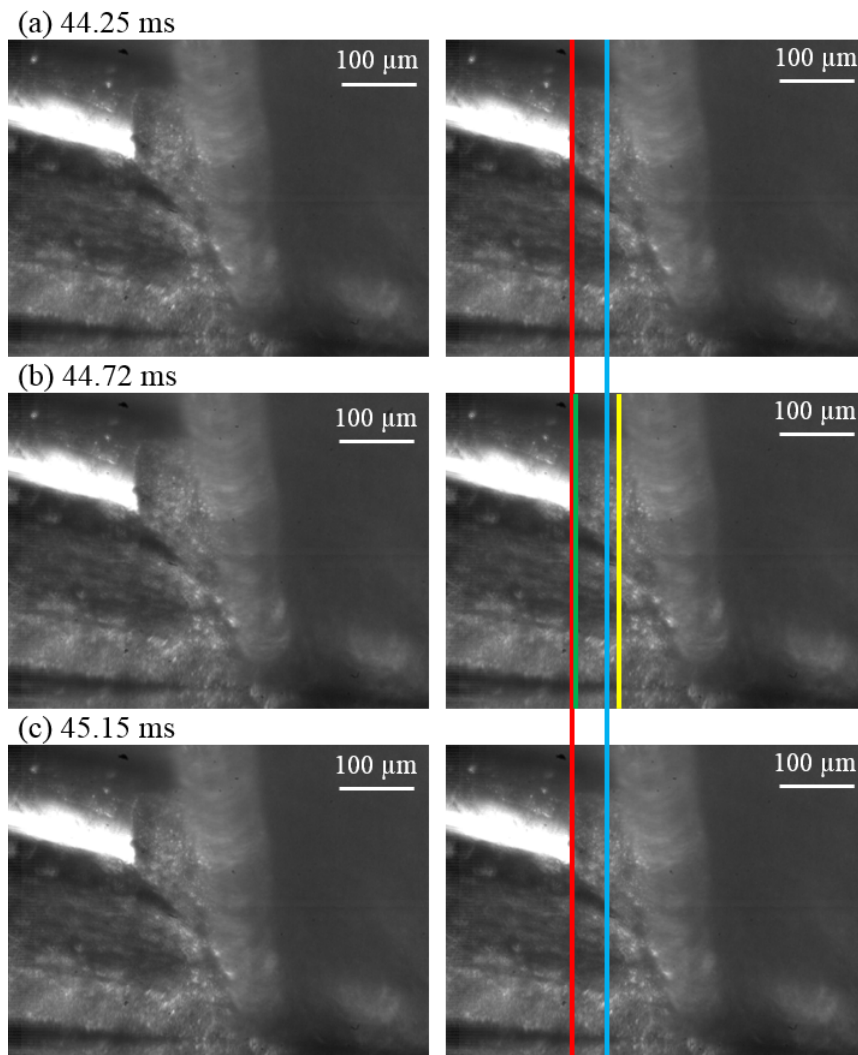


Fig. 4.10: US vibration induced relative motion at the wire/tool interface

The relative motion between the wire and the tool also has two components. The continuous plastic deformation induced relative motion is shown in **Fig. 4.9**. The blue lines represent the substrate surface and the green lines show the profile and the position of the tool. The vertical deformation of the wire is indicated by the decrease of the distance between the tool and the substrate from (a) to (c). This distance totally vanishes in (c) where the tool and the substrate are in contact. The deformation induced horizontal relative motion is directly indicated by the fillet contact surface of the wire, as marked by the red curves in (b) and (c). In the beginning (see (a)), this fillet contact area cannot be observed. After around 12 ms, this area became visible. And from then to (c), this area got larger and larger. The final relative displacement indicated by (c) is approximately $89.1 \mu\text{m}$.

Fig. 4.10 shows the vibration component of the relative motion. The images on the left are the original frames of the video. The four lines imposed on the same images on the right indicate the relative motion. The red line and the blue line represent the initial position of the wire and the tool in the observation cycle from (a) to (c), respectively. An observation cycle in this video contains ~ 60 US vibration cycles. The green line and the yellow line represent the right-most position of the wire and the tool, respectively. It can be seen that the vibration amplitude of the wire at this late stage of the bonding process was very small ($\sim 2.2 \mu\text{m}$) while the relative motion between tool and wire became large ($\sim 4.4 \mu\text{m}$).

4.3 Quantification of the relative motions

Since the bonding process lasted ~ 50 ms and the recording rate was 30008 fps, ~ 1500 frames were recorded for each process. The motions of the wire and the tool in these frames were tracked via the mean shift method in MATLAB. The mean shift method is a non-parametric iterative algorithm that is widely applied in computer vision. It combines the coordinate space and the feature space to define and search for the target vectors in a series of images [131]. The target vectors were defined by selecting two areas on the wire and the tool (one for each, see **Fig. 4.11(a)**). These areas have unique brightness distributions and thus they can be distinguished. The motions in both x (horizontal) and y (vertical) directions in the following frames were tracked and shown in **Fig. 4.11 (b)** and **(d)**, respectively. Due to the plastic deformation of the wire, the vertical displacement of the tool is clearly visible ($113.7 \mu\text{m}$) in **Fig. 4.11(d)**. Comparably, the vertical motion of the selected region, which was due to the bending of the wire, is ignorable. Since the motion of the tool and the wire on the horizontal x -axis plays an essential role in the bonding process, the motion on x -axis is the focus of the work.

From the motion of the tool on the x -axis (the green curve in **Fig. 4.11 (b)**), it can be seen that a shift of the equilibrium position of the tool occurred. This might be due to the unbalanced stress distribution generated during the normal force loading. In the latter stage, the equilibrium position of the tool stayed the same. The vibration of the tool

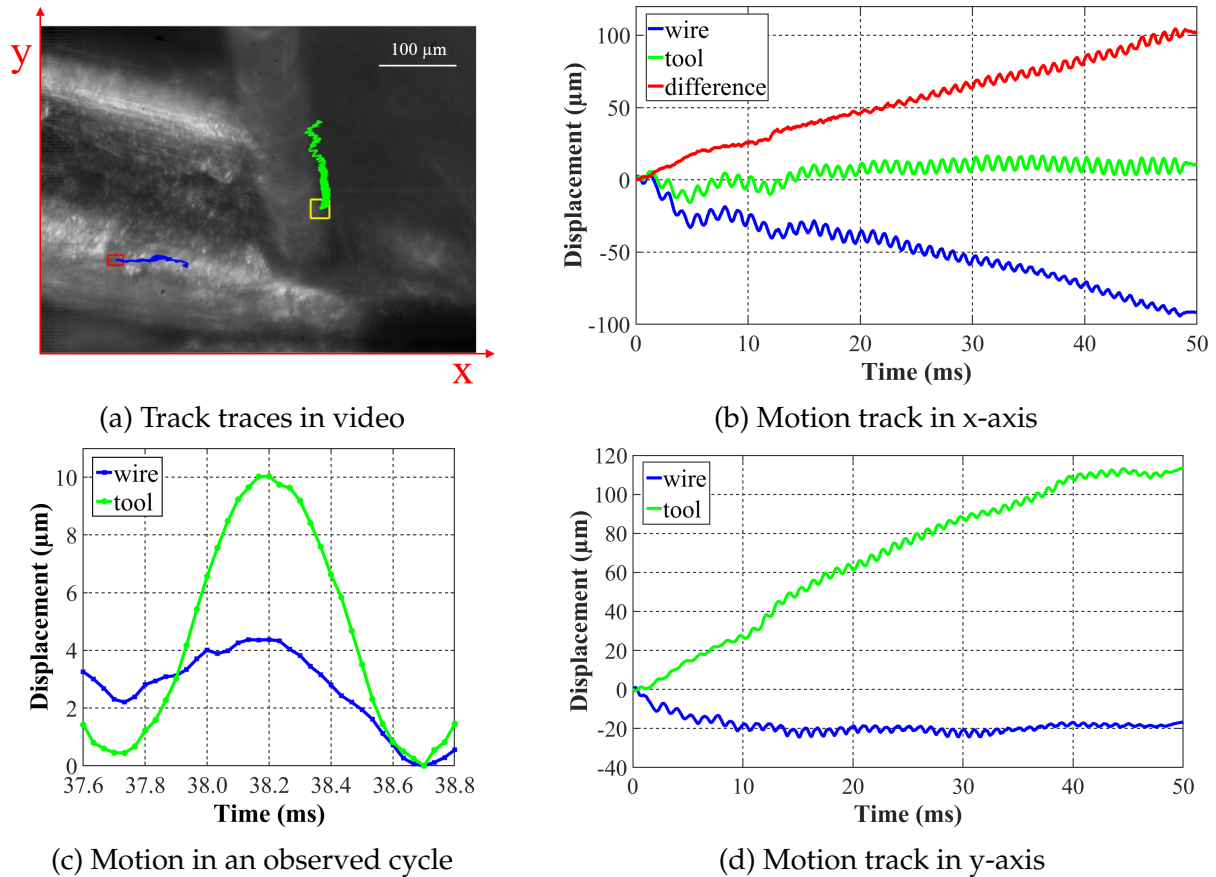


Fig. 4.11: Motion track of wire and tool under 7.5 N, 17.5 W

can be clearly observed. The motion track of the wire on the x-axis (the blue curve in Fig. 4.11 (b)) shows two components of the wire motion - the continuous plastic deformation, which results in an increase of the length of the wire, and the vibration. The final plastic deformation is about $90 \mu\text{m}$. The vibration amplitude of the wire became smaller and smaller as the process went on.

The red curve in Fig. 4.11 (b) represents the relative motion between the wire and the tool. As discussed before, the blue curve can be considered as the relative motion between the wire and the substrate. Both of them contain the two components described in Section 4.2. In the beginning stage, the tool and the wire were well coupled and their vibration amplitudes were similar. The two curves drifted apart due to the continuous plastic deformation. The final deformation induced relative displacement is around $100 \mu\text{m}$. As more and more microwelds were formed between the wire and the substrate, the bottom surface of the wire became more and more constrained. As a result, the vibration induced relative displacement amplitude between the wire and the substrate became smaller and smaller. In contrast, the vibration induced relative displacement amplitude between the wire and the tool was enlarged. The motion tracks of the wire and the tool in the observation cycle (~ 30 US vibration cycle) around 38.2 ms are magnified and shown in Fig. 4.11 (c). Obvious vibration induced relative motion can be seen in the figure.

Due to its large stiffness, the tool can be regarded as a rigid body. Therefore, the selection

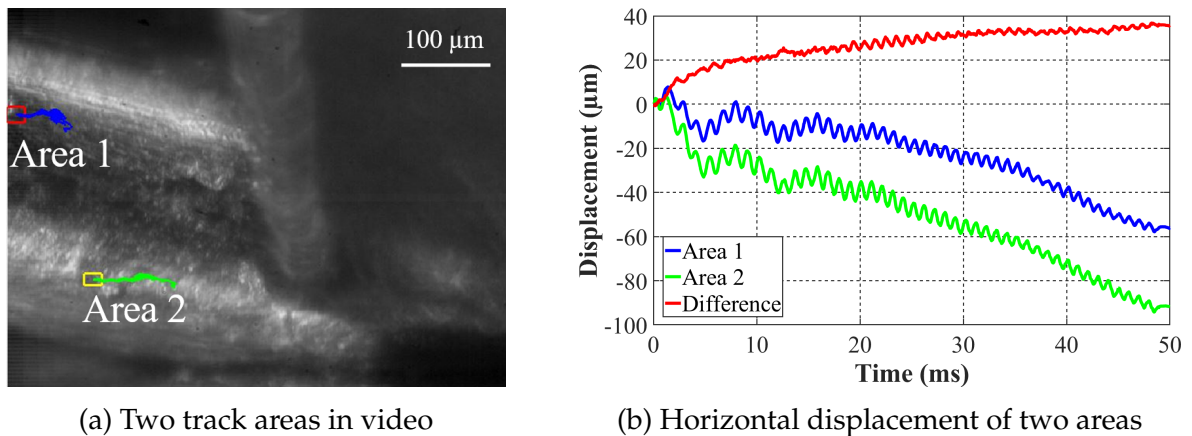


Fig. 4.12: Comparison the horizontal motion of different areas on the wire

of the tracked area on the tool insignificantly influences the tracking results. The deformation of the aluminum wire, however, significantly influences the tracking results when different areas on the wire are selected. An example is given in Fig. 4.12 where the bonding process is the same as that in Fig. 4.11. Two different tracking areas on the wire were selected: one upper square (red) and one lower square (yellow). The results show that the vibration amplitudes of the two areas were similar. A large difference, however, existed in the plastic deformation induced motion. During the bonding process, the wire (the part outside of the contact with the tool) was up-bended. This deflection led to different horizontal positions of the upper areas and the corresponding lower areas (initially on the same vertical line). To avoid this issue, only the area on the lower part of the wire was tracked for all the processes.

Since only one frame was recorded per two US vibration cycles, the real-time measurements were under sampled. Despite of this, the tracked vibration amplitudes of the tool and the wire are quite close to the results of laser vibrometer measurements of the tool movement and the oversampling measurement of the wire movement in Fig. 4.8, respectively. Therefore, the tracking results of the high-speed videos accurately described the vibration amplitudes of the tool and the wire.

4.4 Impacts of process parameters

As stated in Chapter 2, three parameters which significantly influence the bonding process can be controlled during operation. These are normal force, US power and process time. The variations of normal force and US power are shown as the square points in Fig. 4.13. The normal force can be accurately controlled as the designed values. Since the vibration was only controlled by phase-feedback, the applied US power was not exactly the same as the designed values. In this work, a power that is within the range of ± 2.0 W was considered as the designed value. In order to study the contact behavior at very low excitation levels, an additional low level of US power (~ 6 W) was also tested, shown

as the round points in the figure. Regarding the process time, since the measurement approach used in this work is real-time observation, it is possible to study the relative motions at any time within the process time range. In other words, the effect of any time length on the relative motions can be analyzed as long as the time length is less than the set value of the process time. In this work, the process time for all the processes was set to 50 ms, which is long enough for the main changes of the relative motions to take place.

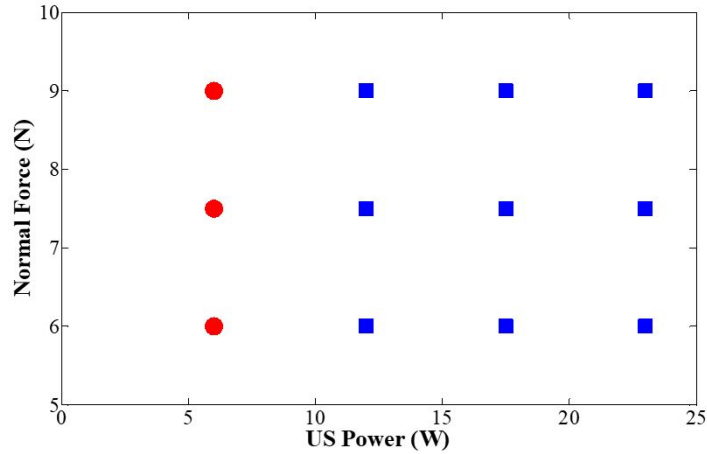


Fig. 4.13: Experimental settings of the process parameters

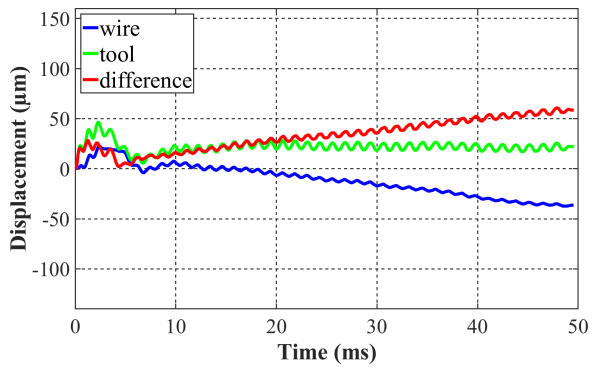
The motion tracks of the bonding process corresponding to the central square point in Fig. 4.13 were shown in last section. The motion tracks of the processes corresponding to the other eight square points are shown in Fig. 4.14. From the green curves, which show the traces of the tool, it can be seen that the shift of the equilibrium position of the tool always occurred, especially in the beginning stage until around 10 ms. However, in most cases the change in the equilibrium position of the tool in the beginning stage did not cause large relative motion as the tool and the wire were well coupled. After this shifting stage, the vibration amplitude of the tool became constant. The vibration amplitudes of the tool at around 40 ms are shown in Table 4.2. Under the same US power, a larger normal force led to a smaller vibration amplitude due to the increased friction resistance. For the same normal force, the increase of US power increased the amplitude since the driving current was larger.

Table 4.2: Vibration amplitudes of the tool at 40 ms under different settings

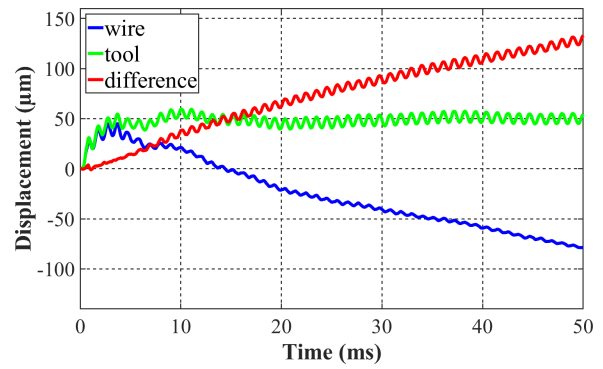
Normal Force	US Power	12 W	17.5 W	23 W
	6.0 N		3.60 μm	5.30 μm
7.5 N		3.38 μm	4.91 μm	5.27 μm
9.0 N		3.44 μm	4.59 μm	5.08 μm

The normal force and the US power interdependently influence the deformation induced relative displacement. The impacts of the normal force and the US power on the deformation induced relative displacement at both interfaces are summarized as the follows:

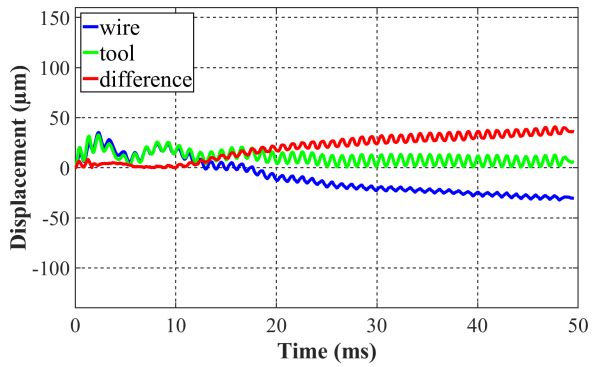
1. In general, under the same normal force, an increase in the US power enlarged the



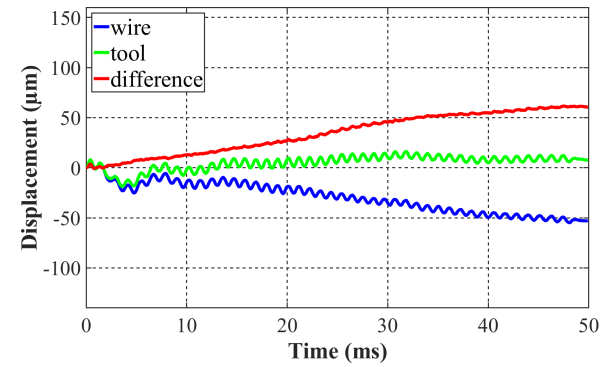
(a) 6 N, 12 W



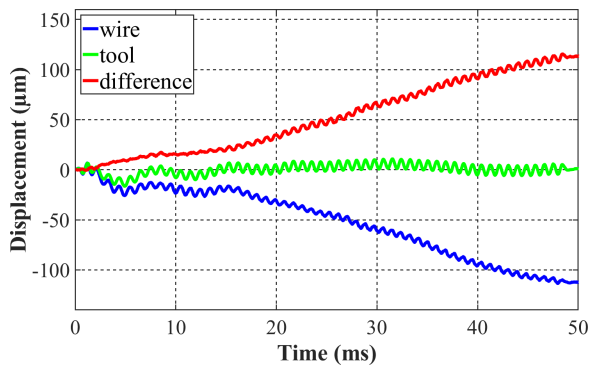
(b) 6 N, 17.5 W



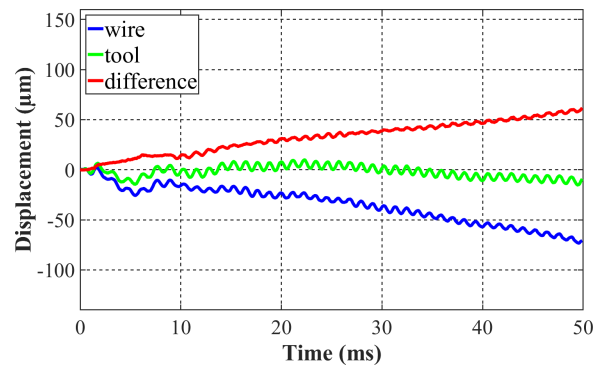
(c) 6 N, 23 W



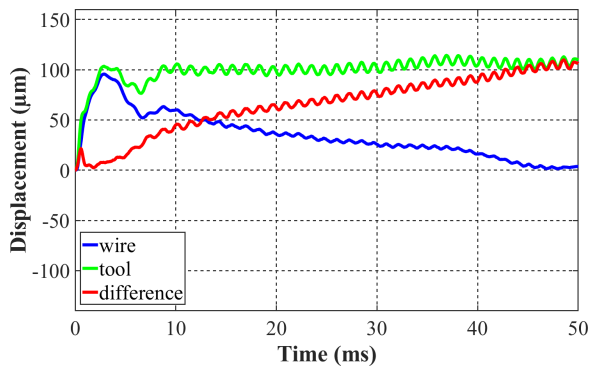
(d) 7.5 N, 12 W



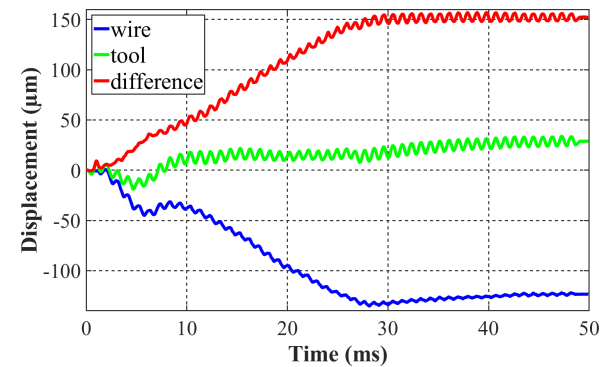
(e) 7.5 N, 23 W



(f) 9 N, 12 W



(g) 9 N, 17.5 W



(h) 9 N, 23 W

Fig. 4.14: Motion tracks of the wire and the tool under different parameter settings

deformation induced relative motion, but a minimum force of 7.5 N was required for this to take place. For example, for the three 9 N processes, the deformation induced relative motion under 23 W was much greater than that under 17.5 W, and both were much greater than that under 12 W. When the normal force was smaller than 7.5 N, like the 6 N processes, the deformation induced relative displacement significantly decreased when the US power reached 23 W. This is due to the small normal force which could not transfer enough US energy to the wire.

2. When the US power remained the same, an increase of the normal force increased the deformation induced relative displacement only when the US power was set to a high level, i.e. 23 W in the current experimental condition. When the US power was smaller, the deformation induced relative displacement underwent no significant change. Taking the three 17.5 W bonding processes as an example, the plastic deformation induced relative motions were nearly the same.
3. Under larger normal forces, more energy was transferred to the wire and the final footprint area was larger (see **Table 4.3**). This is due to the larger initial plastic deformation during the pre-deformation stage.
4. A medium plastic deformation is usually preferred as a small deformation decreases the contact area for microwelds growth and a large deformation is adverse to the oxide removal and the bond reliability. Therefore, from the deformation point of view, a combination of 7.5 N and 17.5 W as well as the combinations in **Fig. 4.14** (e)(f)(g) are favorable.

Regarding the vibration induced relative motion, the interdependent influence of the normal force and the US power also existed. The impacts of the process parameters are discussed as:

1. For the vibration induced relative displacement at the wire/substrate interface (i.e. the vibration displacement of the wire), a decreasing trend of the displacement amplitude was shown in the blue curves for all processes. This is due to the formation of microwelds which constrained the motion of the wire.
2. The middle level of the normal force led to the largest vibration amplitude of the wire. When the normal force increased or decreased, the wire became less active. A small normal force could not transfer enough energy to the wire for vibration while a large normal force prevented the motion of the wire. A large vibration amplitude of the wire is beneficial for the oxide removal.
3. Compared to the normal force, the effect of US power on the motion of the wire is less significant. Under the same normal force, a higher US power led to an early decrease of the vibration amplitude of the wire.
4. The relative motion at the wire/tool interface became more substantial as the process went forward. In most of the difference curves in **Fig. 4.14**, an increase in the vibration induced relative displacement amplitude can be seen. It is assumed to be

caused by the microwelds formed at the wire/substrate interface. As the vibration of the wire was constrained, the relative displacement amplitude between the wire and the tool increased.

5. If the relative displacement at the wire/tool interface started to increase at a middle stage, the oxides could be better removed. For example, in the case of 7.5 N, 17.5 W, the incremental trend appeared after 20 ms, which was sufficient for the removal of most oxides. When the incremental trend took place at a very early stage, like in (b) and (h), many oxides remained and would inhibit the microwelds formation in the following bonding process. This usually happens when a large US power is combined with a small normal force. In such cases, a large relative displacement amplitude in the latter stage was usually present for a long period. It could lead to the damage of pre-formed microwelds and inhibit the further formation of new microwelds. Specifically for (g) where a large shift of the equilibrium position of the tool existed, the large motion of the wire during the beginning stage could greatly facilitate the oxide removal. In conclusion, the appearance of an incremental trend of the vibration induced relative displacement amplitude at the wire/tool interface at a middle stage is beneficial for the bonding quality.

Table 4.3: Shear strength (SS) and interface area (IA) of the bonds under different parameter settings

		US Power		
		12 W	17.5 W	23 W
6.0 N	SS (N)	13.68 ± 1.23	15.25 ± 1.00	14.90 ± 2.11
	IA (μm^2)	290565 ± 49623	306647 ± 27181	291341 ± 49624
7.5 N	SS (N)	15.63 ± 2.14	19.73 ± 2.61	17.99 ± 1.64
	IA (μm^2)	320268 ± 46155	336276 ± 23794	357661 ± 22169
9.0 N	SS (N)	18.79 ± 0.60	18.98 ± 2.88	17.11 ± 2.37
	IA (μm^2)	362209 ± 24681	380054 ± 32800	420418 ± 28509

The shear strength and the interface area of the bonds were measured by shear tests and an optic microscope, respectively. The average values and the standard errors are shown in **Table 4.3**. The 7.5 N, 17.5 W specimens which possessed the smooth incremental trend on the difference curve and a medium plastic deformation had the largest mean shear force. With the increase of the normal force or the US power, the contact interface area greatly increased. The shear force, however, did not necessarily increase. Finally, the 9 N, 12 W and 9 N, 17.5 W specimens obtained a similar level of shear force as the 7.5 N, 17.5 W specimens. If a smaller deformation is preferred, 7.5 N, 17.5 W is the optimal setting.

The US power was further reduced to a value of only 6 W in order to verify if the relative motion between the wire and the tool could be eliminated. Three different normal forces were applied and tested. **Fig. 4.15** shows the motion tracks for the three 6 W processes. It can be seen that such a low level of US power did not significantly decrease the plastic deformation induced relative displacement. The decrease in the vibration induced rela-

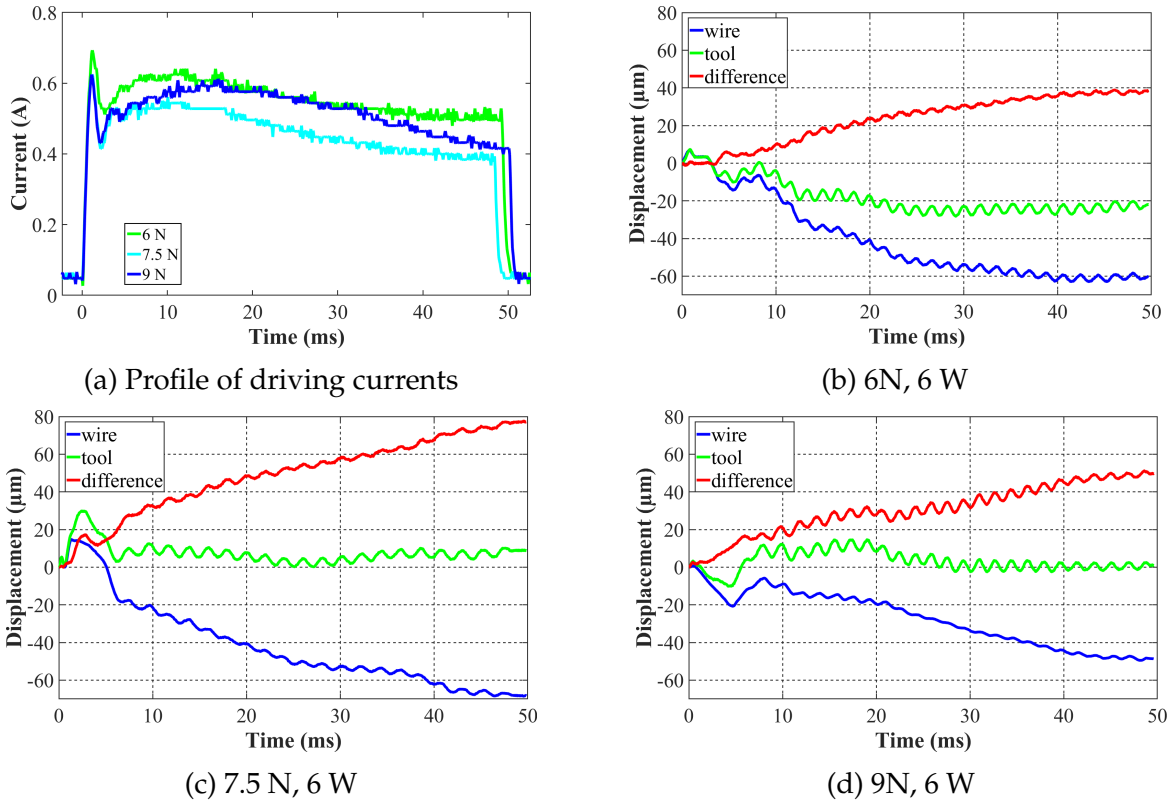


Fig. 4.15: Driving currents and motion tracks for 6 W processes

tive displacement amplitudes at the two interfaces was mainly caused by the decreased vibration amplitude of the tool. In addition, with the increase in the normal force, the vibration amplitude of the wire became smaller while the sliding at the wire/tool interface increased. As a result, the relative motion at the wire/tool interface was not eliminated by reducing the US power.

4.5 Micro-slip at the wire/tool interface

The relative motion behavior at the wire/tool interface is assumed to be similar to that between the wire and the substrate. As described in Chapter 2, it is assumed that the relative motion at the wire/substrate interface can be described by a combination of the Mindlin model and the stick-slip model. Unfortunately, the Mindlin model only considers the interface between two elastic bodies while the wire bonding domain contains two interfaces. By taking the Mindlin model (micro-slip) into consideration of the relative motion behavior at the wire/tool interface, the amplitudes of relative motion at different locations of the interface are different.

This assumption can be verified by two approaches: the change of the wire surface topography and the wear of the oxide layer. Due to the tiny thickness ($\sim 5 \mu\text{m}$) and re-oxidation, the second approach is hard to operate. To overcome these difficulties, an artificial oxide layer was coated on the wire. The wear of the coated layer was checked by the change of

the distributions of the coated elements. In this work, two different kinds of oxides, amorphous aluminum oxide (Al_2O_3) and Zirconium oxide (ZrO_2), were coated on the wire. The changes of the surface topography and the elements distributions were recorded by a scanning electron microscope (SEM). All the SEM images in this dissertation were taken at the Institute of Micro-Production Technology, Leibniz Universitaet Hannover. The details of the coating process as well as its influence on the bonding process will be provided in Chapter 5.

4.5.1 Change of wire surface topography

The change of the upper surface topography of the wire during the bonding process was first analyzed. In order to observe the change, specimens under the same normal force and US power but with different process times of 10 ms, 20 ms, 30 ms, 40 ms and 50 ms were prepared.

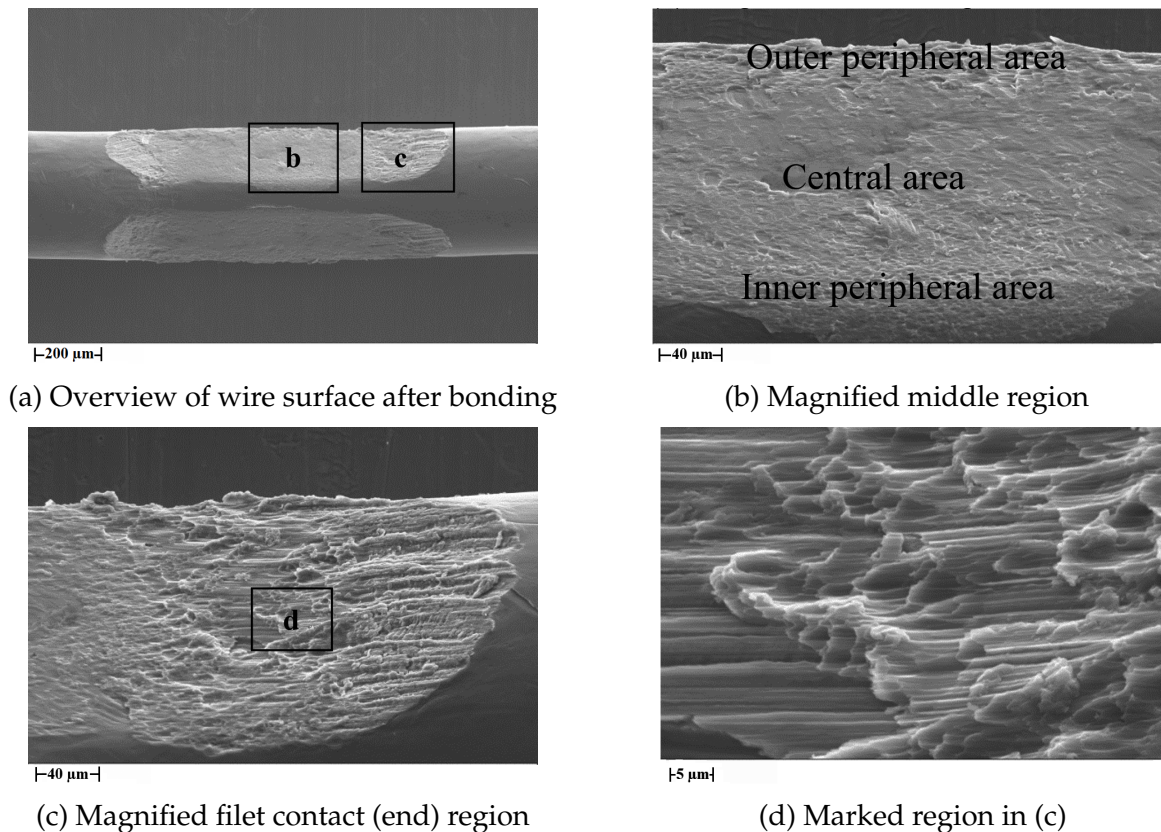


Fig. 4.16: Upper surface topography of the wire after 50 ms under 9 N, 23 W

To get an impression on the significant change of the surface topography from the original smooth surface, detailed information on the 50 ms specimen is first provided in Fig. 4.16. (a) is the overview of the surface topography. (b) and (c) are the magnified images of the middle and end contact regions in (a), respectively. The same selection of these two areas was also performed in the following four figures. As shown in (b), the outer and inner peripheral areas are much rougher than the central area, which indicates that the friction

in the peripheral areas was more serious. (d) is a magnified image of a local end region. A very serious worn and directional surface can be observed. The gradual changes from 10 ms to 40 ms are shown from Fig. 4.17 to Fig. 4.20.

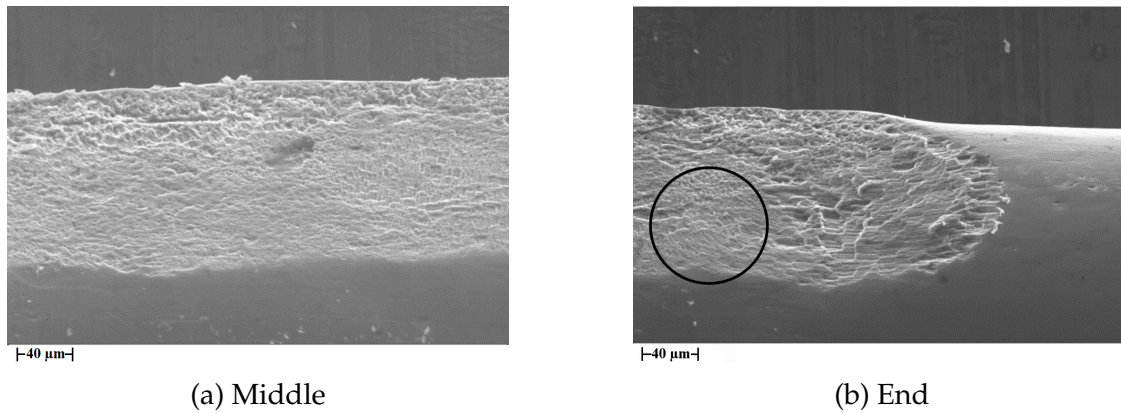


Fig. 4.17: Upper surface topography of the wire after 10 ms under 9 N, 21 W

After 10 ms, the middle and end regions of the wire surface are shown in Fig. 4.17 (a) and (b), respectively. In the middle contact region, the outer peripheral area has more substantial wear while a smoother surface can be seen in the central area and the inner peripheral area. As for the end contact region, the area in contact with the tool fillet shows a rougher surface compared to the area on the left side of the figure. In addition, the surface structure in (a) exhibits a direction that is approximately perpendicular to the wire direction. The fillet contact area in (b), has a directional structure that is consistent with the wire direction. A transitional direction is observed in the area as marked in (b). Since all the directions seen in the upper surface are consistent with the continuous plastic deformation induced expansion of the wire, in the first 10 ms, the plastic deformation played a more important role on the topography change than the vibration induced relative motion.

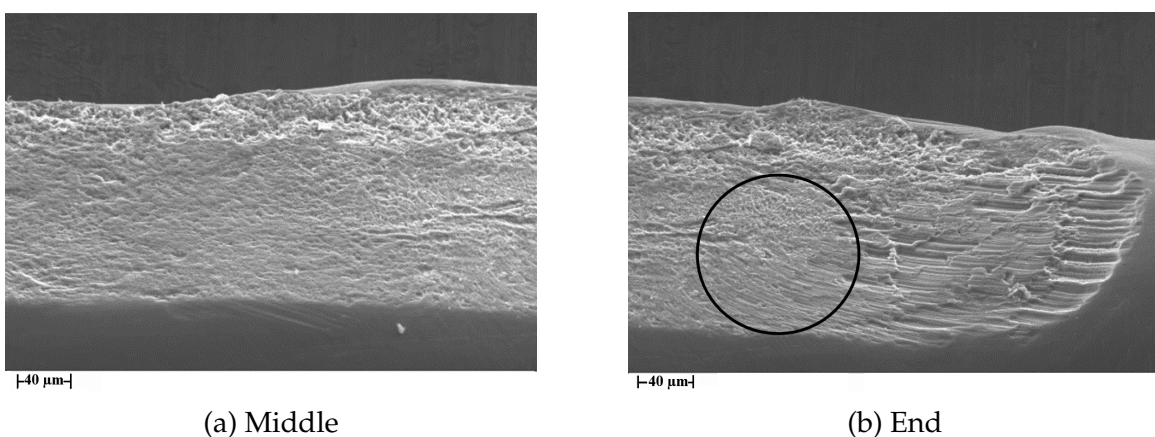


Fig. 4.18: Upper surface topography of the wire after 20 ms under 9 N, 18 W

After 20 ms process time, no big change of the topography can be found in Fig. 4.18 except the expansion of the contact area. Similar to the 10 ms specimen, the outer peripheral area in (a) and the fillet contact area in (b) received more wear than the other areas. The area as marked in (b) still exhibits a direction of material flow caused by the plastic deformation

of the wire. Therefore, the plastic deformation in this period is still significant on the topography change.

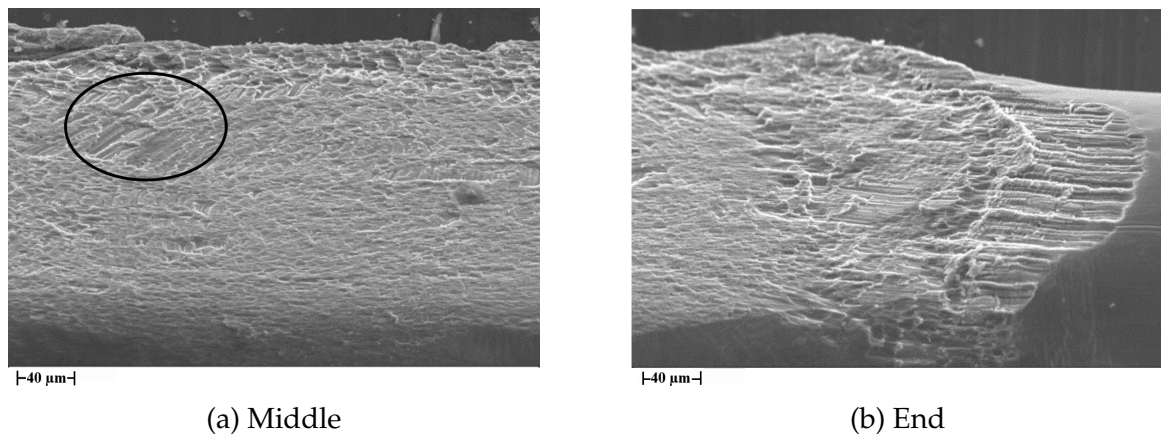


Fig. 4.19: Upper surface topography of the wire after 30 ms under 9 N, 23 W

The distribution of the wear for the 30 ms specimen shown in **Fig. 4.19** is similar to the last two specimens. The outer peripheral area in (a) and the fillet contact area in (b) show more substantial wear. A directional structure which is consistent with the vibration direction appeared in the outer peripheral area of (a). Even though a directional area corresponding to the material flow can be observed, as marked in (a), the main area reflects the direction of vibration. As a result, the vibration induced relative motion becomes more significant on the topography change during the process time window between 20 ms and 30 ms.

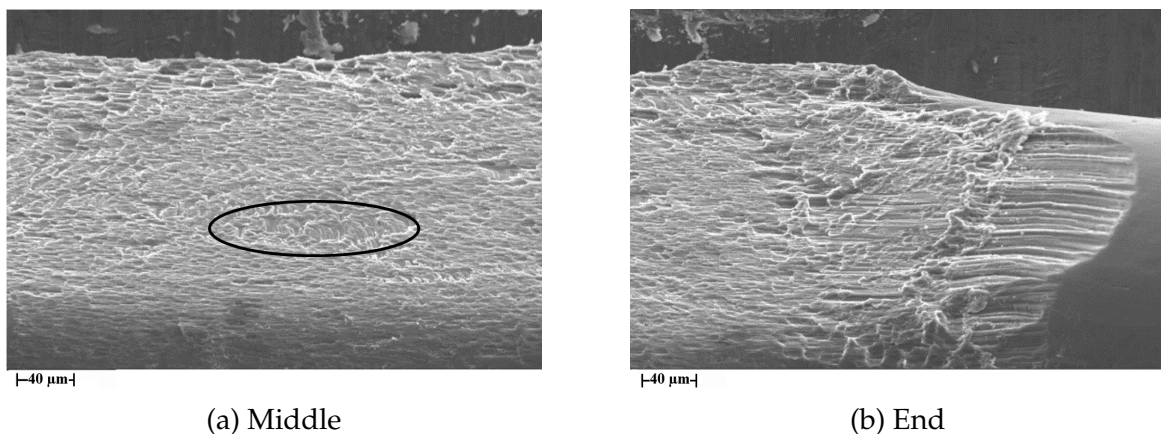


Fig. 4.20: Upper surface topography of the wire after 40 ms under 9 N, 24 W

As before, for the 40 ms specimen shown in **Fig. 4.20**, the wear in the outer peripheral area of (a) and the fillet contact area of (b) is more substantial than that observed in the other areas. However, nearly the whole surface shows a texture which corresponds to the vibration direction. It means that the vibration induced relative motion dominated the topography change in the latter stage of the process. Specifically, the central area marked in (a) still shows a direction perpendicular to the vibration direction. This indicates that this area was less influenced by the vibration induced relative motion. In addition, this area afforded to the largest normal stress. Therefore, the vibration induced relative dis-

placement amplitude in this area is small or even close to zero.

Based on the analysis of the five specimens under 9 N, 22 W, the following conclusions can be reached: the wear in the fillet contact areas is larger than the wear in the outer peripheral areas and the wear in the inner peripheral areas is larger than the wear in the central areas; the continuous plastic deformation is more significant on the topography change than the vibration induced relative motion in the first 20 ms; the vibration induced relative motion becomes more important on the topography change in the rest of the process time. Reflected by the wear conditions and the directional structure, it can be deduced that the relative motion amplitudes at different locations of the wire/tool interface are different.

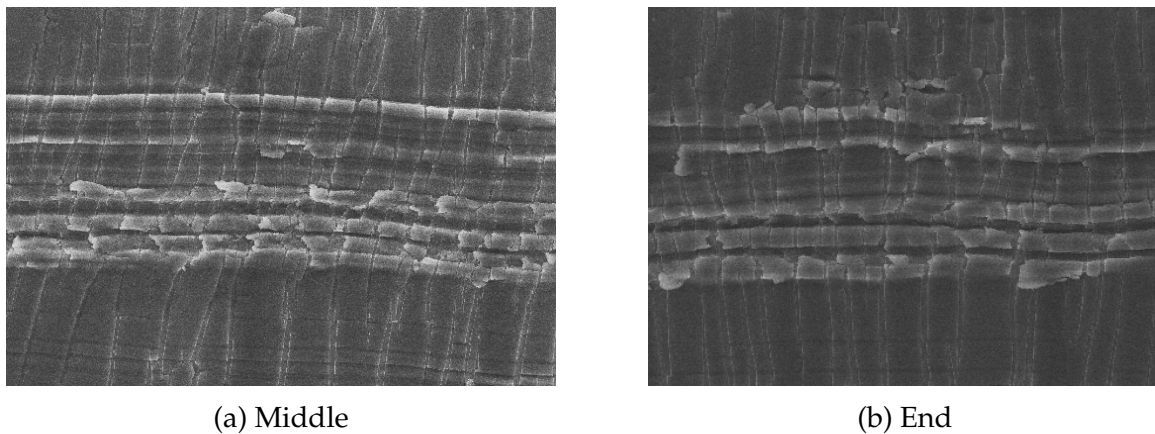


Fig. 4.21: Cracks on the Al_2O_3 coated wire

The topography change on coated wire is similar to the above results with uncoated wire. The only difference is the observable cracks on the coated Al_2O_3 layer. As shown in Fig. 4.21, the direction of the cracks is perpendicular to the wire direction. The cracks also indicate the strain gradient at the wire/tool interface, which is similar to that at the wire/substrate interface as shown in Section 5.3. This supports the hypothesis that the relative motion conditions at the wire/tool interface are similar to those at the wire/substrate interface.

4.5.2 EDAX analysis of wear

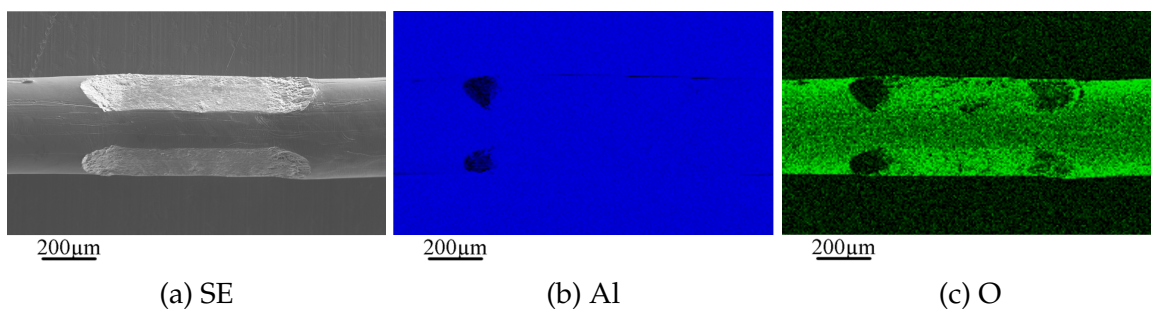


Fig. 4.22: EDAX mapping of Al_2O_3 coated wire after 30 ms under 9 N, 22 W

In addition to the analysis of the topographies, the wear of the coated oxide layer was further analyzed by Energy dispersive X-ray spectroscopy (EDAX). The EDAX analysis was first conducted on a 200 nm Al_2O_3 coated wire. The EDAX mapping results after 30 ms process time are shown in **Fig. 4.22**. The second electron (SE) image of (a) gives an overview of the surface topography. (b) shows the distribution of aluminum element corresponding to (a). Since both the wire and the coated oxide contain aluminum, the element Al was found in the whole image. The two dark areas in (b) shall be ignored since the detector was placed on the left side and could not receive the electrons from these areas. The oxygen distribution in (c) clearly shows that most of the coated oxide in the filet contact areas was removed within the first 30 ms. This also indicates that the wear in the end regions is more substantial than that in the other regions.

More oxides were removed in the last 20 ms, as shown on the 50 ms specimen in **Fig. 4.23**. The Quad-backscattered diffraction (QBSD) image of (a) provides an overview of the wire surface. There is virtually no change in the distribution of aluminum as in (b) but a significant change in the distribution of oxygen as in (c). Compared to **Fig. 4.22** (c), only the central areas, marked in the red ellipses, still conserved some oxide while most oxides in the peripheral areas were removed during the last 20 ms. Furthermore, a high concentration of oxygen can be found in the white circles in (c). It is mainly attributed to the fact that large amounts of oxides were carried to these areas.

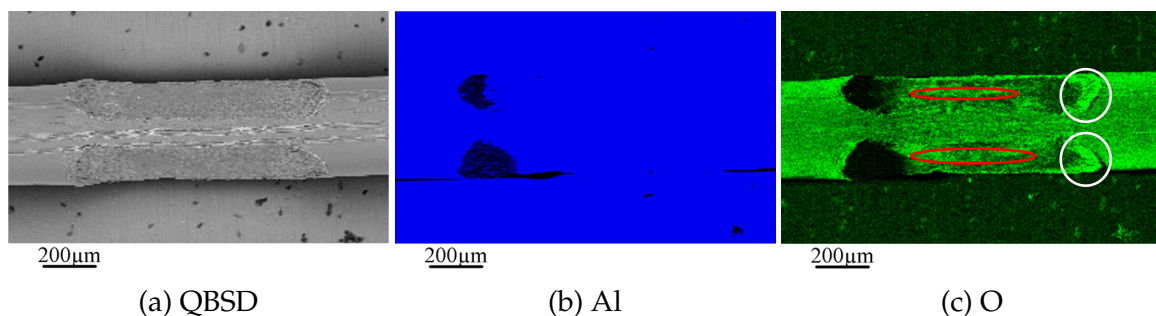


Fig. 4.23: EDAX mapping of Al_2O_3 coated wire after 50 ms under 9 N, 22 W

The EDAX analysis was then conducted on a 50 nm Al_2O_3 coated wire. Since the whole oxide layer was already removed within a short time range, the results were significantly influenced by re-oxidation when the wire surface was exposed to the air. Therefore, no information was revealed.

As the oxide becomes softer, the removal rate decreases. This could be observed when the wire was coated with a 50 nm ZrO_2 (much softer than Al_2O_3) layer. This layer at the wire/tool interface was not completely removed within 50 ms. The EDAX mapping for a 50 ms specimen is shown in **Fig. 4.24**. Some oxides remained in the area marked by the red ellipses. In addition to the filet contact areas and the outer peripheral areas, most oxides in the inner peripheral areas was also removed. As indicated by the oxygen distribution, most oxides were transported to boundary of the wire/tool contact area.

According to the EDAX results, it can be also concluded: the wear in the filet contact areas

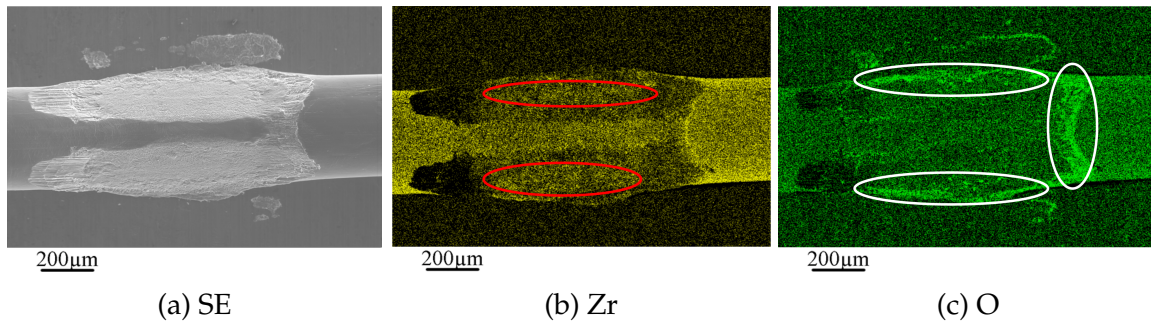


Fig. 4.24: EDAX mapping of ZrO_2 coated wire after 50 ms under 9 N, 23 W

is larger than the wear in the outer peripheral areas and the wear in the inner peripheral areas is larger than the wear in the central areas. As a result, the result of the topography change and the result of the EDAX analysis inter-validated each other. According to the simulation results in [39, 51], the normal stress in the central area is greater than that in the inner peripheral areas; the normal stress in the inner peripheral areas is greater than that in the outer peripheral areas and the filet contact areas. Therefore, it can be stated: the relative displacement amplitude in the filet contact areas is larger than the relative displacement amplitude in the outer peripheral areas and the relative displacement amplitude in the inner peripheral areas is larger than the relative displacement amplitude in the central areas.

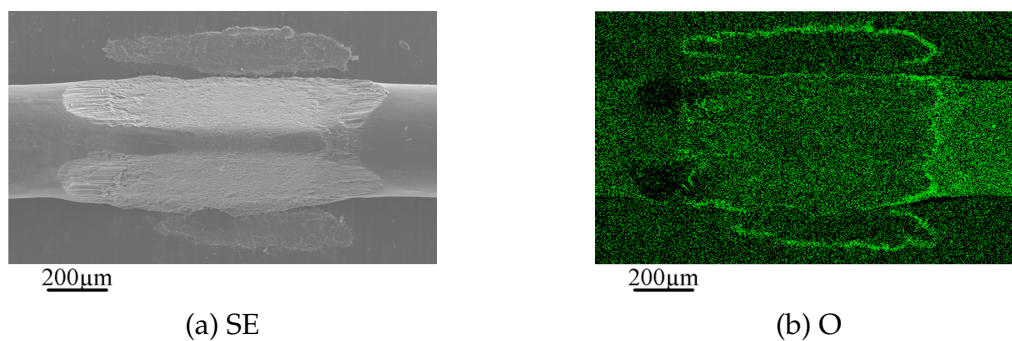


Fig. 4.25: EDAX mapping of the oxygen distribution in the tool touched areas

An interesting phenomenon which was discovered during the tests is the natural oxide removal in the tool/substrate contact areas. When a high US power and a larger normal force were applied or the process time was long enough, the wire was over-deformed and its z-dimension was greatly reduced. In this case, the feet of the bonding tool came into contact with the substrate in the latter stage of the process. An example of the footprints of the tool feet is given in **Fig. 4.25** (a). The oxygen distribution is shown in (b). A high intensity of oxygen can be found at the boundaries of the tool feet contact area. This indicates that large amounts of oxides were transported to the boundary within a short period, even with the flat surfaces of the tool feet.

4.5.3 Accumulations of aluminum on the bonding tool

Due to the wear on the wires during the bonding processes, some aluminum accumulates at the tool tip. In this work, the bonding tool was checked after ~ 100 bonding cycles with the Al_2O_3 coated wire. Compared to the new tool in Fig. 4.26 (a), a black band was found on the used tool in Fig. 4.26 (b). This band corresponds to the wire/tool contact boundary. Close-up images on the same location within the band region of the new and used tools were taken and are shown in (c) and (d), respectively. Compared to the new tool in (c), a clear accumulation of external materials can be observed on the used tool in (d).

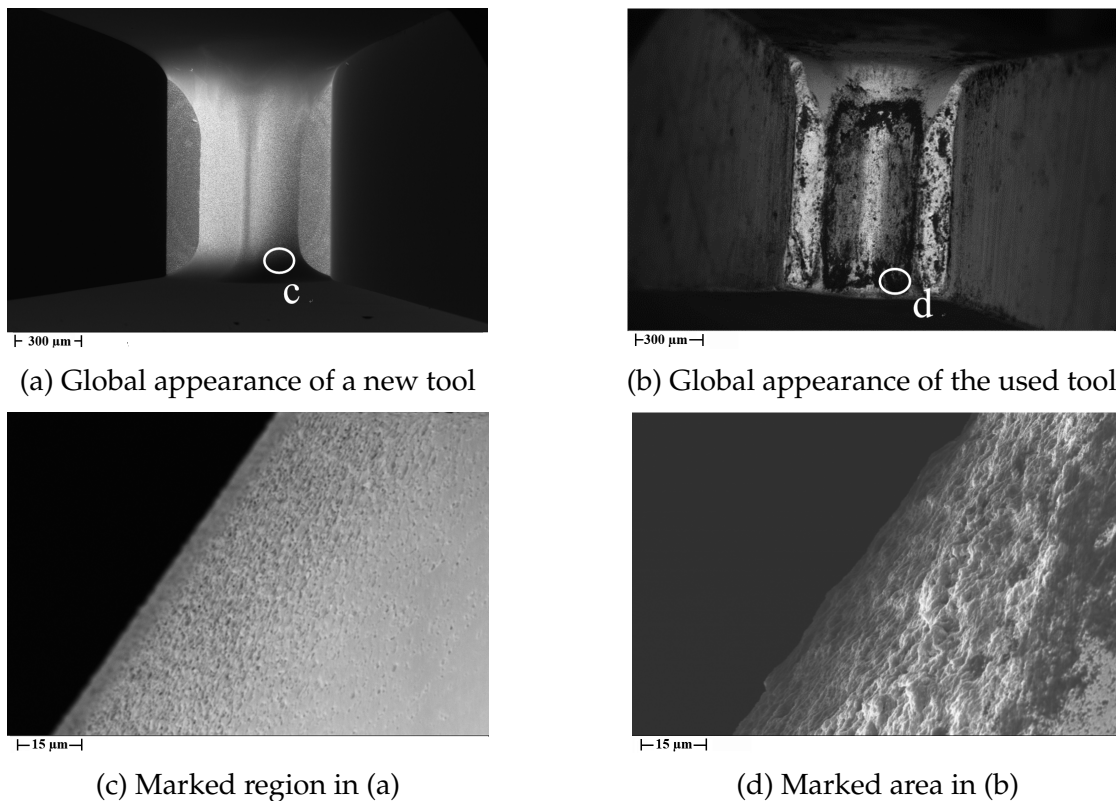


Fig. 4.26: Global and local comparison of new and used tools

An EDAX mapping was performed on one side of the used tool to analyze the composition of the accumulated material. Since the oxide coating is Al_2O_3 and the tool is made of Tungsten carbide (WC), the elements of W, Al and O were checked. As shown in Fig. 4.27, a high concentration of the elements of Al and O is exhibited in the band region while the element Tungsten (W) lost its intensity in the same region. To summarize, the material accumulation on the tool tip further validates the previous result that the relative displacement amplitude in the outer peripheral and fillet contact areas is larger than that in the inner areas.

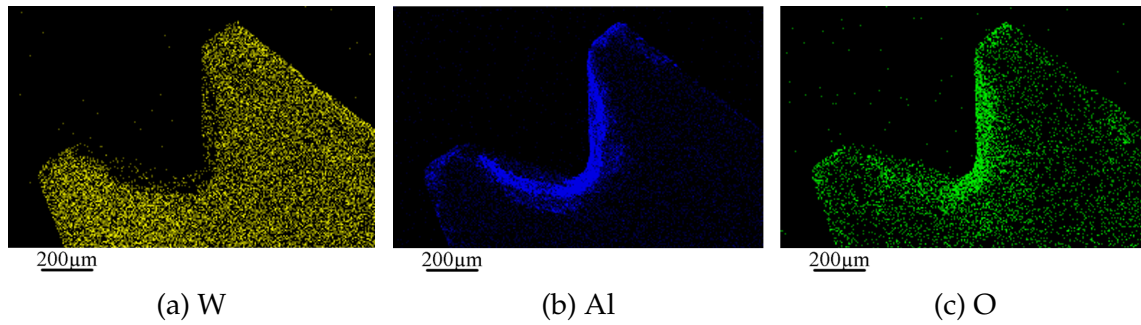


Fig. 4.27: EDAX mapping of the old tool

4.6 Conclusion

In this chapter, the relative motion behaviors at the wire/substrate interface and the wire/tool interface were investigated and quantified based on the real-time observation of the bonding process. Both the deformation induced relative motion and the vibration induced relative motion at the two interfaces were captured in all processes. In addition, a change in the equilibrium position of the tool always occurred, especially in the beginning stage. The process parameters including the normal force, the US power and the process time significantly influence the relative displacement amplitude. In general, the plastic deformation continues as the process goes on, unless a limit value is reached. The vibration induced relative displacement amplitude at the wire/substrate interface decreases in the latter stage since more microwelds are formed to constrain the motion of the wire. In the mean time, the vibration induced relative displacement amplitude at the wire/tool interface increases. The normal force and the US power interdependently affect the two components of the relative motion. In most cases, a greater force or power results into a larger deformation induced relative displacement; this, however, depends on the initial plastic deformation during the pre-deformation stage. A suitable combination of the two factors leads to a larger vibration induced relative displacement amplitude at the wire/substrate interface. A gradual increment of the vibration induced relative displacement at the wire/tool interface indicates a good bonding quality. The result of topography change and the result of EDAX analysis supported the hypothesis that the relative motion behavior at the wire/tool interface follows the Mindlin model. This means that the relative displacement amplitudes at difference locations of the interface differ from one another: the relative displacement amplitude in the filet contact areas is larger than the relative displacement amplitude in the outer peripheral areas and the relative displacement amplitude in the inner peripheral areas is larger than the relative displacement amplitude in the central areas.

5 Experimental investigations on oxide removal

As oxides inhibit the formation of microwelds, their removal is essential for the bonding process. Due to the enclosed interface and the ultra-small thickness of the natural aluminum oxide layer, knowledge of the oxide removal process is still quite limited. In this chapter, the oxide removal is first analyzed via real-time observations of the metal-glass bonding interface. The changes in five different areas including contact area, friction area, stick area, oxides area and microwelds area are revealed. The oxide removal process is then further analyzed based on the change of an artificial coated oxide layer. Four steps including cracks, detachment, milling and transportation are detected. Metal penetration, oxide flow, pushing and metal splash drive the transport of the oxides. During the transport, small oxide particles agglomerate together into larger ones. Some contents of this chapter have been published in [132–136].

5.1 Experimental setup

To optically observe the oxide removal process at the wire/substrate interface, the metal substrate was substituted by a transparent glass plate. The real-time observation system in Chapter 4 was then vertically installed beneath the glass. Some of the specimens (either the wire or the substrate) were coated with an oxide layer to facilitate the detection of the oxide removal mechanisms.

5.1.1 Observation of the wire/substrate interface

The US wire bonding platform, the real-time observation system and the laser source used in this chapter are the same as those in Chapter 4. In Chapter 4, the relative motions at the two interfaces were of interest. The interfaces were thus observed from a side view. The purpose of this Chapter was to observe the oxide removal process at the wire/substrate interface. Therefore, the real-time observation system had to be perpendicular to the interface. Another issue is the visibility of the wire/substrate interface. As this interface is enclosed by the intransparent metal wire and metal substrate, it cannot be seen. To solve this problem, a transparent glass was used as the substrate, which was inspired by Maeda et al. [66]. The whole setup is shown in Fig. 5.1. The real-time observation system was

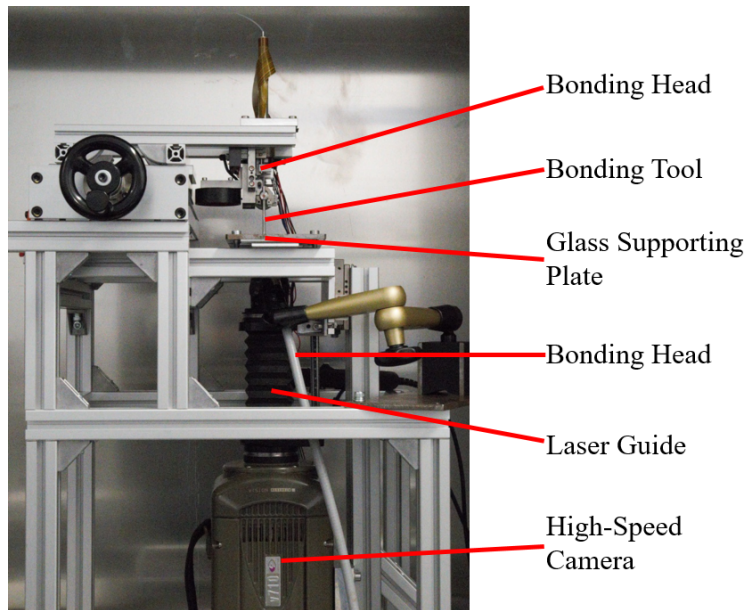


Fig. 5.1: Observation of the wire/substrate interface

vertically installed beneath the glass. The glass was purchased from Siegert Wafer GmbH. It has dimensions of $40 \times 40 \times 3$ mm with a surface roughness R_a of less than 1.2 nm. The light from the laser source was projected onto the interface and then reflected into the real-time observation system. To record the main region of the interface, a larger window size (640×480 pixel) was selected and the corresponding frame rate was set to 20000 fps. The exposure time was set to $2 \mu\text{s}$.

5.1.2 Specimen preparation

Some of the Al-H11 wires and the glass substrates were deposited with an oxide layer via physical vapor deposition. The deposition process was performed in a Kenotec RF (13.56 MHz) 6.5 " target magnetron sputter device. The wires were mounted on an aluminum frame. The frame could be turned over so that both sides of the wire could be coated. In this way, a homogeneous oxide layer on wire was achieved as inspected by SEM.

In order to study the influence of the oxide hardness on the oxide removal process, two different kinds of oxides - Al_2O_3 and ZrO_2 - were selected. The deposition parameters were set as follows:

Al_2O_3 : 500 W, 95 sccm Ar, 5 sccm O_2 , 5×10^{-3} torr, 6 nm/min;

ZrO_2 : 200 W, 95 sccm Ar, 5 sccm O_2 , 5×10^{-3} torr, 2 nm/min.

A 5-min break was taken after every 10-min deposition. A temperature inside the chamber was kept at a low level ($< 150^\circ$) and the material properties were not significantly changed. Most of the specimens were coated with a 50 nm oxide layer. Specifically for

Al_2O_3 , a 200 nm layer was coated on the wire to investigate the impact of the thickness of the oxide layer on the removal process. After deposition, the hardnesses and Young's moduli of the two materials were measured by a Hysitron TI 900 Triboindenter. The measured nano-hardnesses for Al_2O_3 and ZrO_2 were 12.07 ± 1.33 GPa and 6.25 ± 1.38 GPa, respectively. The Young's moduli for Al_2O_3 and ZrO_2 were 125.52 ± 17.71 GPa and 124.00 ± 11.73 GPa, respectively. It can be seen that the hardness of ZrO_2 is only about half of that of Al_2O_3 . As a result, the two materials are appropriate for studying the impact of the hardness on the removal process.

5.2 Oxide removal for non-coated wire

The US bonding process with non-coated wire and non-coated glass was first observed. During the bonding process, five different areas, including the contact area, friction area, stick area, microwelds area and oxides area, were detected and quantified. The cleaning coefficient, that is the ratio of the oxide-free area over the contact area, during the bonding process was analyzed. In addition, the moving of oxide particles within the contact interface was captured.

5.2.1 Real-time observation

5.2.1.1 Central contact region

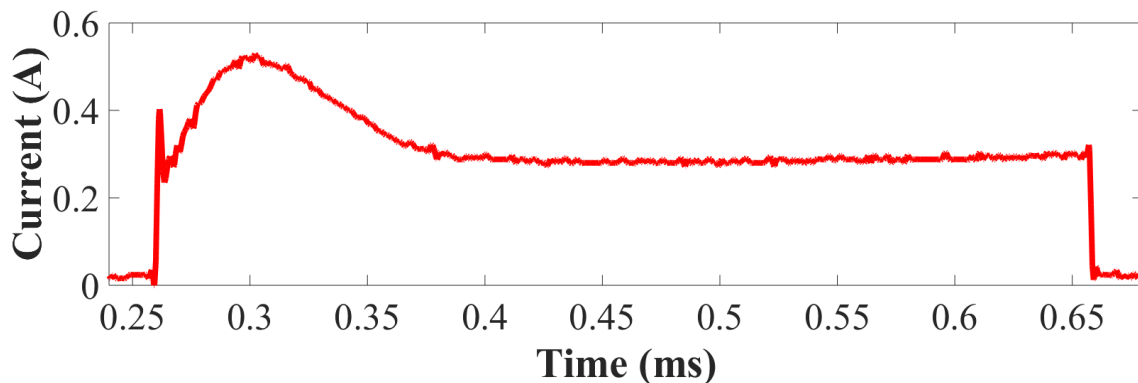


Fig. 5.2: Driving current of the transducer under 5 N and 2.4 W

US bonding processes under different normal forces and US powers were recorded. In comparison with Al-Al bonding, the applied US power for metal-glass bonding was much lower and the process time was much longer. A typical metal-glass bonding process under 5 N, 2.4 W was selected to show the findings.

The driving current of the transducer throughout the process is shown in **Fig. 5.2**. After the first over-shoot of the current (over the constant level), a second over-shoot appeared and lasted for a much longer time (~ 120 ms). This is caused by the smaller impedance at the wire/substrate interface due to the oxide particles, which will be described later. A

constant value was then reached. This feature was usually found in the metal-glass bonding processes. The driving current can be correlated with the recorded frames. According to the current curve, the US vibration lasted for 399.8 ms which corresponded to 7996 frames of the video. The number of frames in which the motion of the wire was detected, however, was only 7962. This difference resulted from the first ~ 1 ms and the last ~ 1 ms of the process. Two situations might take place during these periods. First, the relative displacement between the wire and the substrate during these periods was smaller than the resolution of the camera. The relative motion existed but was not detectable by the video. Second, according to [30], only elastic deformation of the wire occurred during the two periods. No relative motion existed.

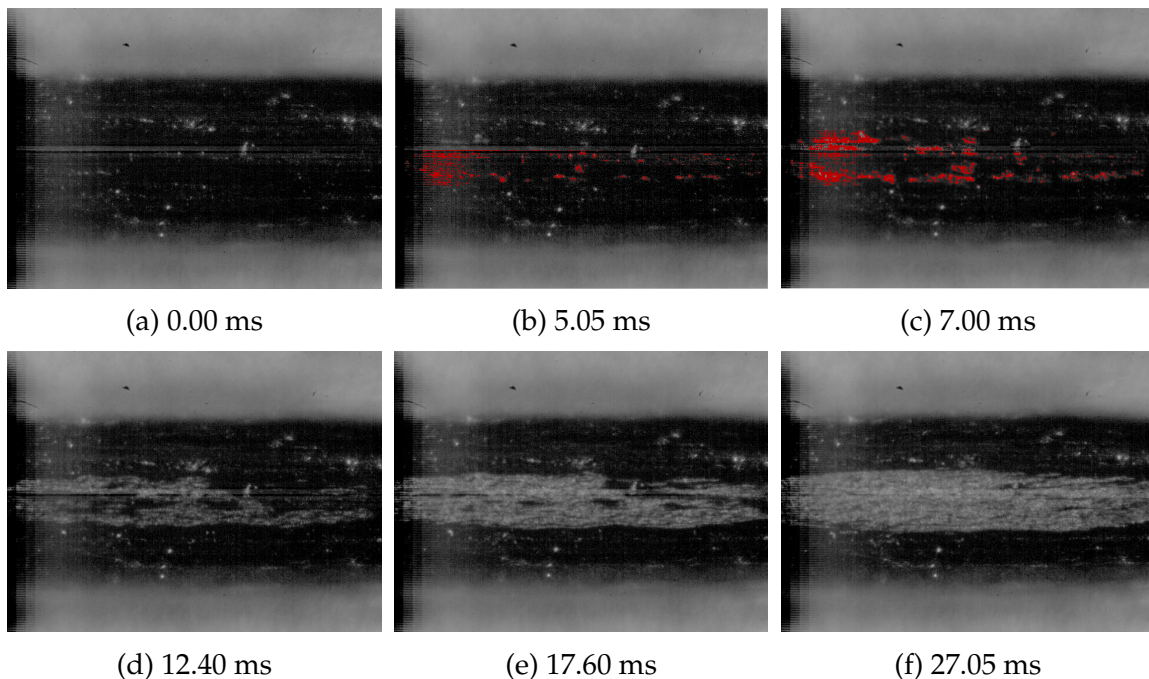


Fig. 5.3: The expansion of the contact area under 5 N, 2.4 W

The real-time observation of the process is explained as follows:

1. After a 5 N normal force loading, the wire/substrate contact was changed from a line to an elliptical area. The interface after the normal force loading is shown in **Fig. 5.3** (a). The contour of the wire is marked by the yellow rectangle. The contact area, however, is hard to observe as the whole wire surface shows a low brightness. No cracks were observed during the Pre-deformation stage.
2. The US vibration was then activated.
3. After ~ 1 ms of the US vibration, the sliding of the wire on the substrate became detectable in the video.
4. At the process time of **Fig. 5.3** (b), the brightness in some peripheral contact regions became higher (These regions in (b) are not as obvious as those in the video. To make them evident in the figure, they were marked in red.). As described in Chapter 2, the

relative displacement amplitudes at different locations of the interface are different. Since the relative displacement in the peripheral region was larger, the detachment of oxides was assumed to first take place in this region. If the detached oxides were still in the form of flakes, the high brightness regions would not appear. As with the wire surface, the surfaces of such oxide flakes could only reflect a small amount of light due to its angle to the light and the camera. Therefore, it was assumed that there was an additional step after the detachment - milling. After the detachment, the oxides were milled into particles. Since the particles have many facets with different angles to the light, they reflect more light into the camera. This assumption will be further verified in Section 5.3.

5. As the vibration continued, nearly the whole peripheral region exhibited a high brightness, as in **Fig. 5.3** (c) (as in (b), the bright peripheral region was marked in red). It indicates that all the oxide layer in the peripheral region had been detached and milled into small particles at 7.00 ms.
6. The bright area then extended to the central region, as shown in **Fig. 5.3** from (d) to (f). At the process time of (f), the whole contact area shows a high brightness. All oxides within the contact area had been milled into small particles.
In other processes where the US power was too small, e.g. 0.3 W, only the oxides in the peripheral region were milled into small particles.

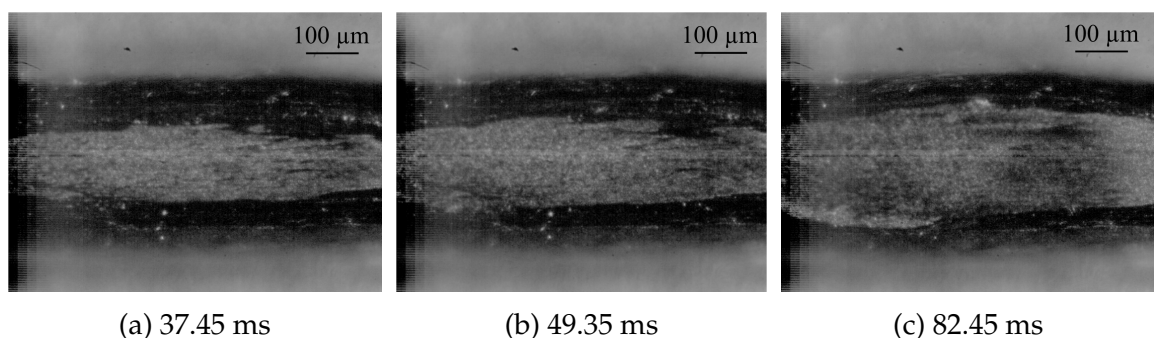


Fig. 5.4: The expansion of the contact area under 5 N, 2.4 W

7. Due to the Acoustoplastic Effect (APE), the contact area was enlarged. Simultaneously, the oxides within the expanded area were detached and milled into small particles. Three representative frames were selected to show this in **Fig. 5.4**. From (a) to (c), the bright area distinctly expanded. According to [83,137], the acoustic softening became active when the vibration amplitude of the tool exceeded a critical value. The defects inside crystals, especially the dislocations, were then activated from their pinned positions. The yield stress was thus greatly reduced. In addition, the superimposed oscillating stress from the vibration caused a further reduction in the yield stress. As a result, even though the normal force was kept constant, continuous plastic deformation and the expansion of the contact area took place.
8. The relative displacement amplitude in the central region became increasingly small until it began flashing. The occurrence of blinking means that no obvious relative

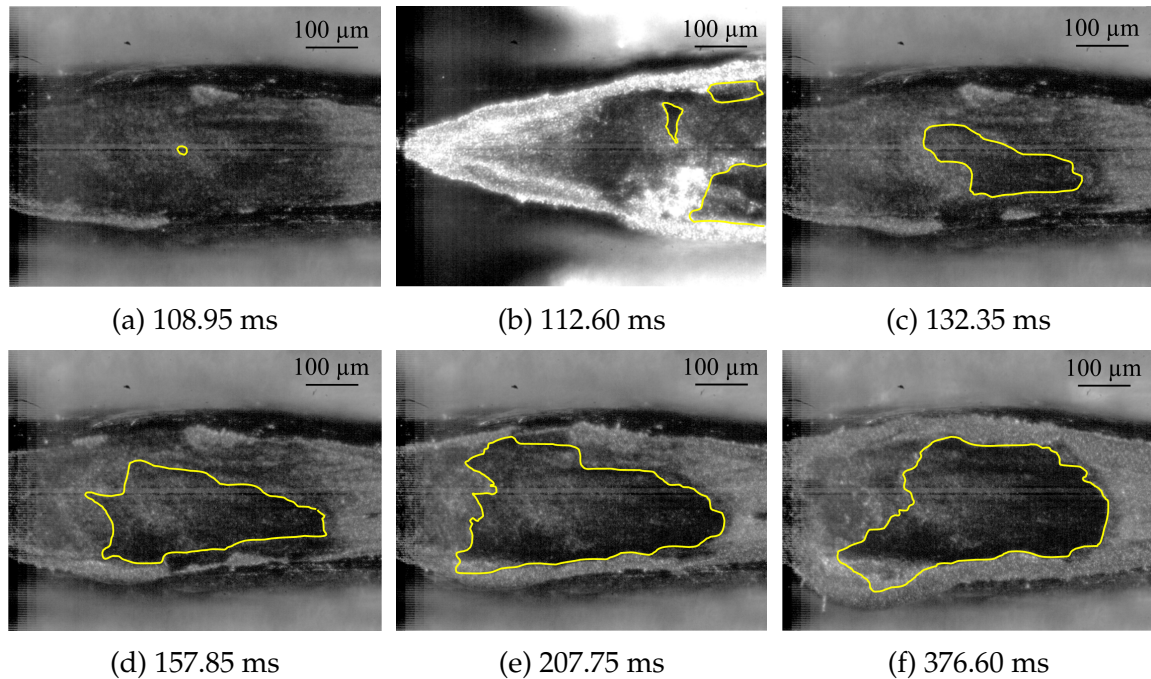


Fig. 5.5: The appearance and expansion of the stick area under 5 N, 2.4 W

displacement was observed in the video while the reflected light flashed. This was due to the resolution of the real-time observation system ($1.1 \mu\text{m}/\text{pixel}$). When the relative displacement amplitude became less than $0.55 \mu\text{m}$, the relative motion was not detectable. The tiny motion or rotation of the oxide particles caused the flashing of the light.

9. At ~ 108 ms, a dark and stick area emerged in the central contact region. This stick area at 108.95 ms is shown **Fig. 5.5** (a) and marked by a yellow curve. The emergence of the stick area was caused by the formation of microwelds. It seems that microwelds first formed in the central region and the motion of the central part of the wire was constrained by them. As a result, the central part of the wire became static in the video.
10. After the emergence of the stick area, the area surrounding the stick area ceased vibrating visibly and began to blink.
11. The stick area expanded. The expansion can be clearly observed in **Fig. 5.5** from (a) to (e). More microwelds formed and further constrained the motion of the wire.
12. During the expansion of the stick area, oxides moved towards the peripheral region. Vibration was assumed to play a significant role on the moving of these oxides, as there was no obvious material flow in the stick area. Not all oxides within the stick area were removed. Some oxides remained and showed a high brightness. In these areas, nearly no microwelds were formed, as most of the substrate surface was covered by the oxides.
13. After ~ 208 ms, the expansion of the stick area to the upper-right region continued

while the stick area in the upper-left region shrank. This can be seen in the comparison between Fig. 5.5 (e) and (f). The upper-left region reverted from the static state back to friction. This implies that excessive vibration could break the existing microwelds. Since the expansion area and the shrinkage area were similar in size, the stick area in the last ~ 200 ms experienced no significant change.

14. As shown in Fig. 5.5 (f), the peripheral region has a higher brightness than the central region. This indicates that most oxides had been transported from the central region to the peripheral region. The oxides in the red ellipses also show that some oxide particles were transported to the outside of the contact.

Similar changes in these areas were also found in the other processes under different parameter settings.

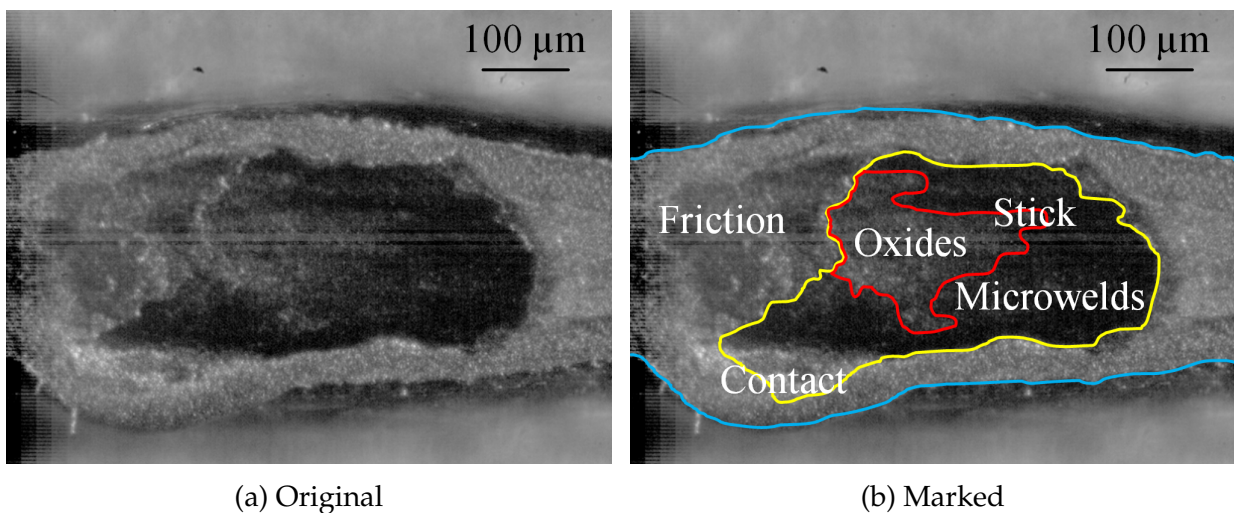


Fig. 5.6: Illustration of five different areas at the wire/substrate interface

To summarize, five different areas including the contact area, friction area, stick area, microwelds area and oxides area emerge and change at the wire/substrate interface during the metal-glass bonding process. The final distribution of these areas is shown in Fig. 5.6. (a) is the final frame of the video and (b) shows the marked areas. The contact area (enclosed by the blue borders) forms after the loading of the touch-down force while the friction area (between the blue and yellow borders) appears after the vibration is activated. Due to the detachment and milling of oxides, the friction area exhibits a high brightness. The stick area (enclosed by the yellow borders) emerges when microwelds (the area between the yellow and red borders) constrain the motion of a part of the wire. During the expansion of the stick area, some oxides (enclosed by the red borders) remain and microwelds form in the rest of the stick area. It shall be noted here that in this work, the oxides area only refers to the area that is within the stick area and covered by oxides.

5.2.1.2 End contact region

The window size (640 × 480 pixel) selected in this work is not large enough to capture the whole contact area. In last section, the bonding process in the middle region was

described. To get a complete picture of the bonding process over the whole contact area, the bonding process in an end region is explained in this section.

The changes of the contact and friction areas in the beginning stage are similar to those in the middle contact region. Compared to Fig. 5.7 (a), some peripheral regions became bright in (b) due to the detachment and the milling of local oxides. At the process time of (c), nearly the whole peripheral region exhibited a high brightness. As the process continued, the bright area further expanded to the inner region where the oxides were also milled into small particles. As shown in (d), nearly the whole contact area of the end contact region shows a high brightness. Due to APE, the contact area continued to expand, which is shown in Fig. 5.7 from (d) to (f). The expansion was in both the horizontal and vertical directions of the figure.

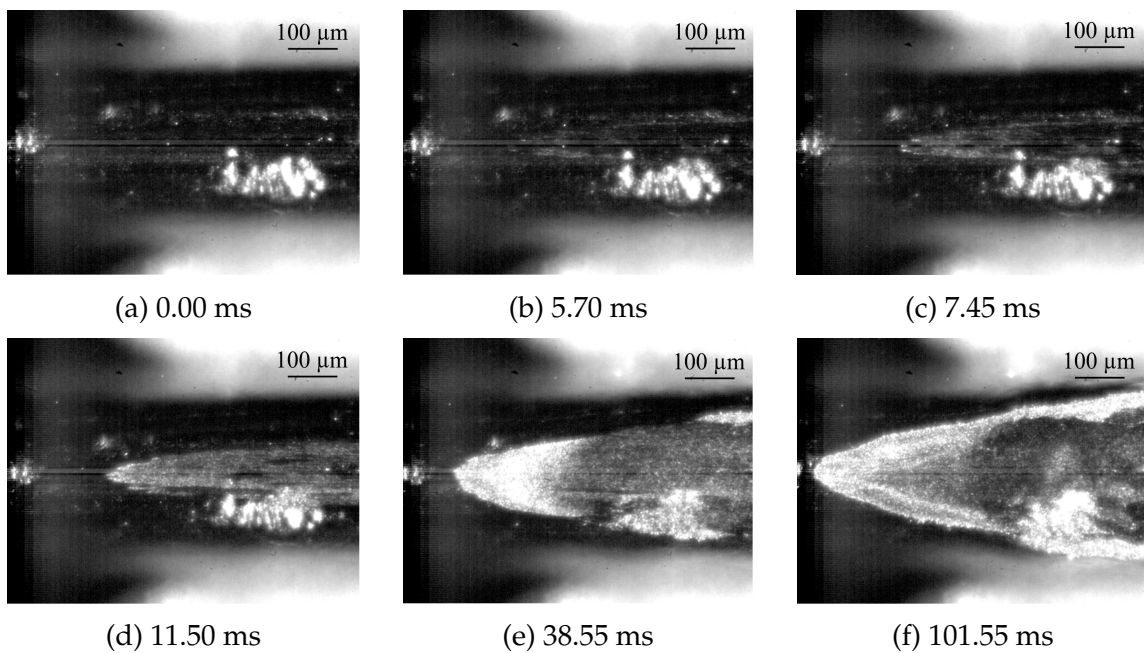


Fig. 5.7: The appearance and expansion of the stick area under 5 N, 2.2 W

After ~ 42 ms, a stick area appeared at one side of the peripheral region. The stick area at 59.50 ms is marked in Fig. 5.8 (a), as indicated by the arrow. As more microwelds formed, the stick area expanded. At the same time, new stick areas appeared. The coexistence of three stick areas at 119.75 ms is shown in Fig. 5.8 (b). As the expansion continued, these stick areas connected together and formed a large stick area. The final stick area is shown in Fig. 5.8 (c). This provides a hint that the stick area does not have to begin in the central region. More than one stick area can emerge from different local regions and coexist at the same time. As in the middle region, most oxides were transported to the peripheral region and some oxides were transported to the outside of the contact region, as shown in the red ellipses in Fig. 5.8 (c). In general, the changes of the five different areas in the end region are similar to those in the middle region.

Another phenomenon visible in the videos is the different relative displacement amplitudes at different positions of the contact area. To demonstrate this, three frames corre-

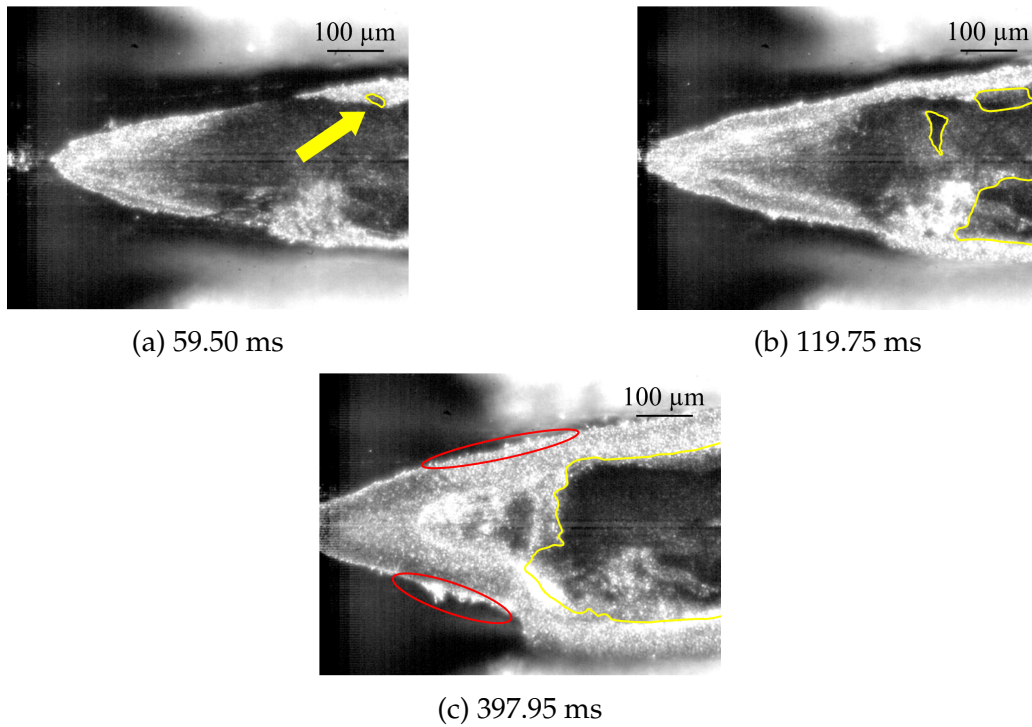


Fig. 5.8: The appearance and expansion of the stick area under 5 N, 2.2 W

sponding to 0° , 180° and 360° of an observation cycle were selected and shown in Fig. 5.9. The region marked by the yellow curve is the stick area and there was no relative motion. The green and red lines represent the lower-most and the upper-most positions of a local area of the wire, respectively. As indicated by the distance between the red and green lines, the local relative displacement amplitude was still large. This further supports the hypothesis that the relative displacement amplitudes at different interface locations are different.

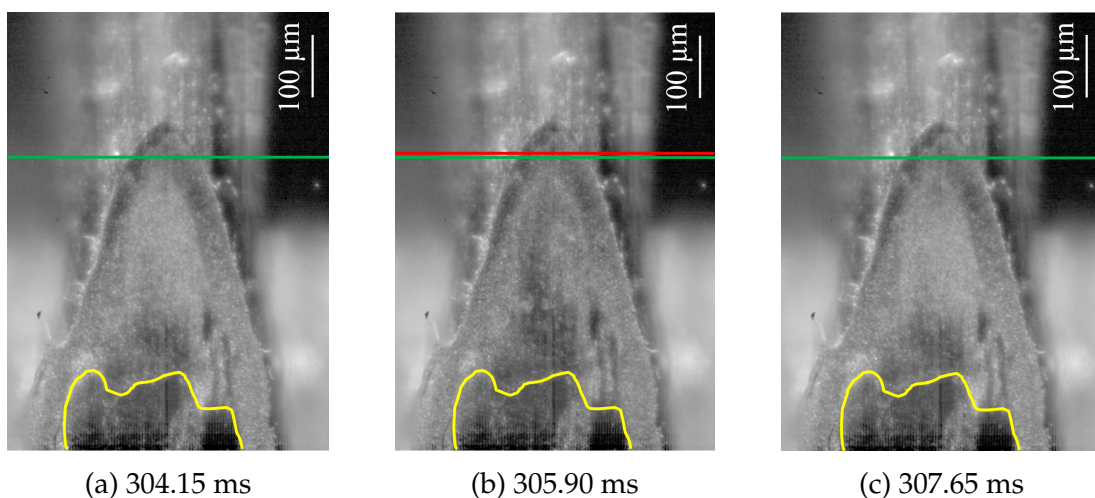


Fig. 5.9: The vibration of the wire under 5 N, 2.1 W

5.2.2 Validation of real-time observation by microscope

In the videos, the five different areas were mainly distinguished from one another by their brightness and contrast. To validate the above described hypotheses about the process, the wire/glass interface after the bonding process was cross-checked by a laser confocal microscope and SEM.

5.2.2.1 Validation by laser confocal microscope

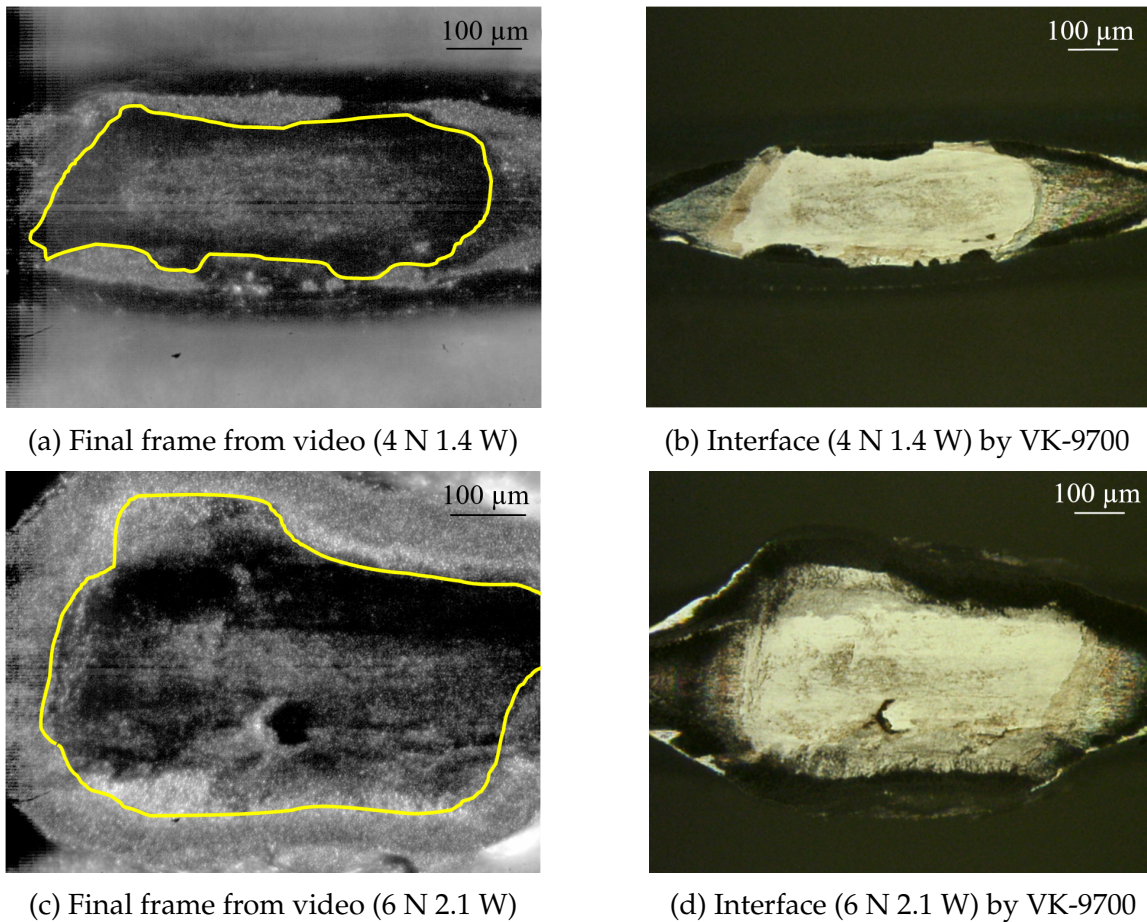


Fig. 5.10: Comparison of the bonding interface between the video and VK-9700

Table 5.1: Microwelds area and shear strength

Specimen	Shear force (N)	Microwelds area (μm^2)		Ultimate shear stress (MPa)	
		Video	Microscope	Video	Microscope
4 N, 1.4 W	3.77	39239.09	38761.19	96.08	97.26
5 N, 1.3 W	8.09	82373.17	86776.66	98.21	93.23
5 N, 2.4 W	7.84	84447.40	85173.07	92.84	92.05
6 N, 2.1 W	11.22	117183.66*	117269.01	95.75	95.68

*This value is smaller than the real value since the final microwelds area exceeds the recording window.

A Keyence VK-9700 laser confocal microscope was used to validate the areas shown in the videos. Comparisons between the video frames and the corresponding microscope

images are shown in **Fig. 5.10**. The yellow curves in (a) and (c) show the boundaries of the stick areas. In the microscope images (b) and (d), the white flat areas in the central region indicate the microwelds area. The remaining areas were covered by oxides and not bonded. It is apparent that the stick areas detected by the videos fit the microwelds area detected by the microscope well. In addition, the oxides areas detected by the videos fit the non-bonded areas detected by the microscope as well. The peripheral regions in (b) and (d) show a low brightness. They also fit the peripheral regions in (a) and (c), correspondingly. For a quantitative comparison, the microwelds areas detected by the videos and the microscope were counted in **Table 5.1**. In the tested processes, the values from the video and the microscope are close to each other. To conclude, the recognition and description of the five areas in last sections are supported by the microscope observations.

The specimens in **Table 5.1** were shear tested and the results are also shown in the table. The ultimate shear stress of the microwelds was then calculated by dividing the shear force over the microwelds area. The value from the videos is 95.72 ± 2.21 MPa and the value from the microscope images is 94.56 ± 2.35 MPa. With these values, the metal-glass bonding strength can be predicted by both videos and the microscope.

5.2.2.2 Validation by SEM

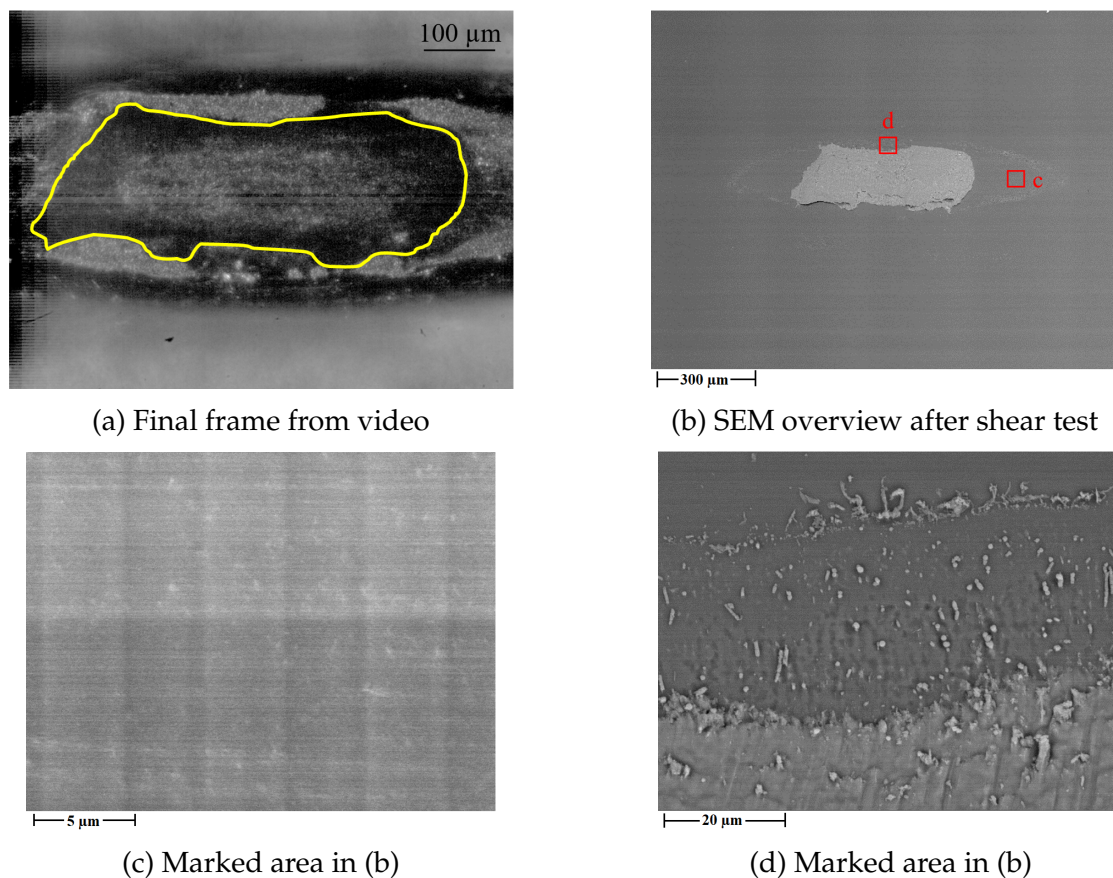


Fig. 5.11: SEM observation of wire/glass interface for 5 N, 1.3 W

The different areas are further validated by SEM after the mechanical removal of the wire.

The SEM images for the specimen 5 N, 1.3 W are shown in **Fig. 5.11**. The stick area in (a) fits the aluminum residue in (b) well. Even though some oxides remain within the stick area, the microwelds surrounding the oxides were strong enough to keep the aluminum residue from being removed by the shear test. The aluminum residue was then etched off by peroxymonosulfuric acid (H_2SO_5). A small amount of oxides was found after the etching. The exposed surface has a roughness of R_a 1.24 nm which is close to the roughness before bonding. This indicates that no serious wear took place in this region. Nearly no oxides were found in the two end regions as in (c). The oxides in these regions were supposed to be removed together with the wire during the shear test. In contrast, large amounts of oxides existed in the peripheral region as in (d). Serious wear of the glass surface was also observed. This region is in accordance to the area outside of the yellow curve in (a). As a result, the contact area, friction area and stick area were validated by the SEM images.

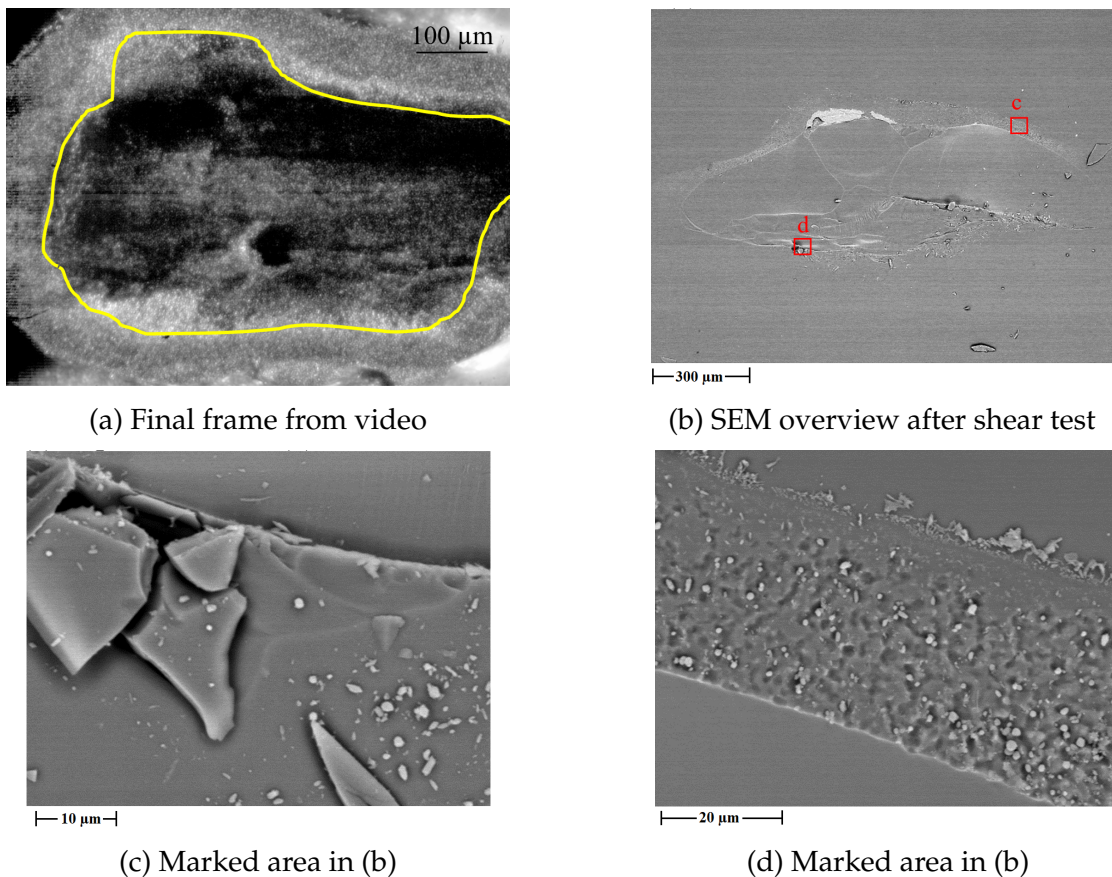


Fig. 5.12: SEM observation of wire/glass interface for 6 N, 2.1 W

Additionally, many particles in the peripheral region have a spherical or cylindrical shape. This might indicate the occurrence of a high flash temperature which caused the melting of aluminum.

The results for the 6 N, 2.1 W specimen are shown in **Fig. 5.12**. (a) is the final frame of the video and (b) to (d) are the SEM images. As shown in (b) and (c), the glass fractured during the shear test. Therefore, the stick area in (a) cannot be compared with the aluminum

residue which was removed together with the glass. The traces on the fractured glass surface, however, indicate a high bonding strength. On the other hand, the large amount of oxides in (d) indicate that the peripheral region in (a) was not bonded. The glass surface in the peripheral region was also seriously worn. As for most of the other specimens, glass fractures and aluminum residues coexisted. In these cases, only the friction area can be validated by SEM.

5.2.3 Impact of process parameters

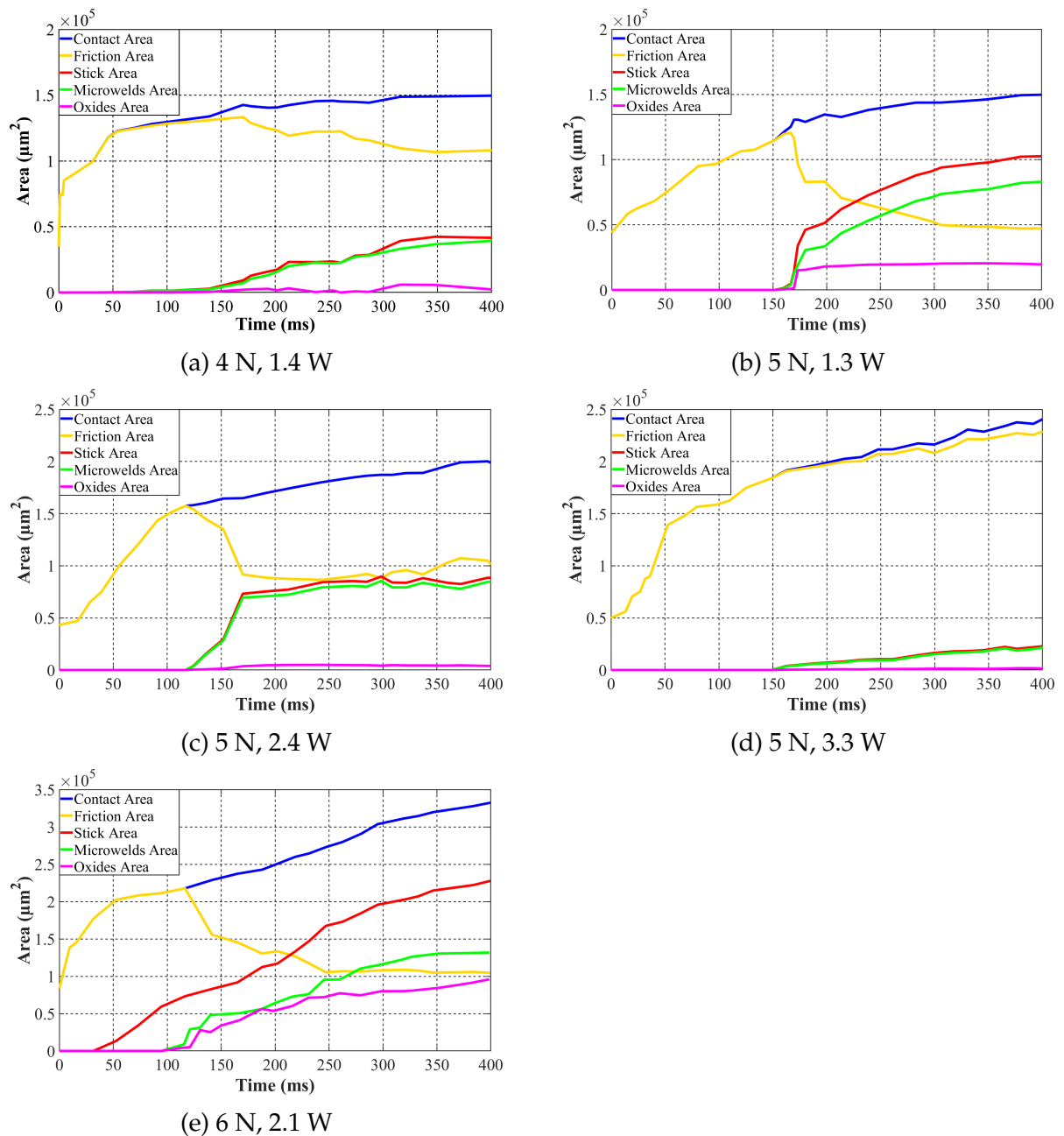


Fig. 5.13: Growth of different areas under different settings

The process parameters including the normal force and the US power were varied to study their impact on the five different areas. Five processes under different settings were recorded by the real-time observation system. The five different areas were then counted. Their changes over the process time are shown in **Fig. 5.13**. The microwelds area represents the shear strength, as in **Table 5.1**. The shear force of the 5 N, 3.3 W specimen is not provided due to its undetectable low strength.

In all cases, the contact and friction areas first show a rapid increase and the increase then becomes slower. The contact area finally reaches a constant value. Due to the emergence of the stick area, the friction area decreases before reaching a constant value. After a certain time required for continuous plastic deformation and friction, the stick, microwelds and oxides areas appear almost simultaneously. In most processes, they had a fast growth period after their emergence. After this period, the growth of the three areas become slower until the end of the processes.

When the US power is kept constant, the increase of the normal force significantly enhances the contact, stick and microwelds areas while the friction area stays nearly the same. This is shown in **Fig. 5.13** (a) (c) and (e). Naturally a larger normal force during the Pre-deformation stage results in a larger initial contact area. If the US vibration induced APEs are the same, a larger normal force leads to a larger final contact area. This large contact area offers a large potential area for microweld formations. These can be seen from the corresponding curves. On the other hand, a large contact area also means that more oxides are involved and large amounts of oxides could remain after the bonding process. An obvious enlargement of the oxides area occurs in (e). Since either the microwelds area or the oxides area is enlarged, the stick area gets larger.

When the normal force stays the same, the increase of the US power increases the contact and friction areas while the stick and oxides areas shrink. The contact area grows as more US energy is used for APE. A larger US power also leads to a larger vibration amplitude of the tool. Under the same normal force, the tangential stress increases. The resulting large tangential stress could damage the pre-formed microwelds and inhibit the formation of new microwelds. As a result, the stick area or even the microwelds area decreases. The decrease of the oxides area indicates that a higher US power is beneficial for oxide removal within the stick area. When a too high US power is applied, as shown in (d), the detrimental effect of excessive vibration on the microwelds formation significantly increases. Finally, only a small area of microwelds are formed.

All in all, the normal force and US power interactively influence the different areas. To obtain a desired bond, an appropriate combination of the normal force and US power must be selected.

An important indicator for the bonding process is the self-cleaning efficiency. As stated in Section 5.2.2.1, when the microwelds in a local region were damaged, the oxides flew back to that region. Therefore, the microwelds area is considered as the clean area in

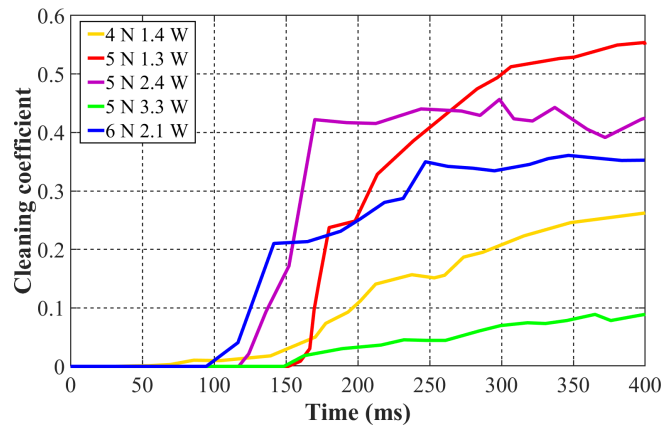


Fig. 5.14: Impact of process parameters on cleaning efficiency within contact area

this work. The cleaning efficiency is then calculated as the ratio of microwelds area over contact area. The changes of the cleaning efficiency under different settings are shown in **Fig. 5.14**. Similar to the change of the stick and microwelds area, the cleaning efficiency shows fast initial growth and then reaches a constant level. These changes are determined by the continuous plastic deformation, the positive effect of vibration on oxide removal and the detrimental effect of excessive vibration on microwelds. The comparison of the cleaning efficiency among the five processes is given below:

1. As shown in the figure, the 5 N, 3.3 W process has the smallest value and the slowest incremental curve. This is mainly caused by the detrimental effect of excessive vibration.
2. As the US power decreases (1.4 W), the vibration becomes more effective for oxide removal.
3. The 1.4 W power, however, is still comparably large for 4 N normal force. Therefore, the 5 N, 1.3 W process has a much larger cleaning efficiency.
4. For the 6 N, 2.1 W process, the detrimental effect of excessive vibration almost vanishes. Due to its large contact area, however, its cleaning efficiency is lower than that of the 5 N, 1.3 W process.
5. Balanced by the detrimental effect of excessive vibration and the decrease of the contact area, the cleaning efficiency of 5 N, 2.4 W lies between the 6 N, 2.1 W process and the 5 N, 1.3 W process.
6. The cleaning efficiency is not the only indicator of the bonding quality (strength). The bonding strength is also significantly influenced by the contact area. Hence, both the contact area and the cleaning efficiency shall be taken into consideration to achieve the desired bonding strength.

5.2.4 Movement of oxide particles

Due to the uneven distribution of the normal stress in the end contact regions, the tangential stresses vary significantly, especially in the beginning stage. If the tangential stress in a local region is smaller than a critical value, the oxides in this region cannot be milled into small particles. This region thus shows a low brightness even when the other regions become bright. Since oxide particles have a high brightness, the movement of these particles in the dark regions can be observed.

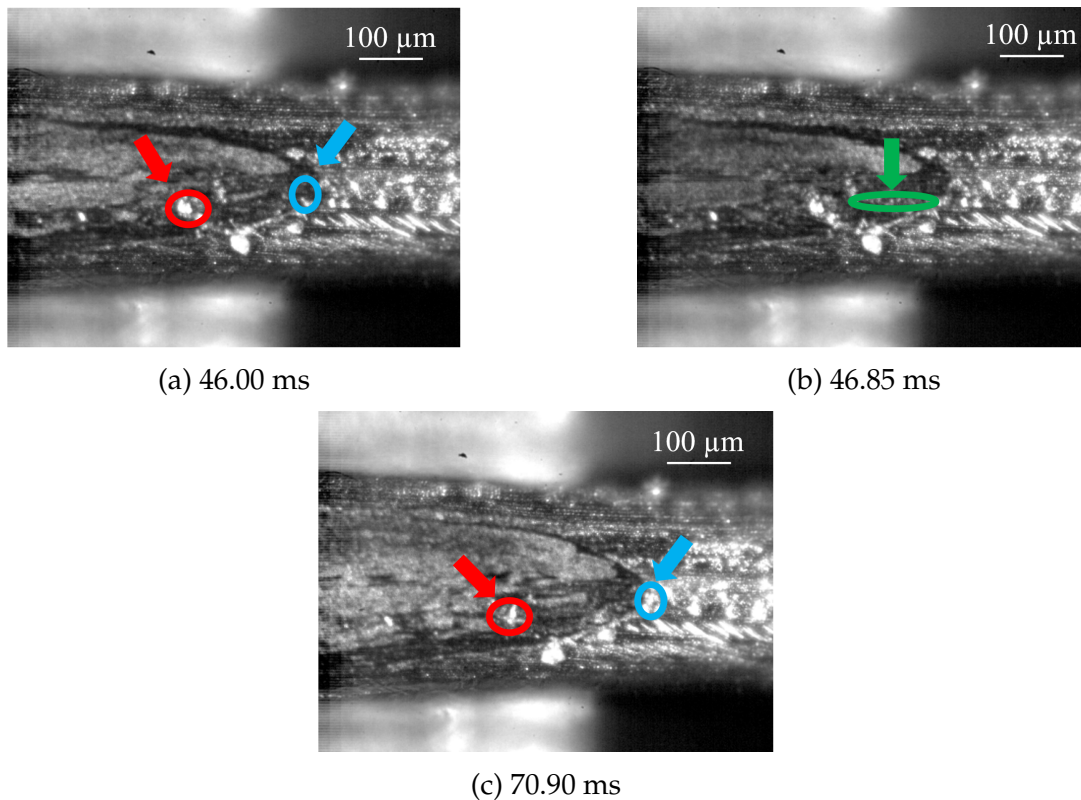


Fig. 5.15: Moving of oxide particles under 6 N, 2.0 W

One example for the movement of particles is shown in Fig. 5.15. As shown in the figure, the inner contact area shows a high brightness while the peripheral region stays dark during the movement period. The movement of these particles was observed in the peripheral dark region. (a) and (c) are the frames where the movement started and ended, respectively. The red and blue circles respectively show the initial and final positions of the moving particles. The movement of particles at 46.85 ms was snapshot and is shown in (b). The yellow ellipse marks the position of these oxide particles at a moment of movement. Finally, most of the particles in the red circle were transported to the area in the blue circle. Since there was nearly no material flow, the movement of these particles evidently confirms the significant role of US vibration on oxides transportation.

5.3 Oxide removal with coated wire or glass

Section 5.2 investigated the changes of the friction area and oxides area. The oxide removal mechanisms, however, are still unclear. Due to the low thickness of the natural oxide layer, the information attained was insufficient. In this section, the oxide removal mechanisms will be analyzed via the addition of artificial coatings.

5.3.1 Oxide removal mechanisms

5.3.1.1 Cracks, detachment and milling

As mentioned before, the first step of the oxide removal process is the generation of cracks in the pre-deformation stage. This can now be clearly observed in **Fig. 5.16** (a) where a 5 N force was loaded on a 50 nm Al_2O_3 coated wire. Cracks were generated during the loading of the 5 N force. The cracks were concentrated in the peripheral region, especially in the two end regions, which is in accordance to [21]. Most cracks exhibit a direction which is perpendicular to the wire direction. This indicates that significant stresses existed in the peripheral region and a large strain gradient distributed in the wire direction. Under the tested range (up to 6 N), no oxides were detached due to the pre-deformation induced material flow.

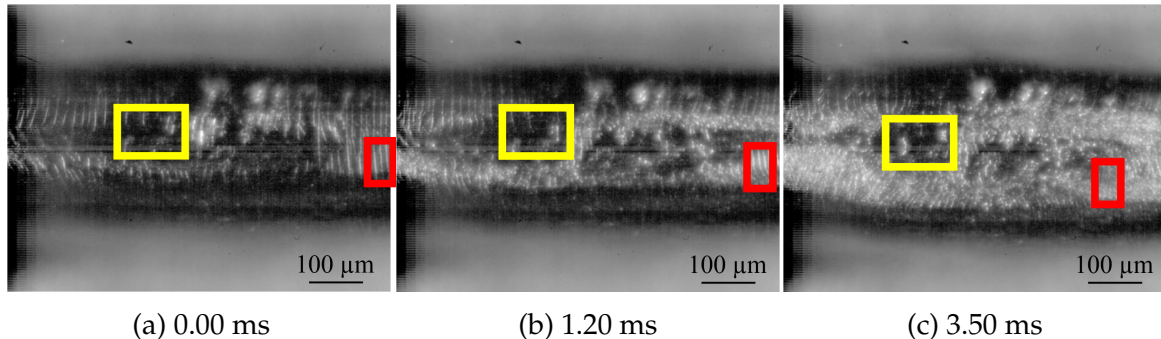


Fig. 5.16: Cracks, detachment and milling of Al_2O_3 coated layer at the wire/substrate interface for 5 N, 1.4 W

As the US vibration of the tool was activated, the detachment of the oxides started and the detachment was characterized by the following features:

1. The oxides in the peripheral region were first detached from the pure metal surface.
2. After detachment, the oxides were still in the form of flakes. An example of this are the oxides in the red square of **Fig. 5.16** (b).
3. The high-speed video shows that the direction of the detachment was from the two end regions towards the middle of the contact region. This can also be seen from the movement of the oxides in the red rectangle of **Fig. 5.16** from (a) to (c). During the detachment period, the vibration of the wire was in the status of micro-slip.

The inward movement of the peripheral slip region might cause such a detachment direction.

4. The inward motion of the detached oxide flakes squeezed the inner oxide layer and caused more cracks and detachment at the central contact region.

After the detachment, the vibration of the wire kept on and continuous oscillatory stress was imposed on the flakes. With further tens to hundreds of vibration cycles, the oxide flakes were milled into small particles. Since particles have many more facets, they could reflect more light into the camera. Therefore, the areas with particles are much brighter than the areas with flakes in the figures. This milling step, which has not yet been mentioned in the literature, should be added into the oxide removal process between detachment and transportation.

The normal force and US power significantly influence the milling process. For the process shown in **Fig. 5.16**, a 1.4 W US power was applied. This low power could not introduce large relative displacement into the central region. Therefore, the oxides flakes in the central region were not milled into small particles, as can be seen from the oxide flakes in the yellow rectangle of **Fig. 5.16**. When the normal force increased to 6 N and a similar US power was applied, the oxide flakes in the central region became larger. When a greater US power (e.g. 3.0 W) was applied while the normal force was kept at 5 N, all the flakes in the central region were milled into small particles. As a result, a greater US power shall be selected in the beginning stage of the bonding process since it aids the milling of oxides.

5.3.1.2 Metal penetration through the oxide layer

After the milling of the oxides, the oxide particles are transported to the peripheral contact region or the outside of the contact region. Many mechanisms for the oxide transportation were detected in this work. One of them is metal penetration, which means the metal penetrates the oxide layer and touches the substrate. Metal penetration is mainly caused by the vibration induced relative motion. It was found in all the high-speed videos of the coated wire bonding processes. This phenomenon is more obvious for the ZrO_2 coated wire than for the Al_2O_3 coated wire. As a result, only an example of the ZrO_2 coated wire is explained in this section.

As shown in **Fig. 5.17** (a), the oxides in the peripheral region have been milled into small particles at ~ 20 ms. Due to the low US power, the oxides in the yellow ellipse were still in the form of flakes. The conversion from flakes to particles made the metal penetration easier. After tens of vibration cycles, the pure metal at a local position penetrated the particle layer and touched the glass substrate. At the same time, the local oxide particles were squeezed into the surrounding area. At the process time of **Fig. 5.17** (b), the pure metal had penetrated the oxide layer at four different locations, marked by the red ellipses. As the metal penetration continued, more oxides were squeezed out and a larger area of metal-glass contact was achieved, as shown in **Fig. 5.17** (c). Due to the small relative displacement in the central region (yellow ellipse), the oxide flake was not milled

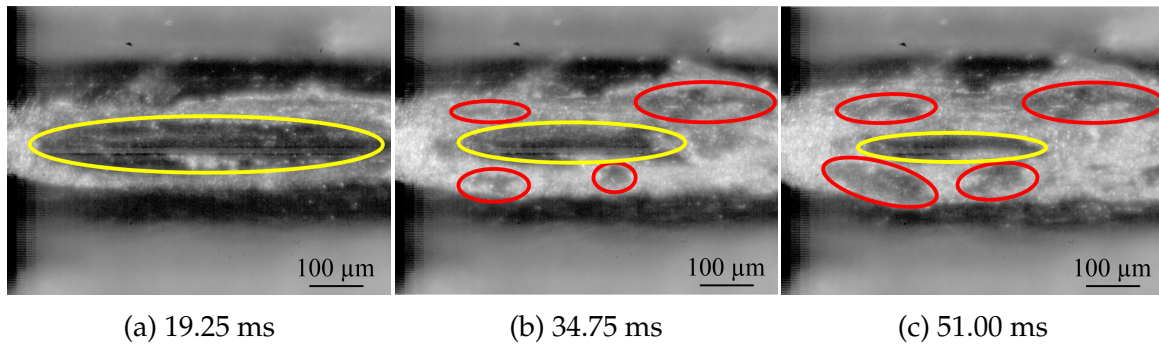


Fig. 5.17: Metal penetration of the 50 nm ZrO_2 coated layer at the wire/substrate interface for 5 N, 1.1 W

into particles and no metal penetration occurred.

5.3.1.3 Oxide flow and metal splash

Another mechanism for oxide transportation is oxide flow. Under the vibration induced relative motion and the unevenly distributed normal stress, oxides usually flow from the central region to the peripheral region. In fact, the oxide flow has been demonstrated in Section 5.2.4 with uncoated wire.

The oxide flow was also observed with the coated wire. When oxide flakes were present in the central region, the oxide particles surrounding the flakes flew along the edges of the flakes towards the peripheral region. It was observed in all videos that some oxides flew to the outside of the contact region.

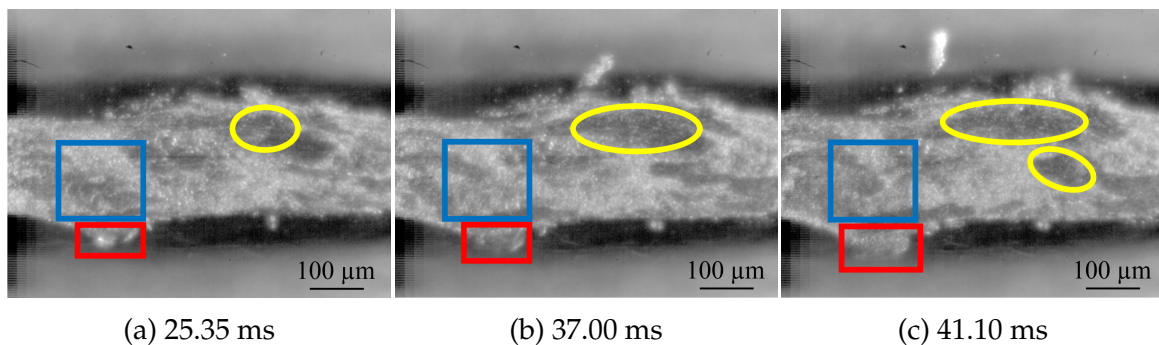


Fig. 5.18: Oxide flow with metal splash at the wire/substrate interface with ZrO_2 coated layer for 5 N 2.2 W

A profound oxide flow phenomenon was observed in the bonding of a 50 nm ZrO_2 coated wire. In addition to the oxide flow, a metal splash which is a thin metal layer was generated. It is usually squeezed out from a soft material when the soft material is bonded with a hard material. As shown in the red rectangle of Fig. 5.18 (a), a metal splash occurred. It first broke the oxide layer at the boundary of the contact and then grew. During the generation of the metal splash, large amounts of oxides in the blue square of Fig. 5.18 flew out together with this thin metal layer. As the growth of the metal splash continued, more and more oxide particles flew out. This was clearly captured by the high-speed video. In

Fig. 5.18, however, it can only be seen that the amount of oxides (bright area) in the blue square significantly decreased from (a) to (c). After the process time of **Fig. 5.18** (b), the metal splash rolled up, which was observed in the video. Therefore, the real area of the splash at 41.00 ms was larger than that in the red rectangle of **Fig. 5.18** (c). This example also indicates that the existence of a metal splash would facilitate the transportation of oxide particles to the outside of the contact. Metal splash existed for nearly all the coated wires and the growth was faster than that for non-coated wire. The reason for this could be attributed to the smaller friction coefficient as more oxide particles were introduced into the interface. Specifically for the process in **Fig. 5.18**, the growth speed of the metal splash was the highest in the recorded processes. As a result, the flow speed of the oxide particles, which is associated with the growth speed of the metal splash, was higher than that in other processes.

Metal penetration also occurred, as marked in the yellow ellipses in **Fig. 5.18**. In this process, the oxide transportation caused by oxide flow and metal splash, however, is more prominent.

5.3.1.4 Pushing

The last transportation mechanism detected in this work is pushing. It was caused by the material flow at the wire/substrate interface and was mainly observed when the oxide layer was coated on the glass substrate. This indicates that pushing plays a more important role in removing oxides on substrates than removing oxides on wire.

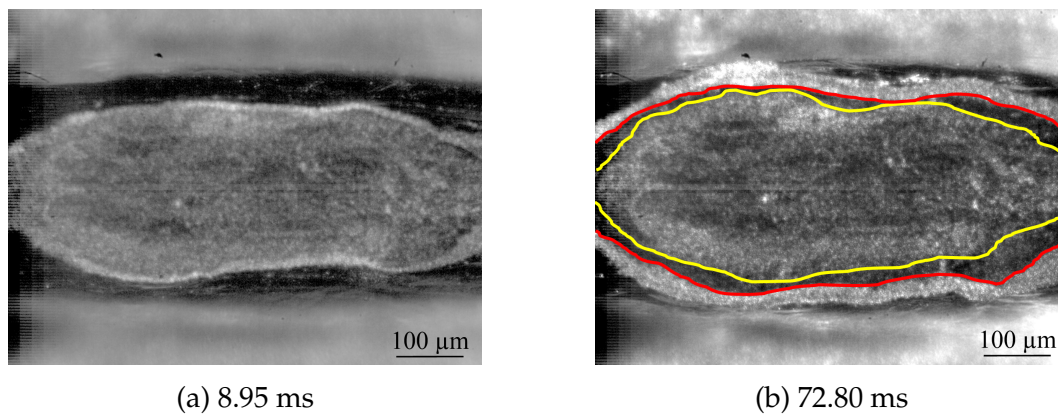


Fig. 5.19: Pushing by material flow for the bonding on ZrO_2 coated glass under 6 N 1.8 W

An example is given for the bonding process with ZrO_2 coated glass under 6 N, 1.8 W. After undergoing the US vibration for a few milliseconds, nearly the whole contact area became static, as shown in the yellow borders of **Fig. 5.19** (a). Since no oxide transportation was observed and this area exhibits a high brightness, most oxides remained within the contact area. Due to the acoustoplastic effect (APE), the plastic deformation as well as its induced material flow continued. The reciprocating relative motion was observed within a narrow band in the peripheral region. During the expansion of the contact area, a dark band emerged on the expansion path, as shown in **Fig. 5.19** (b) between the yellow

and the red borders. Indicated by the low brightness, most oxides within this band area were transported to the outside of the red borders. As the dark band fitted the material flow path and emerged after the material flow passed this band region, the significant role of transportation is attributed to the material flow.

5.3.1.5 Impact of the coated oxide on bonding strength

During the observation of coated bonding processes (the bonding processes with coated oxide layer either on the wire or on the substrate), an interesting phenomenon was found: the fast expansion of the stick area. During both the coated and non-coated bonding processes, the stick area expanded from a tiny area to nearly the whole central contact area. It usually took ~ 200 ms for the expansion under non-coated conditions. Under coated conditions, however, only a few tens of milliseconds were required. In some situations, e.g. the process in **Fig. 5.19**, the time for expansion (a few milliseconds) was even shorter. Since the emergence of the stick area was due to microwelds formation which constrained the vibration of the local wire, the expansion of the stick area indicated the formation of more microwelds. From this point of view, the coated bonding processes had a higher microweld formation rate, at least on the expansion path of the stick area.

On the other hand, it seems that more oxide particles remained within the stick area for the coated bonding processes. This can be determined by the brightness distribution within the stick area. As mentioned before, a high brightness in a local stick area indicates the existence of oxides while a low brightness indicates the formation of local microwelds. For coated bonding processes, most of the stick area showed a high brightness, even on the expansion path. From this point of view, the shear strength of coated bonds (bonds under coated conditions) was expected to be low, as the remaining oxides prevent the formation of microwelds.

In conclusion, it is hard to predict the strength of the coated bonds due to the contradiction between the microwelds formation rate and the high brightness area. Therefore, shear tests must be conducted.

Table 5.2: Bonding strength under 6 N 2.0 W for different conditions

Bonding condition	Shear strength (N)
Al wire - Glass	7.1
50 nm Al ₂ O ₃ coated wire — Glass	13.3
50 nm ZnO ₂ coated wire — Glass	17.2
Al wire - 50 nm Al ₂ O ₃ coated Glass	19.2
Al wire - 50 nm ZnO ₂ coated Glass	17.4

The results of the shear tests are shown in **Table 5.2**. The process parameters were 6 N, 2.0 W and 400 ms. In general, the shear strength of coated bonds is 2~3 times higher than that of uncoated bonds. This considerable difference might be explained by two assumptions: 1) The coated oxides facilitated the formation of microwelds and the final microwelds area was larger. There were large amounts of local areas in which oxides had been removed

and microwelds were formed. These areas, however, were smaller than the resolution of the camera and were surrounded by oxides. Therefore, they cannot be detected from the high-speed videos; 2) Different bond types exist for metal-glass bonding and the coated oxides changed the ratio of these bond types over the total microwelds area. For metal-glass bonding, more specifically for Al-SiO₂ bonding in this work, either metallic bonds (Al-Si) or ionic bonds (Al-O and Si-O) were formed at different locations. It is known that different bond types have different bond energies. Therefore, when the ratio of the different bond types was significantly changed by the coated oxides, the final wire bonding strength greatly differed. These assumptions need further experimental validation.

5.3.2 SEM observation of metal-glass bonding interfaces

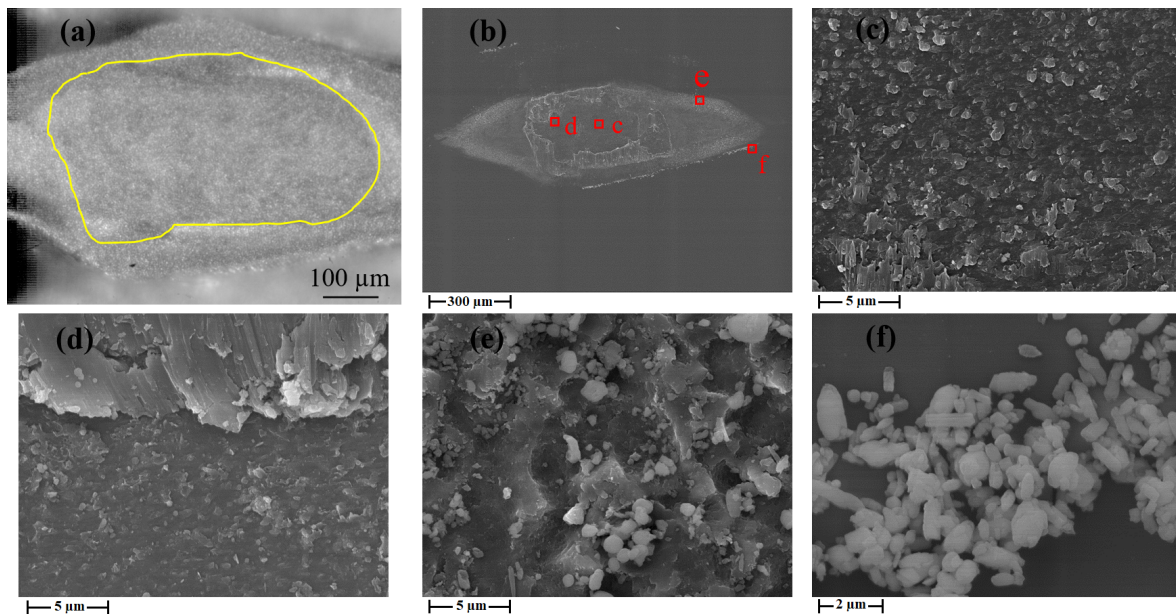


Fig. 5.20: The bonding interface with Al_2O_3 coated wire after the process under 5 N 1.7 W (a) the final frame from video (b) SEM overview after shear test (c)-(f) marked area in (b)

The specimen of an Al_2O_3 coated wire bond for 5N 1.7 W was shear tested and the SEM observations on the bonding interface are shown in Fig. 5.20. The images are explained as the following:

1. (a) is the last frame of the high-speed video and the yellow curve indicates the final stick area. It is hard to distinguish the microwelds area from the oxides area in (a) as nearly all areas exhibit a high brightness.
2. (b) shows the bonding interface after the shear test. It can be seen that the contour of the aluminum residue in (b) fits the stick area boundary in (a) well.
3. The high brightness within the yellow curve indicates that many oxides remained in the stick area. After the shear test, however, nearly no oxides were observed in the stick area, as shown in (b), or in the magnified areas of (c) and (d). This can be

explained by the following: since the glass is much harder than aluminum, most oxides were assumed to be embedded into the surface of the wire; during the shear tests, most oxides were removed together with the wire.

4. (c) shows that slight wear occurred in the central area. (d) shows the inner boundary between the aluminum residue (upper side of the image) and the worn glass surface (lower side of the image). A severe worn surface was observed in (e). Comparing the surface in (c)-(e) to the corresponding images of the non-coated bond surface (in Fig. 5.11 and Fig. 5.12), the wear became more serious for coated processes.
5. The oxide particles which were transported to the peripheral region and the outside of the contact were shown in (e) and (f), respectively. It can be seen that most oxides were transported to such regions.
6. Most of the oxide particles in (e)(f) have a spherical or a cylindrical shape. This could indicate an occurrence of the melting of aluminum. And thus, a high flash temperature might occur during the bonding process. Further experimental validation is required for this assumption.

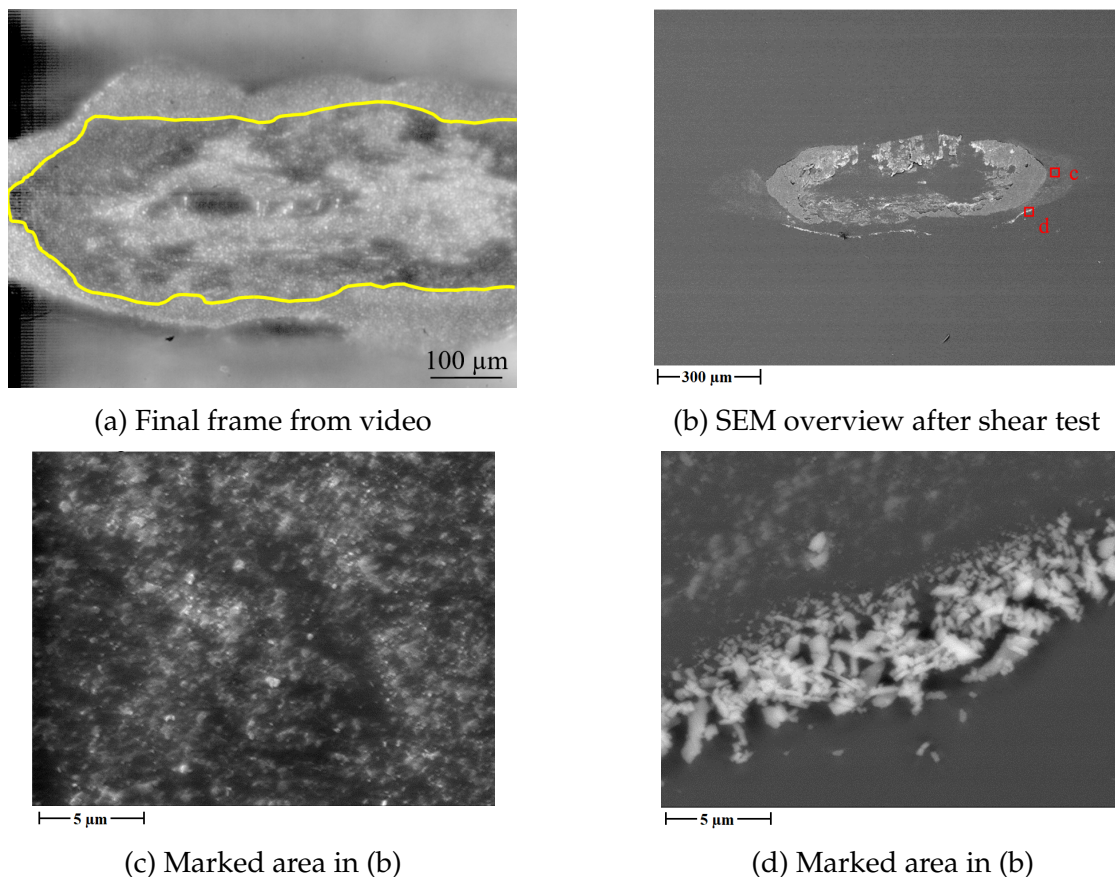


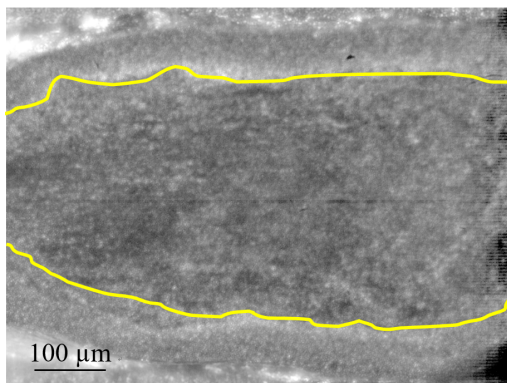
Fig. 5.21: The bonding interface with ZrO_2 coated wire after the process under 5 N, 1.1 W

Another specimen with ZrO_2 coated layer was also analyzed by SEM and the resulting images are shown in Fig. 5.21. The following conclusions can be drawn:

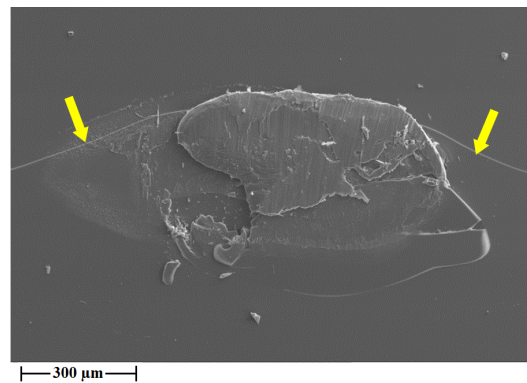
1. As the above, (a) is the last frame of the video. As the stick area within the yellow

curve shows a clear brightness distribution, it is now possible to distinguish the microwelds area from the oxides area. The central region within the yellow curve, which has a high brightness, is supposed to have large amounts of remaining oxides. As a result, no microwelds were formed in this region. The peripheral region of the stick area, which exhibits a low brightness, is the region where microwelds were assumed to form.

2. The SEM overview of the bonding interface in (b) validates the recognition of the different areas in last item. The aluminum residue enclosed area fits the stick area in (a) well. The non-bonded area inside the aluminum residue in (b) also fits the central bright area in (a) well.
3. The wear in a local peripheral region is shown in (c). Compared to Fig. 5.20 (e), the surface was less damaged. This is due to the lower hardness of ZrO_2 particles.
4. As shown in (d), large amounts of oxides were transported to the outside of the contact. This is a common feature which was observed in all SEM observations of the bonding interfaces.



(a) Final frame from video



(b) SEM overview after shear test

Fig. 5.22: The bonding interface with Al_2O_3 coated glass after the process under 6 N, 2.6 W

The interfaces of the bonds with coated glass substrates were also observed with SEM. No additional information was revealed from the above-mentioned interfaces. When checking the interfaces with a large shear strength (> 17 N), however, a featured interface was exposed. An example is provided in Fig. 5.22. It was a bond with Al_2O_3 coated glass under 6 N, 2.6 W. Three features can be derived:

1. The aluminum residue contour in (b) fits the stick area detected from the video in (a) well. It can be seen that the whole stick area was covered by microwelds.
2. The glass fractured and it covered nearly the whole contact area.
3. A long fracture line, as indicated by the yellow arrows, existed.

The shear strength of such metal-glass bonds is similar to that of Al-Al bonds. This also indicates that a 50 nm oxide coating is beneficial for Al-glass bonding.

5.3.3 Validation of oxide removal mechanisms

5.3.3.1 Validation by a thick Al_2O_3 layer

A 200 nm Al_2O_3 layer was deposited on the wire to confirm if the above-mentioned oxide removal mechanisms take place under different conditions. One of the processes is shown in Fig. 5.23. It is described as below:

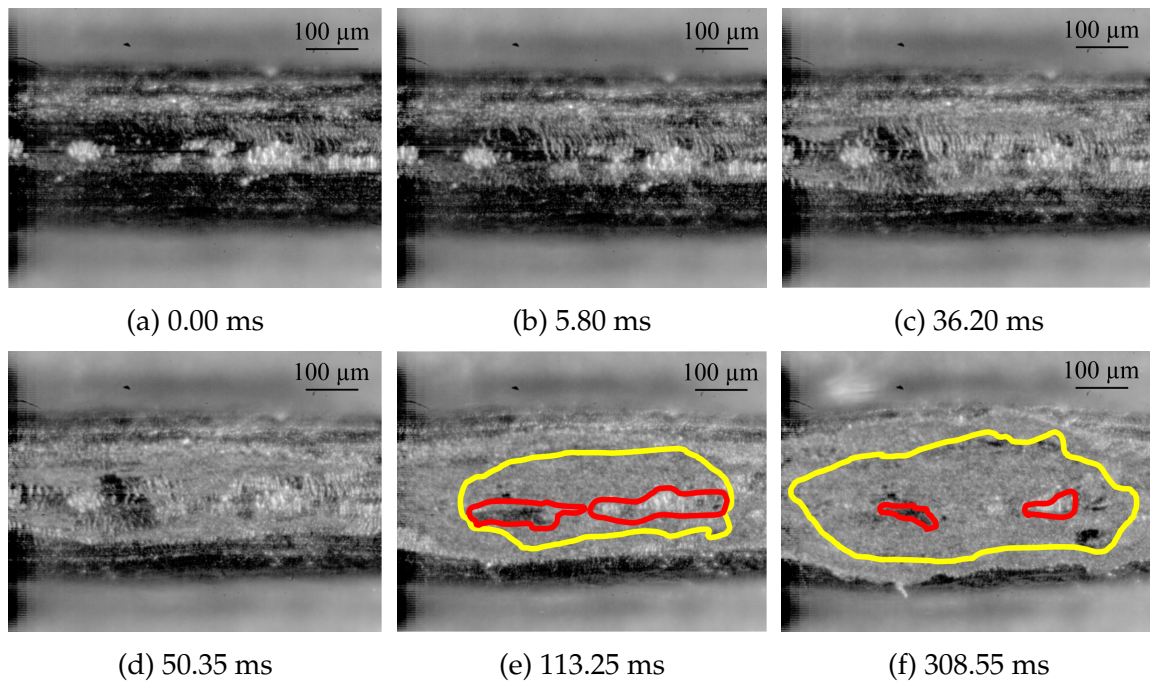


Fig. 5.23: The bonding interface with 200 nm Al_2O_3 coated wire under 5 N, 1.4 W

1. As shown in (a), cracks occurred after the loading of the normal force.
2. After the activation of US vibration, no obvious oxide detachment was observed. Instead, more cracks were generated and some of the normal force induced cracks extended. This can be noticed when comparing the cracks in (b) with those in (a).
3. During this period (0~6 ms), no obvious material flow in the wire direction was observed from the video. Therefore, the increase of the crack intensity was attributed to the vibration induced relative motion.
4. US vibration continued after the process time of (b). The crack intensity also continued to increase. In the meantime, oxides in the peripheral region of the contact started to detach. The detachment process, however, was different from that of the 50 nm Al_2O_3 coated bonding process. During the 50 nm Al_2O_3 coated bonding process, the local oxide layer with a thickness of 50 nm was detached at once. For the 200 nm coated bonding process, however, the 200 nm oxide layer was not detached all at once and the detachment took a longer time. From the video, it can be seen that in the beginning of the detachment process, only the top layer of the oxide was detached and then milled. Such a situation is shown in (c). The high brightness in

the peripheral region indicates that some oxides had been detached and milled into small particles.

5. As vibration continued, more and more of the coated oxide was detached. It is hard to determine when the 200 nm oxide at local positions was totally detached. At the process time of (d), it can be only seen that most of oxides in the peripheral region were detached.
6. The bright area then extended to the central contact region and the crack intensity increased further. Until the process time of (e) when a large area (marked by the yellow curve) became static, there were still two sliding areas (marked by the red curves).
7. The contact and the stick area continued to expand. The two sliding areas still existed at the process time of (f), but became smaller.
8. Oxide flow and metal splash were also observed in the video. Since they were similar to those in the 50 nm Al_2O_3 coated bonding process, no corresponding frames were selected and shown here.

Through this bonding process, cracks, detachment, milling, oxide flow and metal splash were observed. Due to the thickness of the oxide layer, the pure metal of the wire was not able to penetrate the oxide layer. And since no oxide was deposited on the substrate, no pushing occurred. To conclude, the above detected oxide removal mechanisms are still valid for the bonding process with 200 nm Al_2O_3 coated wires.

Since too much oxide was present at the interface, the bonding strength significantly decreased.

5.3.3.2 Validation by coating on both wire and glass

When the wire and the substrate are made of aluminum or copper in metal-metal bonding, oxides exist on both the wire and the substrate. This condition is also tested in metal-glass bonding to validate the oxide removal mechanisms. To create such a condition, a 50 nm Al_2O_3 layer was deposited on the wire and a 50 nm ZrO_2 layer was deposited on the glass. The process is shown in Fig. 5.24 and described as follows:

1. Since the Al_2O_3 was coated on the wire, cracks due to the normal force loading were observed in (a).
2. Immediately after the activation of US vibration, the extension of cracks was observed. This can be seen in (b) where cracks are much longer than those in (a).
3. In the meantime, an area (marked by the yellow ellipse in (b)) became brighter. This is assumed to be induced by the detachment and milling of the ZrO_2 on the substrate. In addition, this area is located in the central region, which is different from the previously described processes. It indicates that the coating on both bonding partners significantly changed the friction conditions at the interface.

4. As vibration continued, the detachment and milling of the Al_2O_3 oxide also began. An example of this is the oxides in the red squares of (b) and (c). These oxides were detached at the process time of (b). In (c), they had been milled into small particles.
5. The areas where Al_2O_3 or ZrO_2 were detached and milled expanded and connected. The connected area at the process time of 24.05 ms is shown in (d).
6. During the expansion, the two different kinds of oxides mixed.
7. At the process time of (e), nearly all the oxides over the contact area were milled into particles. The extension of the cracks in the peripheral region, however, continued.
8. In (f), the central region had stuck on the substrate. Metal splashes can be observed at the lower-left and the upper-right corners of the image.
9. Due to the influence of the Al_2O_3 layer, pushing was hard to observe.

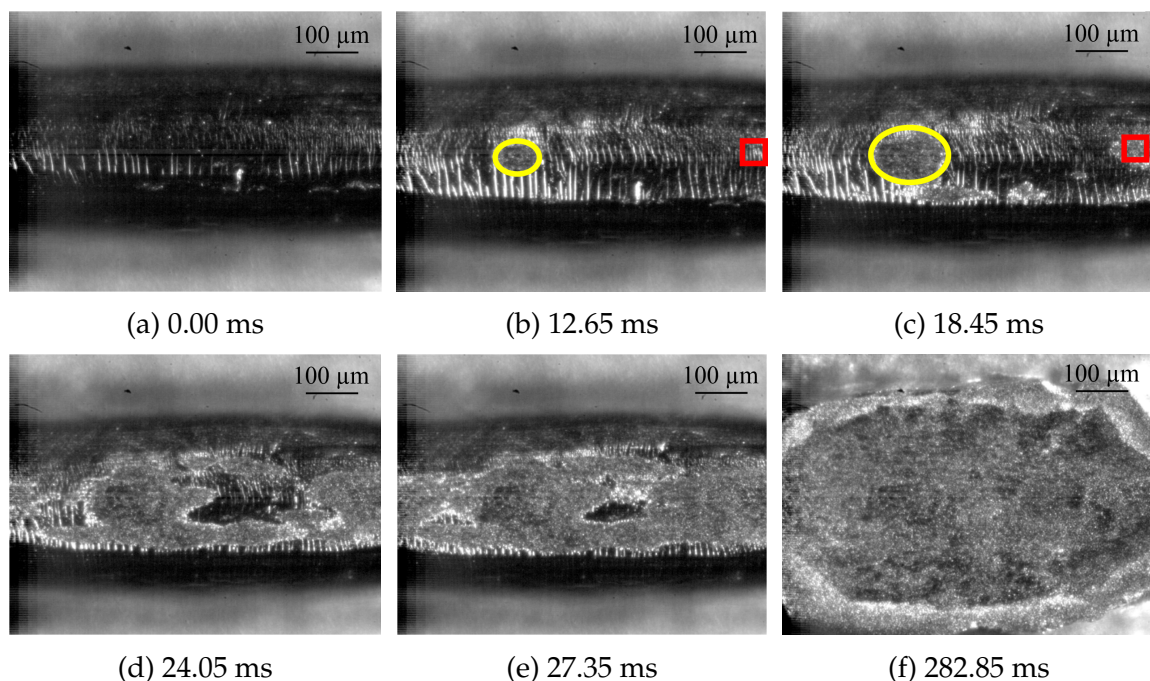


Fig. 5.24: The bonding interface with 50 nm Al_2O_3 on wire and 50 nm ZrO_2 on glass under 5 N, 1.4 W

In another test, a 50 nm ZrO_2 layer was deposited on both the wire and the glass. This process is similar to that shown in Fig. 5.24 except that no obvious cracks could be observed.

In general, all the oxide removal mechanisms except pushing were observed when oxides existed on both the wire and the substrate. Due to the influence of the oxides coated on the wire, pushing was not observed. This does not necessarily speak against the existence of the pushing mechanism.

When a 50 nm oxide layer was coated on both the wire and the substrate, the bonding strength was still enhanced compared to that of non-coated wire bonds. All the bonds

under 5 N, 2.5 W have a shear force larger than 12 N.

5.3.3.3 Validation by copper wire on glass

The case of copper-glass bonding was also tested. Compared to Al_2O_3 , the stiffness of the copper oxide is much smaller (less than one tenth of that of Al_2O_3). Furthermore, the copper oxide increases as long as the copper wire is exposed to air. Therefore, the thickness of the copper oxide is much higher than that of Al_2O_3 . Because of the stiffness and thickness, it is much harder to remove the copper oxides from the bonding interface. In this work, different parameters in a large window (up to 12 N normal force, up to 35 W US power and up to 6 s process time) have been tested for copper-glass bonding. No successful bonds could be made.

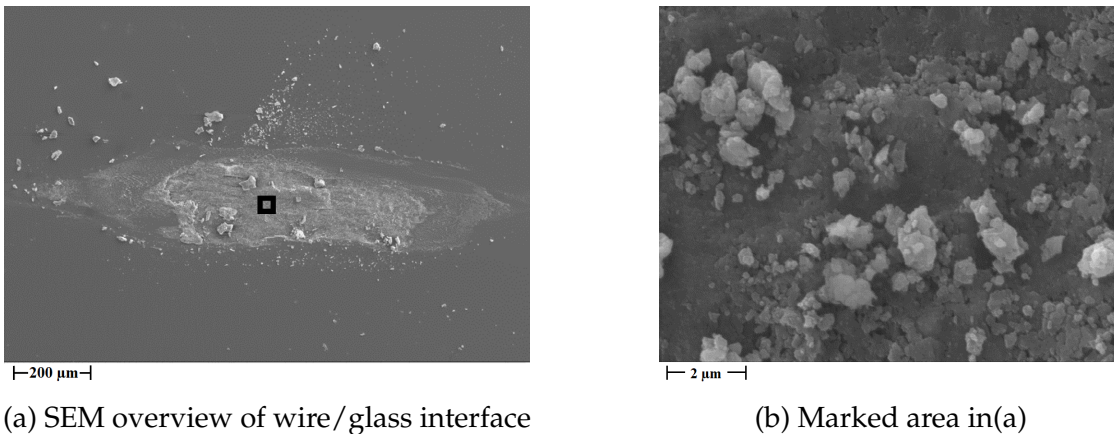


Fig. 5.25: The Cu wire/glass interface under 12 N, 32.3 W and 400 ms

Even though the copper-glass bonding did not succeed, some phenomena could still be observed. Due to the greater stiffness of copper in comparison with aluminum, the contact area was smaller under the same normal force. In addition, the expansion of the contact area was slower compared to that of the Al bonding processes. The detachment and milling of oxides were clearly observed. However, no penetration occurred because of the large thickness of the oxide layer. In contrast, the transportation of oxide particles due to oxide flow became more prominent. At the same time, the glass was worn and some glass particles were transported to the outside of the contact. The worn glass and particles (both oxide and glass particles) could also be observed by SEM. As shown in **Fig. 5.25** (a), the glass surface within the bonding footprint was worn and particles distributed on the whole interface. Due to the large normal stress, the central area was seriously abraded as in **Fig. 5.25** (b). The distributed oxide particles support the hypothesis of the detachment and milling of oxides as well as oxide flow. Therefore, the mechanisms including detachment, milling and oxide flow can be considered to be of importance for US wire bonding.

5.3.3.4 Validation by micro-particles

A layer of micro-particles was placed on the glass substrate to validate the removal mechanisms. The purpose of using particles was to track their positions during the removal process. In order to do this, the particles must be larger than the resolution of the high-speed observation system ($1.1 \mu\text{m}/\text{pixel}$). In addition, they must have a high strength so that they are not broken into smaller particles which are not trackable. Finally, three different materials including mono-diamond, poly-diamond and Silicon carbide (SiC) with two different sizes of $10\sim 20 \mu\text{m}$ and $2\sim 4 \mu\text{m}$ were selected. Since the resulting processes for the three materials are similar to each other, only the bonding processes with mono-diamond particles are described in this section.

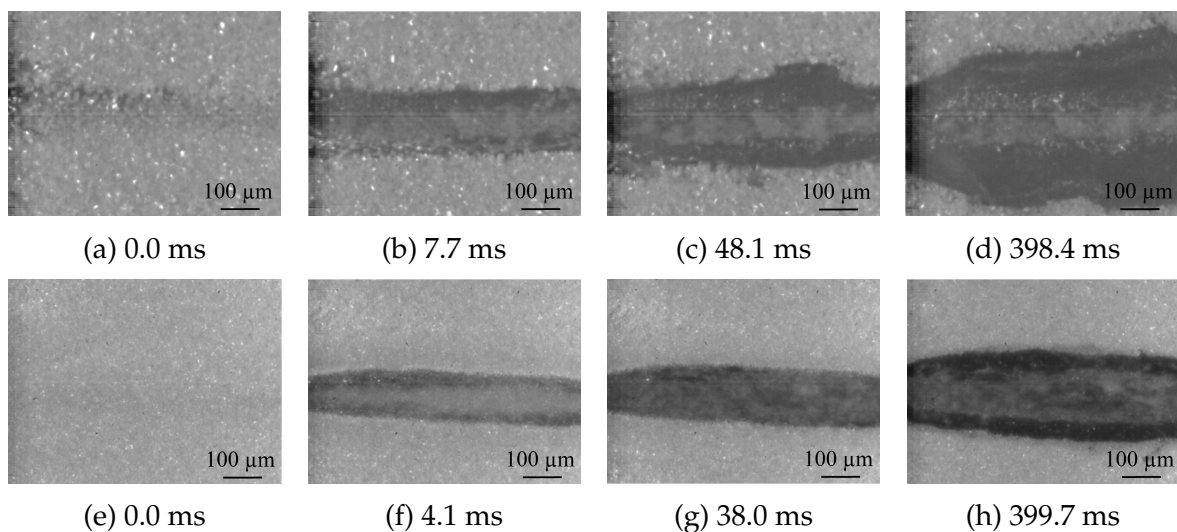


Fig. 5.26: (a)-(d) Wire/substrate interface with a layer of $10\text{-}20 \mu\text{m}$ mono-diamond particles under 5 N, 3.3 W; (e)-(h) Wire/substrate interface with a layer of $2\text{-}4 \mu\text{m}$ mono-diamond particles under 5 N, 4.9 W

For the bonding process shown in **Fig. 5.26** (a) to (d), a $40 \mu\text{m}$ thick layer of $10\text{-}20 \mu\text{m}$ mono-diamond particles was added into the interface. For the process in **Fig. 5.26** (e) to (h), a $200 \mu\text{m}$ thick layer of $2\text{-}4 \mu\text{m}$ mono-diamond particles was added. After the normal force loading, some areas of the wire were exposed in (a) while no wire was exposed in (e). This was due to the different thicknesses of the particle layer. As the particle layer was thicker, it became harder to penetrate the particle layer using the normal force itself.

As the vibration started, a clear wire penetration through the particle layer was observed for both conditions. As shown in **Fig. 5.26** (b) and (f), some wire was exposed to the glass substrate. In the meantime, the particles within the initial contact region were embedded into the surface of the wire. Afterwards, the contact area started to expand due to the continuous plastic deformation. As can be seen from (b) to (d) and from (f) to (h), the particles outside of the initial contact area remained outside of the contact area throughout the whole bonding process. No particles invaded the interface. This is similar to the pushing mechanism by material flow.

During these processes, both penetration and pushing mechanisms were observed. It was also shown that the pushing mechanism was effective on removing the contaminants located on the substrate and outside of the initial contact area.

5.3.4 Summary of the oxide removal process

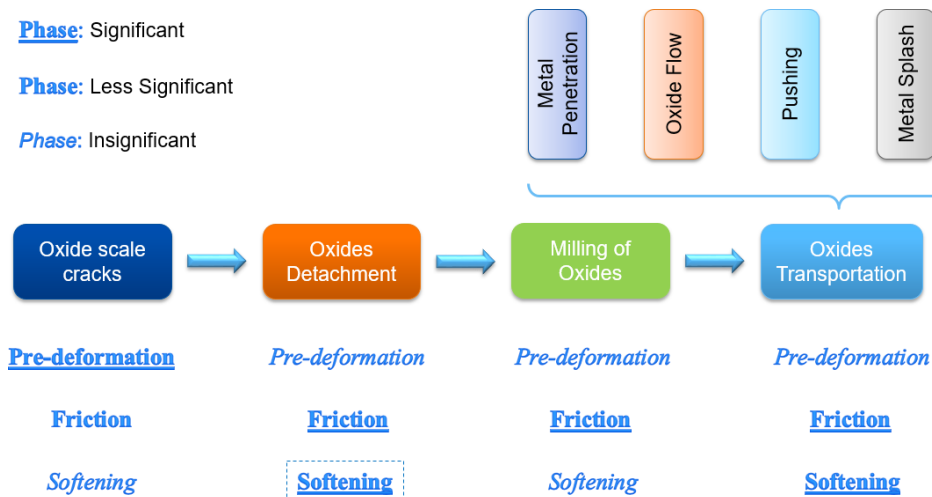


Fig. 5.27: Oxide removal process with the significance of corresponding phases

Based on the above findings and validations, the oxide removal process can be further described as in Fig. 5.27. As shown in the upper-left corner of the figure, the significance of the phases on the corresponding steps is represented by their font style. Compared to the process in Fig. 2.10, the milling of oxides is now included. The four mechanisms including metal penetration, oxide flow, pushing and metal splash are taken into account for oxides transportation. The effects of the three phases on each step become clearer. The normal force induced pre-deformation mainly causes the cracks of the oxide scale. Friction increases the intensity of cracks and thus plays the second most significant role on this step. Softening is insignificant in this step since cracking has finished before evident expansion of the contact area. Softening facilitates the extension of cracks only when the oxide layer is very thick, e.g. 200 nm. No oxides detachment was observed during the pre-deformation stage. The detachment was mainly caused by friction after the activation of US vibration. Softening induced material flow becomes significant to the detachment when oxides exist on the substrate. After the detachment, the oxide flakes are milled into small particles by the vibration induced relative motion. Pre-deformation and softening is insignificant to the milling process. The small particles are then transported to the peripheral region or to the outside of the contact area.

The oxides transportation is caused by both friction and softening. In the meantime, the effect of normal stress must not be ignored. Under the normal stress and vibration, penetration and oxide flow take place and have a significant impact on the oxides transportation. Pushing becomes significant when oxides or contaminants exist on the substrate. However, if they are within the initial contact area, pushing is not effective and the re-

removal is solely achieved by penetration and oxide flow. When metal splash occurs, oxides flow can be greatly enhanced.

5.4 Oxide particles

As mentioned in Section 5.3.2, most oxides piled up at the boundary of the contact area. It is hard to count the precise number and to evaluate the exact sizes of these particles. In this section, the coated wire bonding process from a side view is described. Oxide particles were emitted from the wire/tool interface and then fell down on the wire and the substrate. Since the fallen particles on the wire were discretely distributed, individual particles could be observed. Therefore, more information on the oxide particles was revealed.

5.4.1 Real-time observation of flying particles

The same setup as in Chapter 4 was used to observe the coated wire bonding process from a side view. In addition to the relative motion, emission of oxide particles could be clearly observed. A typical particle emission process with a 50 nm Al_2O_3 coated wire is shown in Fig. 5.28.

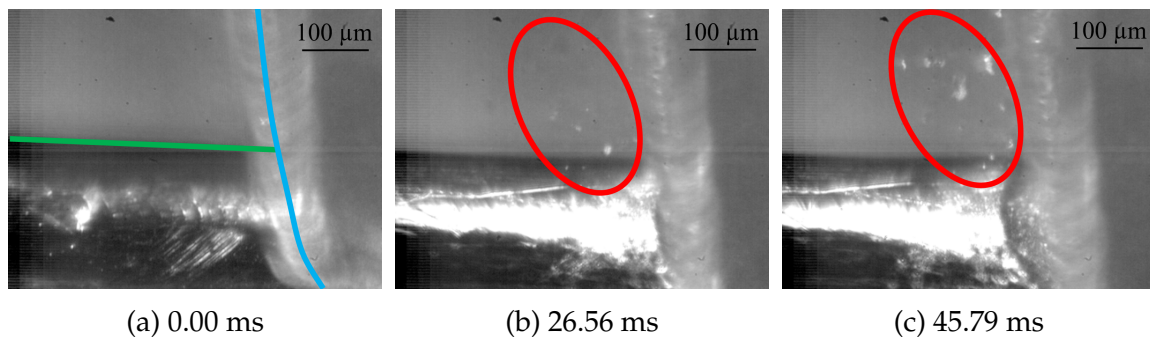


Fig. 5.28: The bonding process with a 50 nm Al_2O_3 coated wire under 6 N, 27.5 W

In Fig. 5.28 (a), the blue curve marks the edge of the bonding tool while the green line indicates the upper edge of the wire. From ~ 6 ms, continuous emission of flying particles occurred and lasted until the end of the bonding process. Two frames at the process time of 26.56 ms and 45.79 ms are shown in Fig. 5.28 (b) and (c), respectively. Many particles were emitted to the position within the red ellipse and exhibited different sizes. Furthermore, the initial speed of the flying particles was estimated from the video. The value (~ 0.34 m/s) is more than 100 times higher than that of the continuous plastic deformation. This indicates that vibration plays a significant role on the contaminants transportation at the wire/tool interface. Since the flying particles can be only observed when coated wire is used, it is supposed that they are the oxides from the coating layer. This will be later verified by SEM. During the flying period, the particles rotated and showed

their different facets. Some particles were found to be in the form of flakes. The bonding processes with a 50 nm ZrO_2 coated wire were also recorded by the real-time observation system. Similar processes for the emission of oxide particles were observed.

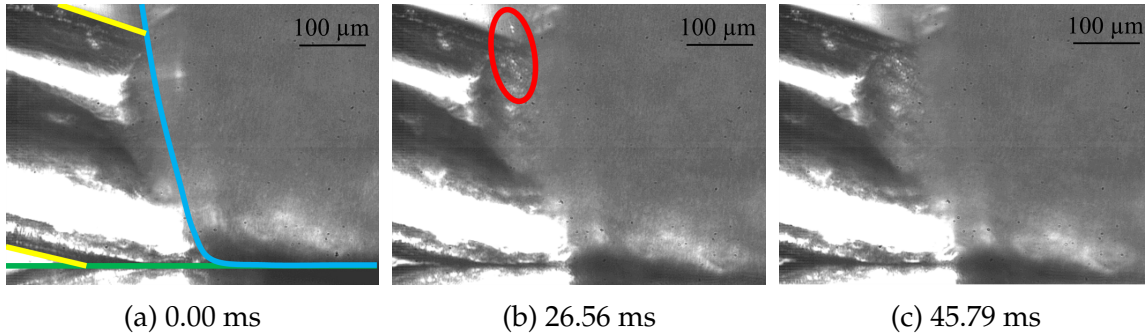


Fig. 5.29: The bonding process with uncoated wire under 9 N, 25 W

As mentioned before, flying particles were rarely observed during uncoated wire bonding processes. When a bonding process finishes, however, most oxides have been transported to the peripheral region as shown in Section 4.5.2. If the US vibration continues, these oxides can also be emitted to the outside. An example is given in Fig. 5.29. The contours of the tool, wire and substrate are marked with a blue curve and green and yellow lines in (a), respectively. Due to the large normal force and high US power, the tool touched the substrate at 21.16 ms, as shown in (a). After this time, particles started to be emitted to the outside of the contact. The flying particles at 31.06 ms are shown in the red ellipse of (b). The emission stopped at ~ 43 ms. Therefore, no flying particles were observed in (c). Due to the limited amount of natural oxides, fewer flying particles were emitted and the emission lasted for a shorter time than that of the coated bonding processes.

5.4.2 SEM observation

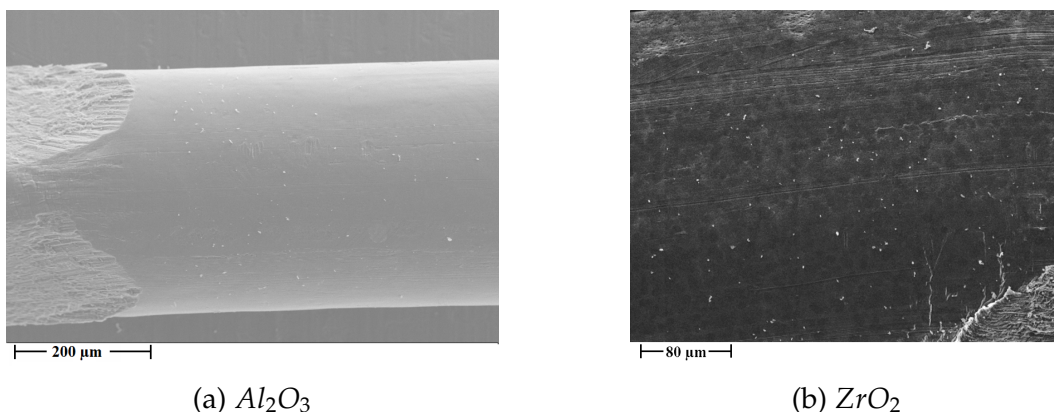


Fig. 5.30: Particles on the wire

After the emission, some particles fell down on the wire and the substrate. The fallen particles on an Al_2O_3 coated wire and a ZrO_2 coated wire are shown in Fig. 5.30 (a) and (b), respectively. With an EDAX analysis, most particles in the images were identified as

oxides. In both images, the oxide particles are discretely distributed on the wire surface. Some particles were emitted to a distant location (> 1 mm), which indicates the high self-cleaning capability of the bonding process. The areas of these particles were counted. It was found that most of the particles have a cross-sectional area of $1\sim 2 \mu\text{m}^2$.

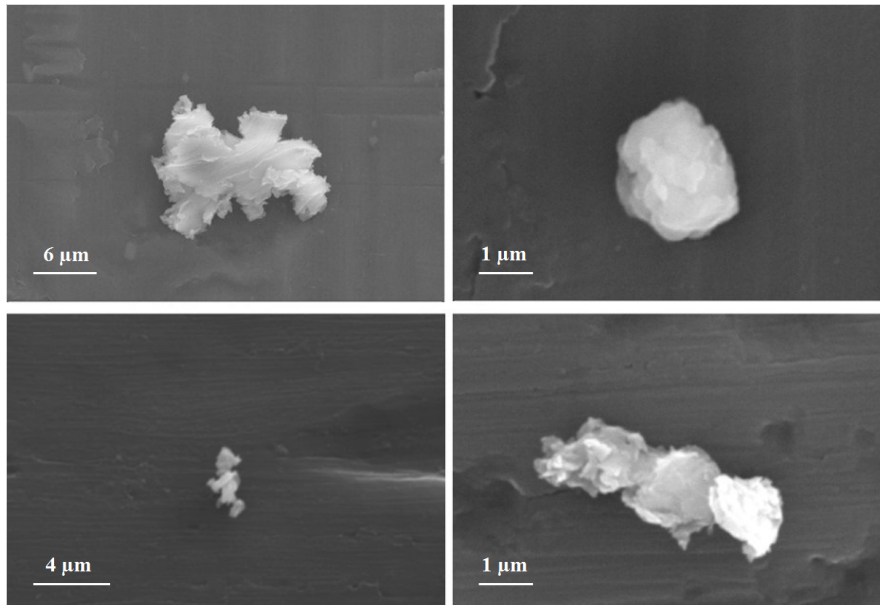


Fig. 5.31: Different oxide particles after the bonding process

Closer SEM observations showed that the oxide particles differ in shape and size from each other. Some particles are magnified and shown in **Fig. 5.31**. The particle in (a) has a length of $20 \mu\text{m}$ at its largest dimension. Furthermore, it has a complex structure in which many smaller particles are interconnected. (b) shows a ball-like particle with a diameter of $2 \mu\text{m}$. The different brightnesses on the particle suggest that it was formed by stacking a few layers of oxide flakes. The particles in (c) and (d) appear to consist of three or four smaller particles which adhere together. In one word, it is indicated that the formation of these particles was due to agglomeration. During the transportation of oxides from the central region to the peripheral region, the "inner" oxide particles met with or crashed into other oxide particles. Some of the particles were pushed away and some agglomerated together with the original inner oxide particles. Finally, the inner oxide particles grew into larger ones.

5.5 Conclusion

The bonding process was first investigated in this chapter via real-time observation of the wire/glass interface. During the bonding process, five different areas including contact area, friction area, stick area, oxides area and microwelds area emerge and vary. The contact area is caused by the loading of the normal force. After the activation of US vibration, the friction area appears and expands together with the contact area. In the meantime, oxides are removed. As microwelds are able to constrain the motion of a part of the wire,

the corresponding area begins to stick on the substrate. As more microwelds form, this stick area expands. Not all oxides can be removed from the stick area. Therefore, the stick area consists of the microwelds area and oxides area. The impacts of the process parameters on the different areas were also studied. To remove more oxides and obtain a large microwelds area, the normal force and the US power must be well combined.

The oxide removal process was further analyzed by the coated bonding processes. It consists of four steps including the occurrence of cracks, the detachment of the discretized oxides, the milling of these oxides into small particles and the transportation of these particles to the peripheral region. Four mechanisms drive the transportation of the oxide particles: metal penetration, oxide flow, pushing and metal splash. Metal penetration and oxide flow play the most significant role in the transportation process. During the transportation process, some oxide particles agglomerate together into larger particles. In addition, it was found that a 50 nm oxide coating on either the wire or the glass can enhance the bonding strength.

6 Energy flow

Based on the measurements and the knowledge obtained in the previous chapters, the energy flow as described in Chapter 2 can now be quantified. It is quite difficult to give a general description that is valid for all parameter combinations. As a first step towards such a general model of the energy flow, in this chapter the process with 7.5 N, 17.5 W is used as a reference. The energy flow of the process is calculated based on the information gathered in Chapter 4 where this case was studied in detail. The aim is to give a specific example for the energy flow chart of **Fig. 6.1** with specific values on the arrows. The quantification for processes with different parameter settings is discussed as well. The energy flow helps to achieve a quantitative understanding of the complicated bonding mechanisms and the enhancement of the bonding quality. Some contents of this chapter have been published in [128].

6.1 Simplification

Some processes require only little amount of energy and it is straightforward to conclude that they are not significant to the bonding process. Such items are marked in gray in **Fig. 6.1**.

As with the wire/substrate interface, the wire asperities at the wire/tool interface are plastically deformed. The formation and breakage of microwelds occur at the wire/tool interface as well. The energy required for these changes, however, is negligible. The reasons for this are as follows. Firstly, the energy for the bulk deformation of the wire is more than three orders higher than that for the asperities deformation at the two interfaces. Therefore, the energy from the vertical motion of the tool is mainly consumed by the bulk deformation of the wire. Only a much smaller and negligible part goes into asperities deformation. Secondly, due to the material of the tool, the connection between the tool and the wire is very weak, which has no significant influence on the process at the wire/substrate interface. Thus only a small amount of energy is required to form such a weak connection. Finally, the very small amount of energy for "Asperities Deformation + Microwelds Formation & Breakage" at the wire/tool interface are neglected.

Due to the friction and the formation of microwelds at the wire/substrate interface, the substrate also vibrates. The vibration and the normal force further lead to the deforma-

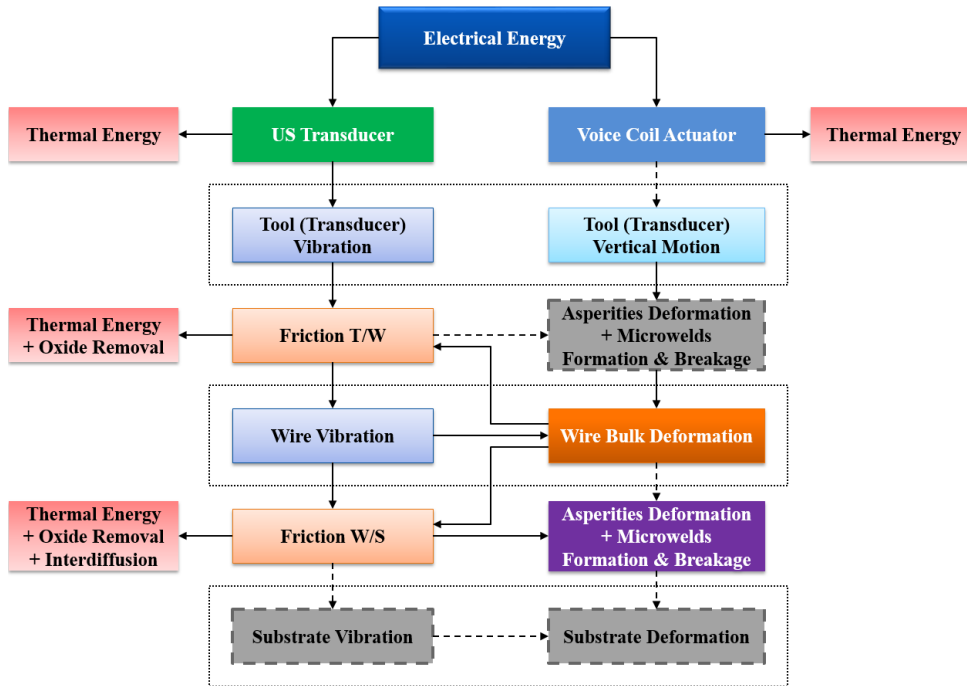


Fig. 6.1: The simplification of the energy flow

tion of the substrate material. Under normal conditions, however, both the vibration amplitude and the deformation depth are in the range of nanometers. Therefore, they are considered to be insignificant to the bonding process and the corresponding energy flows are not considered.

6.2 Quantification of energies

6.2.1 Energy of the transducer

Assuming that at the initial time $t = 0$, the transducer is in its equilibrium state with $u = 0$, the electrical input energy to the transducer can be easily calculated by the measured voltage and current:

$$E_{tran-input}(t) = \int_0^t u(t)i(t)dt \quad (6.1)$$

where $u(t)$ and $i(t)$ are the instantaneous voltage and current at the process time t , respectively. Both the voltage and the current have the same frequency which is tuned to the eigenfrequency of the transducer - 59.95 kHz. Their instantaneous values were measured by a Tektronik 3014 oscilloscope with a sampling rate of 50 MS/s.

Some of the energy is lost in the electro-mechanical energy conversion and in the energy transfer to the tool. An equivalent electric model of the transducer (including the tool) is shown in Fig. 6.2. $Z_{Process}$ is the impedance of the process. It is expressed as a function

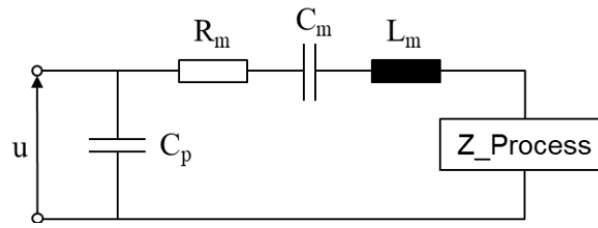


Fig. 6.2: An equivalent electric model of the transducer

of the generalized mechanical coordinates of transducer and tool to the eigenmode which is used for operation. As described in Chapter 4, the transducer is always driven at its resonance, which is a consequence of the phase-locked-loop control. Therefore, the electrical energy is only consumed at R_m and $Z_Process$ and the current to C_p can be neglected. The energy consumed at R_m (14.45Ω) is converted into thermal energy and radiated into the environment. It can be calculated as

$$E_{tran-loss}(t) = \int_0^t R_m i^2(t) dt \quad (6.2)$$

The storage energies at L_m (11.78 mH) and C_m (600.42 pF) are related to the vibration of the transducer and the tool. They are calculated as follows:

$$E_{tran-stor}(t) = E_L(t) + E_C(t) \quad (6.3)$$

$$E_{Lm-stor}(t) = \frac{1}{2} L_m i^2(t) \quad (6.4)$$

$$E_{Cm-stor}(t) = \frac{1}{2} \frac{q^2(t)}{C_m} \quad (6.5)$$

$$q(t) = \int_0^t i(t) dt \quad (6.6)$$

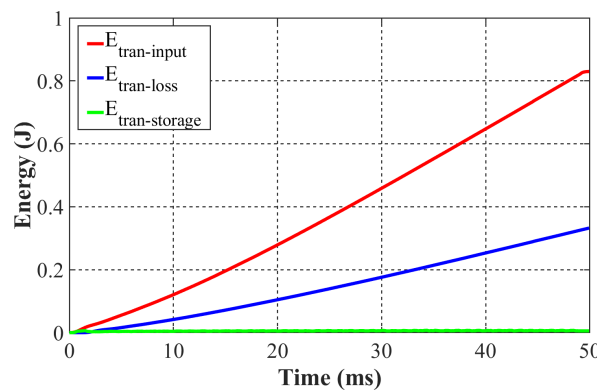


Fig. 6.3: The energy flow at the transducer during the process under 7.5 N, 17.5 W

The energy flows of the transducer for the process under 7.5 N, 17.5 W are shown in Fig. 6.3. The total input energy at the full process time is 0.8 J and only 59.56% of the energy was transferred to the bonding domain and the environment.

6.2.2 Energy of the voice coil actuator

The voice coil actuator can be considered an inductor L_{VCA} (3.47 mH) and a resistor R_{VCA} (20.09 Ω) in series. The energy consumption at the actuator can be calculated as

$$E_{VCA-loss}(t) = \int_0^t R_{VCA} i_{VCA}^2(t) dt \quad (6.7)$$

The storage energy of the actuator is dependent on the driven current i_{VCA} and is calculated:

$$E_{VCA-stor}(t) = \frac{1}{2} L_{VCA} i_{VCA}^2(t) \quad (6.8)$$

The energy from the voice coil actuator generates normal force and vertical displacement. The output energy of the actuator is:

$$E_{VCA-output} = \int_0^t F_N(t) dS_N(t) \quad (6.9)$$

where $F_N(t)$ is the normal force generated by the voice coil actuator and $S_N(t)$ is the vertical displacement of the tool tip at the process time t .

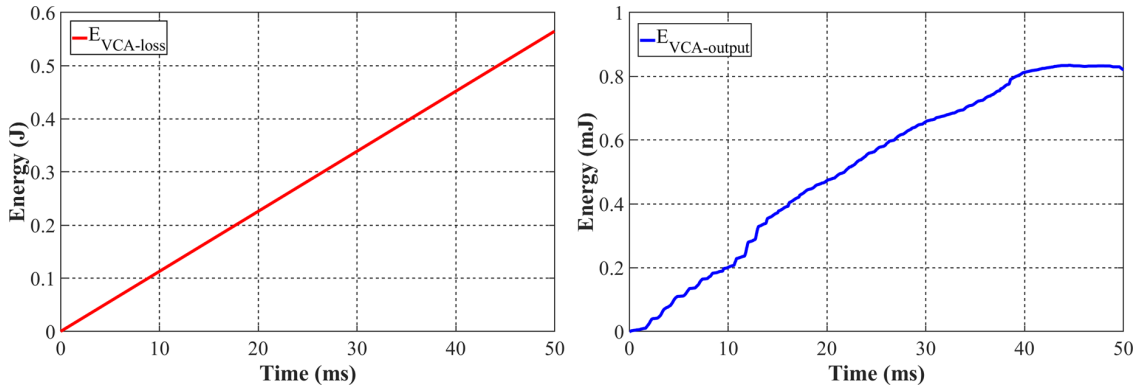


Fig. 6.4: The energy flow at the voice coil actuator during the process under 7.5 N, 17.5 W

Fig. 6.4 shows the energy flows at the voice coil actuator. It can be seen that most of the energy (99.75%) is consumed at the coils. Since the driven current was nearly the same during the bonding process, the storage energy also remained the same. Only 0.8199 mJ was used to keep the normal force at the desired value during the bonding process.

6.2.3 Friction energy

As explained in Chapter 4, both vibration and the plastic deformation induce friction at the wire/tool interface and at the wire/substrate interface. Therefore, the friction en-

ergy at each interface consists of two components - the vibration induced friction and the plastic deformation induced friction. In this section, the friction conditions at the two interfaces are first discussed and the energies are then calculated.

6.2.3.1 Cleaning coefficient

In Chapter 5, the cleaning coefficient during metal-glass bonding was identified via real-time observation. In the case of metal-metal bonding, however, the bonding interface becomes opaque and the cleaning coefficient during the bonding process cannot be directly measured. In this case, the cleaning coefficient is assessed by the microwelds area.

In general, the wire/substrate interface can be divided into an oxide-metal area and an oxide-free area. The latter is indicated by microwelds. The cleaning coefficient φ is defined as:

$$\varphi(t) = \frac{A_{mw}(t)}{A_{cont}(t)} \quad (6.10)$$

where $A_{mw}(t)$ and $A_{cont}(t)$ are the microwelds area and the contact area at the process time t , respectively.

As stated in Chapter 2, the microwelds area can be indirectly estimated by real-time contact resistance measurement. According to [35], the microwelds start to form after 2~5 ms and then increase linearly with time. In this work, the starting time of microweld formation is set at 3.5 ms for all the processes. Even though it varies slightly when the parameters are changed, this can be ignored since the range is small compared to the whole process time. The only unknown now is the final value of the cleaning coefficient.

As discussed in Chapter 2 and Chapter 5, the metal residues after shear tests are not exactly equal to the microwelds area. Instead of counting the metal residues, the final microwelds area is calculated as:

$$A_{mw-final} = \frac{F_{shear}}{\sigma_{y-mw}} \quad (6.11)$$

where F_{shear} is the shear force of a bond and σ_{y-mw} is the ultimate shear stress of microwelds. The shear forces were directly measured by shear tests and are shown in **Table 4.3**. The ultimate shear stress of 99.999% aluminum is about 50 MPa according to [?]. Due to the change of the defect density within the crystals, the recrystallization and recovery, the ultimate shear stress might differ after the bonding process. The nominal shear stress of the aluminum bonds for all the processes can be calculated based on **Table 4.3**. The largest nominal stress is 58.31 MPa obtained from the 7.5 N, 17.5 W specimens. Since this value exceeds the reference value by 16.62%, it is considered as the ultimate shear stress after the bonding process. The final cleaning coefficient for the 7.5 N, 17.5 W process is

assumed to be 1. The final interface of a 7.5 N, 17.5 W specimen after the shear test and the corresponding cleaning coefficient curve are shown in Fig. 6.5 (a) and (b), respectively.

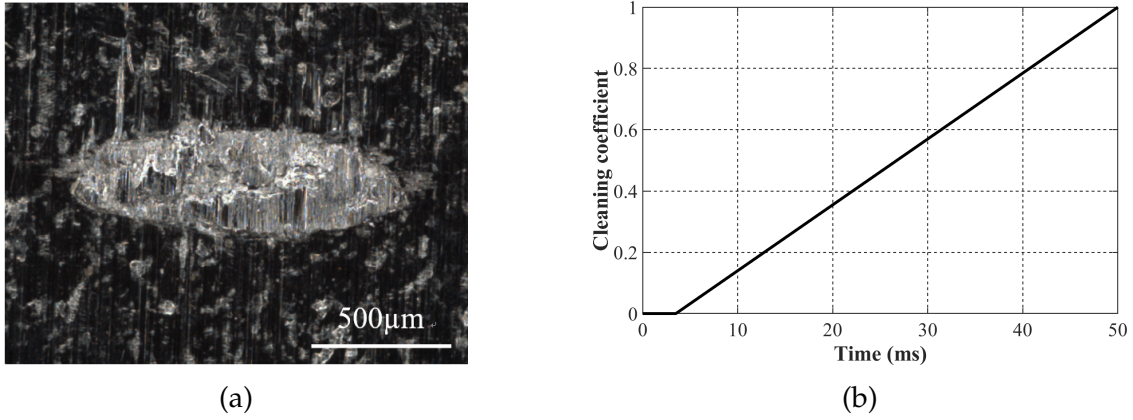


Fig. 6.5: (a) The final interface (b) cleaning coefficient of the process under 7.5 N, 17.5 W

Since nearly no microwelds form at the wire/tool interface, the friction coefficient at this interface is considered to be a constant value for tungsten carbide-aluminum contact.

6.2.3.2 Friction energy due to vibration

The energy for the vibration induced friction can be calculated by Coulomb's Law as follows:

$$E_{v\text{-friction},w/t}^{up\text{-limit}}(t) = \int_0^t \mu_{w/t} F_N(t) dD_{v,w/t}(t) \quad (6.12)$$

$$E_{v\text{-friction},w/s}^{up\text{-limit}}(t) = \int_0^t \mu_{w/s} (1 - \varphi(t)) F_N(t) dD_{v,w/s}(t) \quad (6.13)$$

where μ is the friction coefficient for the corresponding sliding interface; $D_v(t)$ is the total distance accumulated by the vibration induced relative displacement at the corresponding interface at the process time t . As discussed in last section, the wire/substrate interface at the process time t can be divided into metal-oxide area and microwelds area (oxide-free area). Since there is no friction in the microwelds area, a coefficient of $1 - \varphi(t)$ is introduced into Equation. 6.13 in order to calculate the friction energy at the wire/substrate interface. Due to the unevenly distributed normal stress and microwelds, the relative displacement amplitudes at different locations of the interface are different, which were shown in both Chapter 4 and Chapter 5. The relative displacements used for this calculation are derived from the high-speed videos in Chapter 4 where the largest relative displacement amplitude was captured. Therefore, only the upper limit of this energy can be calculated. The energy for microwelds formation and breakage will be discussed later.

The friction coefficient between the tool and the wire was measured by the detection of the dragging force of the wire which was pressed by the tool. The average of the mea-

surements is 0.915 ± 0.098 . The metal-oxide contact for Al-Al bonding is considered to be an alumina-alumina contact. According to [138], the friction coefficient for an alumina-alumina contact, i.e. $\mu_{w/s}$, is taken as 0.41.

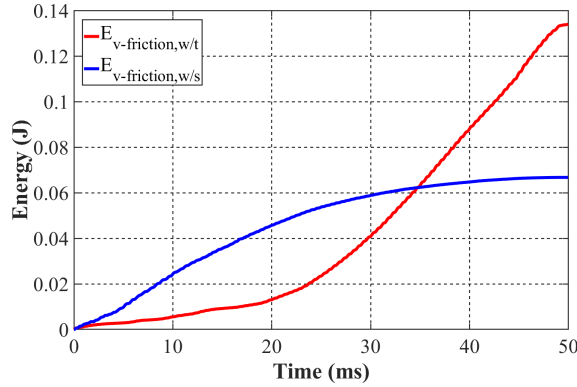


Fig. 6.6: The vibration induced friction energy at two interfaces

The results for the vibration induced friction energy at the two interfaces are shown in Fig. 6.6. After a rapid increase during the beginning stage, the increment of the friction energy at the wire/substrate interface becomes slower. This is due to the decreased relative displacement amplitude and the reduced oxide-metal contact area. At the same time, the enlarged relative displacement amplitude at the wire/tool interface makes the increment of $E_{v\text{-friction},w/t}$ faster in the later stage. Nevertheless, the vibration induced friction energies at both interfaces makes up a significant part of the total input energy to the bonding domain. They thus play essential roles in the bonding process.

6.2.3.3 Friction energy due to plastic deformation

The plastic deformation induced friction energies are:

$$E_{p\text{-friction},w/t}^{up\text{-limit}}(t) = \int_0^t \mu_{w/t} F_N(t) dS_{p,w/t}(t) \quad (6.14)$$

$$E_{p\text{-friction},w/s}^{up\text{-limit}}(t) = \int_0^t \mu_{w/s} (1 - \varphi(t)) F_N(t) dS_{p,w/s}(t) \quad (6.15)$$

where $S_p(t)$ is the largest plastic deformation induced relative displacement at the corresponding interface. The plastic deformation induced relative displacements vary at different parts of the wire. The longer the distance from the center of the wire is, the larger this relative displacement is. In Chapter 4, only the largest plastic deformation induced relative displacements were measured. Since it is extremely difficult to predict the plastic deformation induced relative displacement in the other areas, it is not possible to calculate the average relative displacement of the wire induced by plastic deformation. As a result, only the upper limits of the plastic deformation induced friction energies can be calculated. The resulted values are very small, which is in the order of 10^{-4} (J). This is easy to understand as the displacement induced by the plastic deformation

is in the micron range while the accumulation of the vibration induced displacement is in the meter range. Since the consumed energies are even smaller than these upper limit values, the plastic deformation induced friction energies are not further analyzed.

6.2.4 Kinetic energy of wire vibration

As detected in the real-time observation, the wire vibrates during the bonding process. The kinetic energy for wire vibration is:

$$E_{v-wire}(t) = \int_0^t \frac{1}{2}mv^2(t)dt \quad (6.16)$$

where m is the mass of the wire underneath the tool tip and is calculated to be ~ 0.379 mg; $v(t)$ is the vibration speed of the wire at the process time t .

Since the mass is very small, the calculated vibration energy (5.8×10^{-5} J) is in the order of 10 to the power of -5. Therefore, this energy is also neglected.

6.2.5 Energy for APE

The energy for the wire bulk deformation comes from the work of the normal force and the US energy which goes into APE. The energy obtained from the work of the normal force is:

$$E_{NF-defor,wire}(t) = E_{VCA-output}(t) - E_{p-friction,w/t}(t) - E_{p-friction,w/s}(t) - E_{p-mw}(t) \quad (6.17)$$

where E_{p-mw} is the energy consumed for plastic deformation induced microwelds formation. This energy will be discussed in the following section.

It is currently impossible to directly calculate the APE energy, as the mechanism is still unknown. In this work, an equivalent work to deform the wire is used to estimate the APE energy. The equivalent work is calculated as:

$$W_{defor,wire}(t) = \int_0^t F_{add,N}(t)dS_N(t) - E_{add-p-friction,w/s}(t) - E_{add-p-friction,w/t}(t) \quad (6.18)$$

$$E_{add-p-friction,w/t}^{up-limit}(t) = \int_0^t \mu_{w/t}F_{add,N}(t)dS_{p,w/t}(t) \quad (6.19)$$

$$E_{add-p-friction,w/s}^{up-limit}(t) = \int_0^t \mu_{w/s}F_{add,N}(t)dS_{p,w/s}(t) \quad (6.20)$$

where $F_{add,N}(t)$ is the additional normal force required to deform the wire with a normal displacement $S_N(t)$ when no US energy is applied; $E_{add-p-friction}(t)$ is the additional friction energy which is caused by additional normal force induced plastic deformation. As with the plastic deformation induced friction energy, only the upper limit of $E_{add-p-friction}$ can be calculated. During the additional force test, no US vibration was applied.

As mentioned above, there are two energy inputs to the bulk deformation of the wire. The equivalent work can be also expressed as:

$$W_{defor,wire}(t) = E_{NF-defor,wire} + E_{APE}(t) \quad (6.21)$$

Then the energy flowing into APE is:

$$E_{APE}(t) = W_{defor,wire}(t) - E_{NF-defor,wire}(t) \quad (6.22)$$

When $E_{p-friction}$ and $E_{addpfriction}$ take half the value of their upper limits, the total energy flowing into APE is calculated to be 0.4899 mJ. This is 4.95 times higher than the work done by the normal force during pre-deformation stage. From this point of view, continuous plastic deformation takes place when US vibration is superimposed. Nevertheless, this energy is not considered due to its small value.

6.2.6 Energy for microwelds formation and breakage

As already mentioned, highly dynamic changes in microwelds including formation, deformation and breakage, occur at the bonding interface. The changes also differ at different locations of the interface. As a result, it is extremely hard to directly calculate the energy required for these changes. In this work, the energy for microwelds changes is estimated as an equivalent friction energy at the wire/substrate interface within the oxide-free area. As with the relative motions, the equivalent energy consists of two parts: the vibration induced friction and the plastic deformation induced friction:

$$E_{v-mw}^{up-limit}(t) = \int_0^t \mu_{mw} \varphi(t) F_N(t) dD_{v,w/s}(t) \quad (6.23)$$

$$E_{p-mw}^{up-limit}(t) = \int_0^t \mu_{mw} \varphi(t) F_N(t) dS_{p,w/s}(t) \quad (6.24)$$

where μ_{mw} is the equivalent friction coefficient for microwelds formation, deformation and breakage. The value of μ_{mw} shall be higher than that for Al-Al (metal-metal) contact and smaller than the value which is equivalent for the breakage of all microwelds. As

discussed in Section 6.2.3.1, the whole wire/substrate interface for the 7.5 N, 17.5 W process is considered to be bonded. The equivalent friction coefficient for the breakage of all microwelds is thus calculated as the ratio of shear force over normal force. The resulting coefficient is 2.63. The friction coefficient for metal-metal contact of aluminum is 0.865, as referred from [138,139]. The equivalent coefficient μ_{mw} must be a value between 0.865 and 2.63. To estimate the energy, an average value of 1.748 is selected.

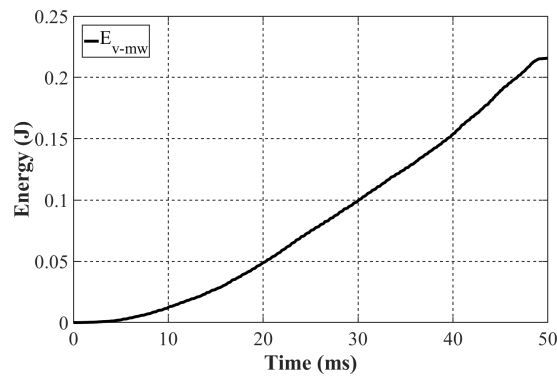


Fig. 6.7: Equivalent energy for microwelds formation, deformation and breakage

The energy for vibration induced microwelds formation, deformation and breakage is shown in Fig. 6.7. It takes the largest part of the energy from the transducer. The energy for plastic deformation induced microwelds formation, deformation and breakage is in the range of 10^{-4} (J). It is thus not further considered.

6.2.7 Energy emitted into the environment

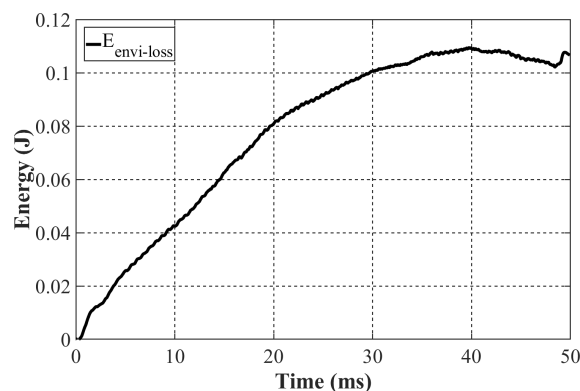


Fig. 6.8: Energy emitted into the environment

There is still a certain amount of energy which is emitted into the environment, including the substrate, the non-contacted part of the wire and the ambient space. This energy can be obtained by subtracting the energy mentioned above (related with vibration) from the total energy of the transducer. The result is shown in Fig. 6.8. Finally, about 0.11 J was emitted into the environment.

6.3 Global energy flow

Based on the calculation of the individual energy flows, a global map of the energy flows can be drawn. The main energy flows from the transducer along with the processing time is summed up in **Fig. 6.9**. It is obvious that the main output energy of the transducer flows into three parts: the vibration induced friction at the wire/tool interface, the vibration induced friction at the wire/substrate interface and the microwelds formation, deformation and breakage. The vibration induced friction energy at the wire/substrate interface finally reaches a constant level. The other energy flows keep increasing through the whole process. A small part of the energy was stored in the transducer and the energy loss of the transducer is comparably large.

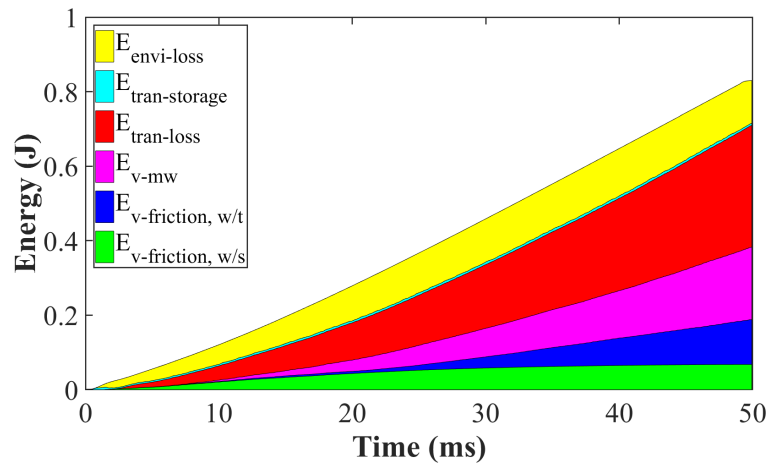


Fig. 6.9: Energy flow from transducer through the bonding process under 7.5 N, 17.5 W

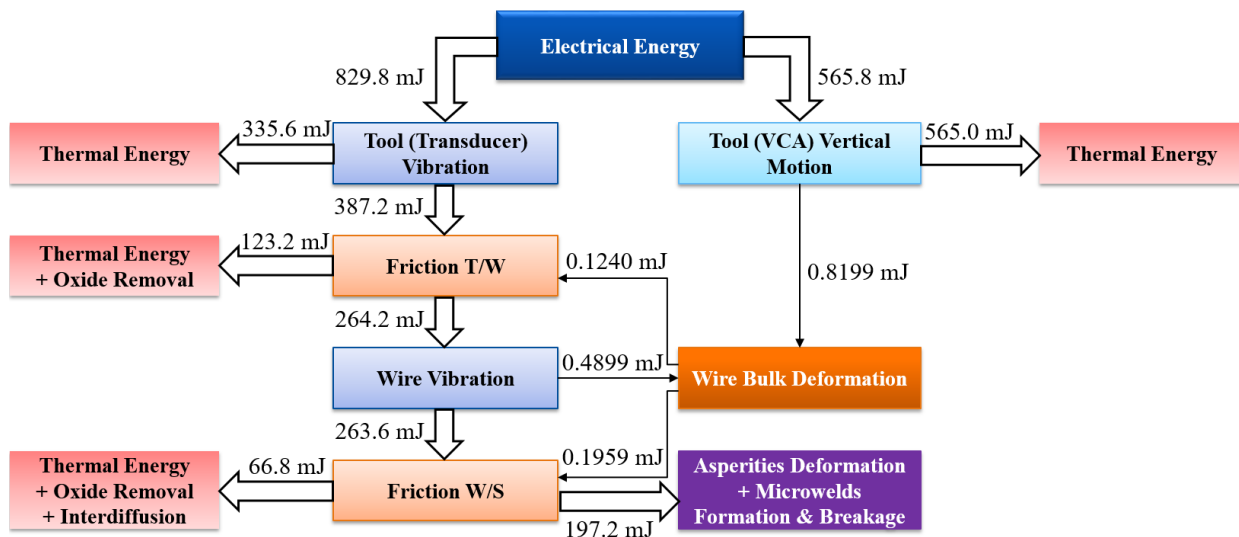


Fig. 6.10: Quantification of the energy flow at the process time of 50 ms under 7.5 N, 17.5 W

To explain the energy flow in more detail, the corresponding energies at the process time of 50 ms are filled on the arrows of the energy flow chart and shown in **Fig. 6.10**. 40.50% of the total electrical energy was consumed at the voice coil actuator. 46.66% of the output

energy of the transducer went to the bonding domain and the surrounding environment. The energy flowing to APE is similar to the VCA energy flowing to the bulk deformation of the wire. This can explain the yield stress reduction of the wire material when US vibration is imposed. In total, the plastic deformation induced friction energy is only 0.074% of the vibration induced friction energy. Since 17.5 W is well matched with 7.5 N, 68.08% of the energy from the transducer can be guided to wire/substrate and 74.69% of that energy was used for the formation, deformation and breakage of microwelds.

6.4 Impact of process parameters

Table 6.1: Energy consumption (EC) at and total output energy (OE) from the voice coil actuator under different parameter settings

		US Power		
		12 W	17.5 W	23 W
6.0 N	EC	361.62 mJ	361.62 mJ	361.62 mJ
	OE	0.7265 mJ	0.7367 mJ	0.6697 mJ
7.5 N	EC	565.03 mJ	565.03 mJ	565.03 mJ
	OE	0.7991 mJ	0.8199 mJ	0.8575 mJ
9.0 N	EC	813.65 mJ	813.65 mJ	813.65 mJ
	OE	0.9147 mJ	1.3324 mJ	1.4699 mJ

The energy flows under the other 8 settings are calculated in order to study the impact of the process parameters. The energy consumption and the output energy of the voice coil actuator are first shown in **Table 6.1**. To obtain a larger normal force, more energy was consumed and the output energy significantly increased. As a higher US power usually led to a larger vertical displacement, more work was done by VCA. The only exception is the 6 N, 21.6 W process where the vertical displacement is small.

Table 6.2: Final cleaning coefficient under different parameter settings

		US Power		
		12 W	17.5 W	23 W
6.0 N		0.8075	0.8530	0.8768
7.5 N		0.8370	1.0000	0.8626
9.0 N		0.8195	0.8566	0.6873

To be able to calculate the energy flows from the transducer, the final cleaning coefficients in different processes must be quantified first. Using Equation. 6.10 and Equation. 6.11, the final cleaning coefficients for the other process are calculated and shown in **Table 6.2**. The 6 N processes obtained larger cleaning coefficients which are mainly due to the small contact areas. The 7.5 N processes have the highest values which indicate effective self-cleaning processes. As the contact areas increased for the 9 N processes, the values decreased.

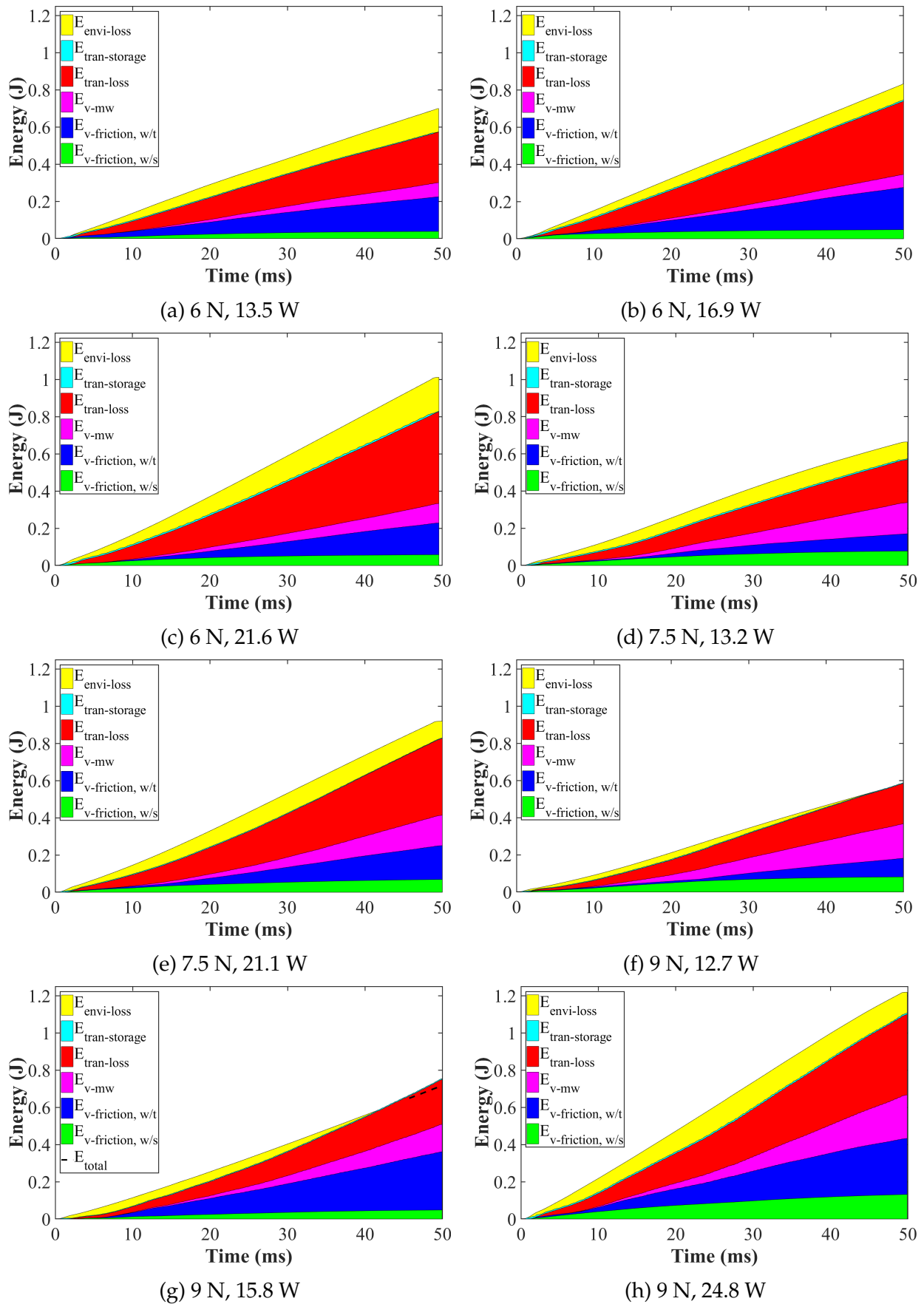


Fig. 6.11: Energy flow from the transducer during the other processes

The energy flows from the transducer during the other processes are shown in **Fig. 6.11**. In the case of (g), the sum of the calculated energy exceeded the input energy by 2.59%, as shown by the dash lines. Other than that, the sum of energies is lower than the total input energy. In general, the deviations in the calculations are acceptable.

The energy loss of the transducer greatly increased as the US power (or current) increased. The vibration induced friction energy at the wire/substrate interface increased as the normal force increased. The decrease of the energy by (g) was due to the initial change of the equilibrium position of the tool. The impact of US power on the vibration induced friction energy at the wire/substrate interface is greatly influenced by the various cleaning coefficients. For the vibration induced friction energy at the wire/tool interface, an increase in the US power usually caused an increase in this energy consumption. Compared to the process under 6 N and 9 N, less friction energy at the wire/tool interface was consumed for the 7.5 N processes.

When more energy was transferred to the wire/substrate interface, more energy also went to the formation, deformation and breakage of microwelds. This, however, does not necessarily indicate the achievement of a high bonding strength. For example, the shear strengths of (e) (h) are not high despite their large energy input into the formation, deformation and breakage of microwelds. It indicates that in these processes, more energy was used for the deformation and breakage of microwelds than for the formation of microwelds.

To conclude, a good match between the normal force and the US power provides a large percentage of the energy for microwelds formation. To obtain this, a mid-range of normal force and a mid-range of US power should be applied.

6.5 Conclusion

The energy flows from the voice coil actuator and the transducer to the bonding processes were quantified in this chapter. Most of the input energy to the voice coil actuator is consumed at the coils due to the large electrical resistance. The work done by the voice coil actuator is much smaller than the energy from the transducer. The main output energy of the transducer flows into the consumption at the transducer, the vibration induced friction energy consumption at the wire/tool interface, the vibration induced friction energy consumption at the wire/substrate interface and the formation, deformation and breakage of microwelds. The process parameters significantly affect the energy flows. A normal force and an US power in a mid-range are recommended to obtain a good composition of the energy flows, which means that a large amount of energy can be guided for microwelds formation.

7 Discussion on results

In the previous chapters, the relative motions at the two interfaces were analyzed and quantified by real-time observation; the oxide removal process was revealed by a transparent glass substrate and artificial coatings; finally, the energy flows during the bonding process were quantified. The results from these chapters are now discussed as the following:

The quantification of the relative motions at the two interfaces

In general, there are two methods which are commonly used to measure the amplitudes of the tool and the wire: real-time observation and laser vibrometer. Both methods have advantages and disadvantages. The real-time observation has normally a recording rate that is smaller than the bonding frequency and might cause under-sampling problems. On the other hand, more information can be recorded due to the large number of pixels in the recording window. The laser vibrometer is able to solve the sampling problem while the location of the laser beam is a new issue. As stated in Chapter 4, different motion routes exist at different vertical locations of the wire, especially for the plastic deformation induced motion. To perform the measurement with a laser vibrometer, the wire is normally cut, which could affect the accuracy of the measurement. In addition, it is hard to confirm that the laser beam is always focused on the same position for different wires. The accuracy might be further influenced if the size of the laser beam is relatively large. To compromise the features of the two methods, the bonding process was recorded with the real-time observation system and the obtained amplitudes were then validated with a laser vibrometer. The results showed that the real-time observation was capable to capture the peak values of the vibration.

The relative motion at both the wire/tool interface and the wire/substrate interface can be quantified by the real-time observations. In addition, the two components of the relative motion, the vibration induced relative motion and the continuous plastic deformation induced relative motion, can be separated. In general, the vibration induced relative motion at the wire/substrate interface gets smaller while the relative motion at the wire/tool interface gets larger as more microwelds form. The plastic deformation of the wire keeps increasing until the maximum is reached. On unexpected result is the change of the equilibrium position of the tool in the beginning stage. This takes place in all processes and the changes vary from process to process. The quantification of the relative motions at the

two interfaces provides the basis for the quantitative understanding of the mechanisms.

The oxide removal process

It is hard to analyze the oxide removal process since the interface is enclosed and the natural oxide layer on the aluminum wire is only 5 nm thick. To solve these problems, the metal substrate was substituted by a transparent glass and an artificial oxide coating was deposited on some specimens. Cracks and detachment were clearly observed by this method. An additional step — milling which has been shown here for the first time occurs after the detachment. The transportation mechanisms including oxide flow, penetration, pushing and metal splash are revealed for the first time. The amount of the removed oxide can be also calculated according to the real-time observation. On the other hand, these mechanisms were revealed in the context of metal-glass bonding and a further validation for metal-metal bonding shall be conducted.

The energy flow through the bonding process

The simplified energy flow can be quantified based on the studies from Chapter 4 to Chapter 6. The quantification is based on many approximations: the equivalent friction coefficient for microwelds formation, deformation & breakage was considered as a single value; the vibration amplitude of the wire at the whole length is considered to be the same. Despite of these issues, the deviation of the energy flows from real values is insignificant and the ranges of the energy flows at different mechanisms can reflect impacts of the processing parameters. The energy flow can be used to optimize the parameter setting so that the microwelds formation & breakage receive the largest amount of energy and the energy consumption is minimized. A more detailed investigation on the deleted terms of the energy flow chart will further improve the quantitative understanding of the mechanisms.

8 Conclusion and outlook

8.1 Conclusion

In this thesis, the complex phenomena during US wire bonding process including the relative motions at the two interfaces and the oxide removal process are studied. The relative motions were detected by a real-time observation system and the specific values were deduced by the automatic tracking of the mean-shift technique. The oxide removal process at the wire/substrate interface was observed by the application of a transparent glass and artificial oxide coatings. Based on the deeper understanding of these phenomena, the energy flow during the bonding process were quantified. The gained knowledge is summarized below.

Based on the real-time observation of the bonding process, it is proved that a relative motion exists at the wire/substrate interface and the wire/tool interface. The relative motions at the two interfaces are caused by both the continuous plastic deformation induced material flow and the vibration induced reciprocating motion. In general, the plastic deformation induced relative motion is enlarged throughout the bonding process unless the limit is reached before the termination of the process. As the process goes, the vibration induced relative motion at the wire/substrate interface becomes smaller and smaller since more microwelds are formed to constrain the motion of the wire. In contrast, the vibration induced relative motion at the wire/tool interface gets larger and larger until a threshold value is attained. The normal force and US power interdependently influence the relative motion. A small normal force is unable to transfer a large amount of energy to the wire and a serious vibration induced relative motion is resulted between the wire and the tool. As the normal force gets larger, more power is transferred via the wire/tool interface where the vibration induced relative motion is lowered down. When the normal force becomes too large, the vibration induced relative motion at the wire/tool interface increases again. The vibration induced relative motion at the wire/substrate interface is reversely influenced in comparison to that at the wire/tool interface. With a constant normal force, the increase of the US power leads to a large relative motion amplitude at an early time. When the US power is in the mid-range or smaller, the normal force insignificantly influence the amount of energy that is transferred to softening the wire. As the US power is at a high level, a larger normal force transfers more softening energy to the wire and results into large plastic deformation. A mid-level normal force and a mid-level US

power can be best coupled to vibrate the wire and form microwelds in the condition that the wire is not over-deformed.

It is further proved that the relative motion behavior at the wire/tool interface is similar to that at the wire/substrate interface. The behavior can be described by a combination of stick-slip model and Mindlin model. The relative motion amplitudes at different locations of the interfaces differ from each other. In general, the end contact regions receive the largest relative motion amplitude; the amplitude becomes smaller at the other peripheral regions; and the smallest amplitude occurs at the central contact region.

According to the revealed mechanism, the oxide removal process consists of four steps — the occurrence of cracks, the detachment of discretized oxides, the milling of oxide flakes and the transportation of oxide particles. The cracks are mainly caused by the normal force induced plastic deformation while the detachment is conducted by the vibration induced relative motion. After the detachment, the oxide flakes are milled into small particles under the normal force and the relative motion. At some peripheral locations, the pure metal of the wire penetrates through the oxide layer and directly contact the substrate. In the meantime, the oxides at the penetrated regions are squeezed to the surrounding areas. Due to the normal stress gradient and the vibration induced relative motion, the oxides are continuously compelled to the peripheral contact region as well as the outside of the contact. Such oxide flows can be greatly enhanced when a metal splash is formed. If an oxide layer exists on the substrate material, the continuous plastic deformation induced material flow becomes significant on removing the oxide outside of the initial contact region. During the transportation, the oxide particles agglomerate into large particles.

Due to the coexistence of many mechanisms, the energy from the transducer and the voice coil actuator flows to different aspects. The results show that most energy from the transducer is delivered to the vibration induced friction at the two interfaces and the microwelds formation and breakage at the wire/substrate interface. Despite the significance of the other mechanisms, only little amount of energy is taken up. The majority of the electrical energy to the voice coil actuator is consumed at the coils while the rest of the energy mainly flows to the bulk deformation of the wire. The processing parameters significantly influence the energy flow. Due to the increase of the cleaning coefficient as process time goes, the friction at the wire/substrate interface costs less and less energy while the consumed friction energy at the wire/tool interface keeps increasing. More energy goes to the bonding domain as the normal force or US power increases. Without a good matching of the normal force and the US power, however, more energy is converted to friction energy, especially at the wire/tool interface. In contrast, more energy can be guided to the formation of microwelds when the normal force and US power are well matched.

8.2 Outlook

It has been shown that a relative motion exists at the wire/tool interface and significantly influences the bonding process. As the tool becomes different, such a relative motion behavior might be different from that during thin wire bonding. A similar study should be performed to reveal more differences on the understanding of the two bonding processes. In addition, a further quantification of the relative motion amplitudes at different locations of the interface is beneficial to the understanding of the local changes so as a global understanding of the bonding process could be more comprehensive. Regarding the oxide removal process, the transportation route and the behavior of individual oxide particles are still unknown. The impacts of the surface hardness and roughness have not been systematically studied as well. A potential enhancement of the oxide removal process could be made by revealing these issues. A more detailed investigation on the substrate and the connection between the tool and the wire could further enhance the quantification of the energy flow.

Reference

- [1] FISCHER, A.C. ; KORVINK, J.G. ; ROXHED, N. ; STEMME, G. ; WALLRABE, U. ; NIKLAUS, F.: Unconventional applications of wire bonding create opportunities for microsystem integration. In: *Journal of Micromechanics and Microengineering* 23 (2013), pp. 083001.
- [2] HARMAN, G.G.: *Wire bonding in microelectronics*. McGraw-Hill, 2010.
- [3] SIEPE, D. ; BAYERER, R. ; ROTH, R.: The future of wire bonding is? Wire bonding! In: *Int. Conf. on Integrated Power Electronics Systems*, 2010.
- [4] ZHOU, Y.N.: *Microjoining and nanojoining*. Elsevier, 2008.
- [5] An Overview of 3D Integrated Circuits. Online available: <https://eprimes.wordpress.com/2011/09/21/an-overview-of-3d-integrated-circuits/>, last accessed: 20.07.2017.
- [6] MERKLE, L. ; SONNER, M. ; PETZOLD, M.: Lifetime prediction of thick aluminium wire bonds for mechanical cyclic loads. In: *Microelectronics Reliability* 54 (2014), pp. 417–424.
- [7] LONG, Y. ; TWIEFEL, J. ; WALLASCHEK, J.: A review on the mechanisms of ultrasonic wedge-wedge bonding. In: *Journal of Materials Processing Technology* 245 (2017), pp. 241–258.
- [8] BINA, M.H. ; JAMALI, M. ; SHAMANIAN, M. ; SABET, H.: Investigation on the resistance spot-welded austenitic/ferritic stainless steel. In: *The International Journal of Advanced Manufacturing Technology* 75 (2014), pp. 1371–1379.
- [9] SIEMENS, A.G.: Vorrichtung zum elektrischen Punktschweissen bei gleichzeitiger Einwirkung von Schall oder Ultraschall. D.E. Patent No. 748,193 (1937).
- [10] WILLRICH, H.O.: Application of ultrasonic waves. In: *Welding Journal* 18 (1950), pp. 61–66.
- [11] JONES, J.B. ; TURBETT, F.J. ; KANE, I.V.: *Exploratory Research on the Application of ultrasonics to spot welding*. Aerojects Inc. West Chester, Pa. Res. Rept. 50-5, 1950.
- [12] ANDERSON, O.L. ; CHRISTENSEN, H. ; ANDREATCH, P.: Technique for connecting electrical leads to semiconductors. In: *Journal of Applied Physics* 28 (1957), pp. 923–923.

- [13] Sonobond ultrasonics inc. Online available: <http://www.sonobondultrasonic.com>, last accessed: 12.08.2017.
- [14] COUCOULAS, A.: Ultrasonic welding of aluminum leads to tantalum thin films. In: *Transactions of the Metallurgical Society of AIME* 236 (1966).
- [15] HARMAN, G.G.: *Microelectronic ultrasonic bonding*. US National Bureau of Standards, 1974.
- [16] Hesse Mechatronics GmbH. Online available: <http://www.hesse-mechatronics.com/>, last accessed: 25.04.2018.
- [17] UTHE, P.M.: Variables affecting weld quality in ultrasonic aluminum wire bonding. In: *Solid State Technology* 12 (1969), pp. 72–77.
- [18] NEPPIRAS, E.A.: Ultrasonic welding of metals. In: *Ultrasonics* 3 (1965), pp. 128–135.
- [19] JONES, N.; Thomas J.G.; Bancroft D.: *Fundamentals of ultrasonic welding*. Aeroprojects Inc. West Chester Pa. Res. Rept. 60-91, 1960.
- [20] DANIELS, H.P.C.: Ultrasonic welding. In: *Ultrasonics* 3 (1965), pp. 190–196.
- [21] HARMAN, G.G. ; LEEDY, K.O.: An experimental model of the microelectronic ultrasonic wire bonding mechanism. In: *Reliability physics* (1972), pp. 49–56.
- [22] JOSHI, K.C.: The formation of ultrasonic bonds between metals. In: *Welding Journal* 50 (1971), pp. 840–848.
- [23] LEVINE, L.: The ultrasonic wedge bonding mechanism: Two theories converge. In: *ISHM*, 1995, pp. 242–246.
- [24] WINCHELL, V.H.I.I. ; BERG, H.: Enhancing ultrasonic bond development. In: *IEEE Transactions on Components, Hybrids, and Manufacturing Technology* 1 (1978), pp. 211–219.
- [25] OSTERWALD, F.: *Verbindungsbildung beim Ultraschall-Drahtbenden: Einfluß der Schwingungsparameter und Modellvorstellungen*. Dissertation, Technical University of Berlin, 1999.
- [26] GAUL, H. ; SCHNEIDER-RAMELOW, M. ; REICHL, H.: Analysis of the friction processes in ultrasonic wedge/wedge-bonding. In: *Microsystem technologies* 15 (2009), pp. 771–775.
- [27] TSUJINO, J. ; HASEGAWA, K. ; SONE, Y. ; NOZAKI, K.: Frequency characteristics of ultrasonic wire bonding using high frequency vibration systems of 40 kHz to 780 kHz. In: *Ultrasonics Symposium*, 1996, pp. 1021–1026.
- [28] KRZANOWSKI, J.E. ; MURDESHWAR, N.: Deformation and bonding processes in aluminum ultrasonic wire wedge bonding. In: *Journal of electronic materials* 19 (1990), pp. 919–928.

- [29] KRZANOWSKI, J.E.: A transmission electron microscopy study of ultrasonic wire bonding. In: *IEEE Transactions on Components, Hybrids, and Manufacturing Technology* (1989), pp. 450–455.
- [30] GAUL, H. ; SCHNEIDER-RAMELOW, M. ; LANG, K.D. ; REICHL, H.: Predicting the shear strength of a wire bond using laser vibration measurements. In: *Electronics Systemintegration Technology Conference*, 2006, pp. 719–725.
- [31] JI, H. ; LI, M. ; KWEON, Y. ; CHANG, W. ; WANG, C.: Observation of Ultrasonic Al-Si Wire Wedge Bond Interface Using High Resolution Transmission Electron Microscope. In: *8th International Conference on Electronic Packaging Technology*, 2007, pp. 1–4.
- [32] GEISSLER, U. ; SCHNEIDER-RAMELOW, M. ; REICHL, H.: Hardening and Softening in AlSi 1 Bond Contacts During Ultrasonic Wire Bonding. In: *IEEE Transactions on Components and Packaging Technologies* 32 (2009), pp. 794–799.
- [33] MAYER, M. ; SCHWIZER, J. ; PAUL, O. ; BOLLIGER, D. ; BALTES, H.: In situ ultrasonic stress measurements during ball bonding using integrated piezoresistive microsensors. In: *Proc. Intersociety Electron. Pack. Conf.*, 1999, pp. 973–978.
- [34] UNGER, A. ; SEXTRO, W. ; ALTHOFF, S. ; EICHWALD, P. ; MEYER, T. ; EACOCK, F. ; BRÖKELMANN, M. ; HUNSTIG, M. ; BOLOWSKI, D. ; GUTH, K.: Experimental and Numerical Simulation Study of Pre-Deformed Heavy Copper Wire Wedge Bonds. In: *International Symposium on Microelectronics*, 2014, pp. 289–294.
- [35] GAUL, U.: *Verbindungsbildung und Gefügeentwicklung beim Ultraschall-Wedge-Wedge-Bonden von AlSi1-Draht*. Dissertation, Technical University of Berlin, 2008.
- [36] SEPPANEN, H. ; KASKELA, A. ; MUSTONEN, K. ; OINONEN, M. ; HAEGGSTROM, E.: P1E-5 Understanding Ultrasound-Induced Aluminum Oxide Breakage During Wirebonding. In: *Ultrasonics Symposium*, 2007, pp. 1381–1384.
- [37] TYLECOTE, R.F.: *Solid Phase Welding of Metals*. Arnold, 1968.
- [38] EACOCK, F. ; UNGER, A. ; EICHWALD, P. ; GRYDIN, O. ; HENGSBACH, F. ; ALTHOFF, S. ; SCHAPER, M. ; GUTH, K.: Effect of different oxide layers on the ultrasonic copper wire bond process. In: *Electronic Components and Technology Conference*, 2016, pp. 2111–2118.
- [39] ALTHOFF, S. ; NEUHAUS, J. ; HEMSEL, T. ; SEXTRO, W.: Improving the bond quality of copper wire bonds using a friction model approach. In: *64th Electronic Components and Technology Conference*, 2014, pp. 1549–1555.
- [40] XU, H. ; ACOFF, V.L. ; LIU, C. ; SILBERSCHMIDT, V.V. ; CHEN, Z.: Facilitating inter-metallic formation in wire bonding by applying a pre-ultrasonic energy. In: *Microelectronic Engineering* 88 (2011), pp. 3155–3157.

- [41] DESCARTIN, A.M. ; SONG, M.J. ; LI, J. ; YAN, B.Y.: Non-continuous IMC in copper wirebonding: Key factor affecting the reliability. In: *16th International Conference on Electronic Packaging Technology*, 2015, pp. 403–407.
- [42] MINDLIN, R.D.: Compliance of elastic bodies in contact. In: *Journal of Applied Mechanics* 16 (1949), pp. 259–268.
- [43] BOWDEN, F.P. ; LEBEN, L.: The nature of sliding and the analysis of friction. In: *Proceedings of the Royal Society of London. Series A, Mathematical and Physical Sciences* (1939), pp. 371–391.
- [44] HU, C.M. ; GUO, N. ; DU, H. ; LI, W.H. ; CHEN, M.: A microslip model of the bonding process in ultrasonic wire bonders Part I: Transient response. In: *The International Journal of Advanced Manufacturing Technology* 29 (2006), pp. 860–866.
- [45] MAYER, M. ; SCHWIZER, J. ; BOLLIGER, D. ; PAUL, O. ; STEINBICHLER, J.: Active Test Chips for in situ Wire Bonding Process Characterisation. In: *Semicon Singapore* 3 (2001), pp. 17–26.
- [46] LUM, I. ; MAYER, M. ; ZHOU, Y.: Footprint study of ultrasonic wedge-bonding with aluminum wire on copper substrate. In: *Journal of electronic materials* 35 (2006), pp. 433–442.
- [47] GAUL, H. ; SHAH, A. ; MAYER, M. ; ZHOU, Y. ; SCHNEIDER-RAMELOW, M. ; REICHL, H.: The ultrasonic wedge/wedge bonding process investigated using in situ real-time amplitudes from laser vibrometer and integrated force sensor. In: *Microelectronic Engineering* 87 (2010), pp. 537–542.
- [48] MAYER, M. ; SCHWIZER, R.: Thermosonic ball bonding model based on ultrasonic friction power. In: *5th Electronics Packaging Technology Conference*, 2003, pp. 738–743.
- [49] MAYER, M. ; SCHWIZER, J.: Ultrasonic bonding: understanding how process parameters determine the strength of Au-Al bonds. In: *Proceedings-SPIE the International Society for Optical Engineering*, 2002, pp. 626–631.
- [50] GAUL, H. ; SCHNEIDER-RAMELOW, M. ; REICHL, H.: Analytic model verification of the interfacial friction power in Al us w/w bonding on Au pads. In: *IEEE Transactions on Components and Packaging Technologies* 33 (2010), pp. 607–613.
- [51] ALTHOFF, S. ; NEUHAUS, J. ; HEMSEL, T. ; SEXTRO, Walter: A friction based approach for modeling wire bonding. In: *International Symposium on Microelectronics*, 2013, pp. 208–212.
- [52] DING, Y. ; KIM, J.K. ; TONG, P.: Numerical analysis of ultrasonic wire bonding: Effects of bonding parameters on contact pressure and frictional energy. In: *Mechanics of materials* 38 (2006), pp. 11–24.
- [53] DING, Y. ; KIM, J.K.: Numerical analysis of ultrasonic wire bonding: Part 2. Effects of bonding parameters on temperature rise. In: *Microelectronics Reliability* 48 (2008), pp. 149–157.

- [54] TAKAHASHI, Y. ; SUZUKI, S. ; OHYAMA, Y. ; MAEDA, M.: Numerical analysis of interfacial deformation and temperature rise during ultrasonic Al ribbon bonding. In: *Journal of Physics: Conference Series* 379 (2012), pp. 012028.
- [55] LIU, Y. ; LIU, Y. ; KELLER, D. ; BELANI, S. ; DUBE, M.: Characterization of Al wire wedge bonding in power electronics package. In: *62nd Electronic Components and Technology Conference*, 2012, pp. 1893–1898.
- [56] KRAEMER, F. ; RITTER, P. ; WIESE, S. ; MOLLER, M.: Deformation analysis of wire bonding on soft polymers. In: *14th International Conference on Thermal, Mechanical and Multi-Physics Simulation and Experiments in Microelectronics and Microsystems*, 2013, pp. 1–7.
- [57] ZHANG, H. ; HU, M. ; ZONG, F. ; YIN, B. ; YE, D. ; HE, Q. ; WANG, Z.: Wafer damage issue study by heavy Al wire wedge bonding. In: *Microelectronics International* 31 (2014), pp. 129–136.
- [58] KRAEMER, F. ; WIESE, S.: FEM wire bonding simulation for sensor chip applications. In: *15th international conference on Thermal, mechanical and multi-physics simulation and experiments in microelectronics and microsystems*, 2014, pp. 1–6.
- [59] STORCK, H. ; LITTMANN, W. ; WALLASCHEK, J. ; MRACEK, M.: The effect of friction reduction in presence of ultrasonic vibrations and its relevance to travelling wave ultrasonic motors. In: *Ultrasonics* 40 (2002), pp. 379–383.
- [60] JIN, X.: *Microelectronic Packaging and Welding*. University of Electronic Science and Technology of China Press, 1996.
- [61] CHUANG, C.L. ; AOH, J.N. ; DIN, R.F.: Oxidation of copper pads and its influence on the quality of Au/Cu bonds during thermosonic wire bonding process. In: *Microelectronics Reliability* 46 (2006), pp. 449–458.
- [62] HARMAN, G.G. ; JOHNSON, C.E.: Wire bonding to advanced copper, low-K integrated circuits, the metal/dielectric stacks, and materials considerations. In: *IEEE Transactions on Components and Packaging Technologies* 25 (2002), pp. 677–683.
- [63] HO, H.M. ; LAM, W. ; STOUKATCH, S. ; RATCHEV, P. ; VATH, C.J. ; BEYNE, E.: Direct gold and copper wires bonding on copper. In: *Microelectronics Reliability* 43 (2003), pp. 913–923.
- [64] GROSS, D. ; HAAG, S. ; REINOLD, M. ; SCHNEIDER-RAMELOW, M. ; LANG, K.D.: Heavy copper wire-bonding on silicon chips with aluminum-passivated Cu bond-pads. In: *Microelectronic Engineering* 156 (2016), pp. 41–45.
- [65] IWAMOTO, C. ; SATONAKA, S. ; YOSHIDA, A. ; NISHINAKA, T. ; YAMADA, K.: High Resolution Transmission Electron Microscopy of Aluminum/Mo-Coated Glass Substrate Interface Bonded by Ultrasonic Wire Welding. In: *Journal of Solid Mechanics and Materials Engineering* 5 (2011), pp. 803–809.

- [66] MAEDA, M. ; KITAMORI, S. ; TAKAHASHI, Y.: Interfacial microstructure between thick aluminium wires and aluminium alloy pads formed by ultrasonic bonding. In: *Science and Technology of Welding and Joining* 18 (2013), pp. 103–107.
- [67] GEISSLER, U.: *Verbindungsbildung und Gefügeentwicklung beim Ultraschall-Wedge-Wedge-Bonden von AlSi1-Draht*. Dissertation, Technical University of Berlin, 2008.
- [68] XU, H. ; LIU, C. ; SILBERSCHMIDT, V.V. ; PRAMANA, S.S. ; WHITE, T.J. ; CHEN, Z. ; SIVAKUMAR, M. ; ACOFF, V.L.: A micromechanism study of thermosonic gold wire bonding on aluminum pad. In: *Journal of applied physics* 108 (2010), pp. 113517.
- [69] XU, H. ; LIU, C. ; SILBERSCHMIDT, V.V. ; PRAMANA, S.S. ; WHITE, T.J. ; CHEN, Z.: A re-examination of the mechanism of thermosonic copper ball bonding on aluminium metallization pads. In: *Scripta Materialia* 61 (2009), pp. 165–168.
- [70] KHATIBI, G. ; PUCHNER, S. ; WEISS, B. ; ZECHMANN, A. ; DETZEL, H.: Influence of titanium surface contamination on the reliability of Al wire bonds. In: *18th European Microelectronics and Packaging Conference*, 2011, pp. 1–7.
- [71] SCHWIZER, J. ; MAYER, M. ; BRAND, O.: *Force sensors for microelectronic packaging applications*. Springer Science & Business Media, 2006.
- [72] GAUL, H. ; SCHNEIDER-RAMELOW, M. ; REICHL, H.: FORSCHUNG & TECHNOLOGIE-Hochgeschwindigkeitsaufnahmen der Werkzeug- und Drahtschwingung beim US-Wedge/Wedge-Bonden. In: *Produktion von Leiterplatten und Systemen* 9 (2007), pp. 1529–1535.
- [73] UNGER, A. ; SEXTRO, W. ; MEYER, T. ; EICHWALD, P. ; ALTHOFF, S. ; EACOCK, F. ; BRÖKELMANN, M. ; HUNSTIG, M. ; GUTH, K.: Modeling of the stick-slip effect in heavy copper wire bonding to determine and reduce tool wear. In: *17th Electronics Packaging and Technology Conference IEEE*, 2015, pp. 1–4.
- [74] EICHWALD, P. ; SEXTRO, W. ; ALTHOFF, S. ; EACOCK, F. ; SCHNIETZ, M. ; GUTH, K. ; BRÖKELMANN, M.: Influences of bonding parameters on the tool wear for copper wire bonding. In: *15th Electronics Packaging Technology Conference IEEE*, 2013, pp. 669–672.
- [75] XU, T. ; WALKER, T. ; CHEN, R. ; FU, J. ; LUECHINGER, C.: Bond tool life improvement for large copper wire bonding. In: *17th Electronics Packaging and Technology Conference*, 2015, pp. 1–5.
- [76] BRÖKELMANN, M. ; SIEPE, D. ; HUNSTIG, M. ; MCKEOWN, M. ; OFTEBRO, K.: Copper wire bonding ready for industrial mass production. In: *International Symposium on Microelectronics*, 2015, pp. 399–405.
- [77] EICHWALD, P. ; SEXTRO, W. ; ALTHOFF, S. ; EACOCK, F. ; UNGER, A. ; MEYER, T. ; GUTH, K.: Analysis method of tool topography change and identification of wear indicators for heavy copper wire wedge bonding. In: *International Symposium on Microelectronics*, 2014, pp. 856–861.

- [78] XU, T. ; WALKER, T. ; CHEN, R. ; FU, J. ; LUECHINGER, C.: Advanced interconnect equipment and process development. In: *16th Electronics Packaging Technology Conference*, 2014, pp. 564–569.
- [79] XU, T. ; WALKER, T. ; PONCELET, B. ; FU, J. ; LUECHINGER, C.: Consumable and Process Improvement for Large Copper Wire Bonding. In: *International Symposium on Microelectronics*, 2016, pp. 445–449.
- [80] EICHWALD, P. ; UNGER, A. ; EACOCK, F. ; ALTHOFF, S. ; SEXTRO, W. ; GUTH, K. ; BRÖKELMANN, M. ; HUNSTIG, M.: Micro wear modeling in copper wire wedge bonding. In: *IEEE CPMT Symposium Japan*, 2016, pp. 21–24.
- [81] BLAHA, F. ; LANGENECKER, B.: Dehnung von zink-kristallen unter ultraschalleinwirkung. In: *Naturwissenschaften* 42 (1955), pp. 556–556.
- [82] NEVILL, G.E. ; BROTZEN, F.R.: The effect of vibrations on the static yield strength of a low-carbon steel. In: *Proceeding-American Society for Testing Material* 57 (1957), pp. 751–758.
- [83] BLAHA, F. ; LANGENECKER, B.: Plastizitätsuntersuchungen von metallkristallen in ultraschallfeld. In: *Acta Metallurgica* 7 (1959), pp. 93–100.
- [84] LANGENECKER, B.: Work hardening of zinc crystals by high-amplitude ultrasonic waves. In: *Proc. Am. Soc. Test. Mat* 62 (1962), pp. 602.
- [85] LANGENECKER, B.: Effect of sonic and ultrasonic radiation on safety factors of rockets and missiles. In: *AIAA Journal* 1 (1963), pp. 80–83.
- [86] LEBEDEV, A.B. ; BURENKOV, Y.A. ; GOLUBENKO, T.I.: Internal-friction and acoustoplastic effect in zinc single-crystals under deformation. In: *Fizika Tverdogo Tela* 35 (1993), pp. 420–430.
- [87] SAPOZHNIKOV, K.V. ; KUSTOV, S.B.: Acoustoplastic effect and amplitude-dependent internal friction during deformation of impure aluminium single crystals. In: *Le Journal de Physique IV* 6(C8) (1996), pp. 293–296.
- [88] DAUD, Y. ; LUCAS, M. ; HUANG, Z.: Modelling the effects of superimposed ultrasonic vibrations on tension and compression tests of aluminium. In: *Journal of Materials Processing Technology* 186 (2007), pp. 179–190.
- [89] DAUD, Y. ; LUCAS, M. ; HUANG, Z.: Superimposed ultrasonic oscillations in compression tests of aluminium. In: *Ultrasonics* 44 (2006), pp. e511–e515.
- [90] YAO, Z. ; KIM, G.Y. ; FAIDLEY, L. ; ZOU, Q. ; MEI, D. ; CHEN, Z.: Effects of superimposed high-frequency vibration on deformation of aluminum in micro/meso-scale upsetting. In: *Journal of Materials Processing Technology* 212 (2012), pp. 640–646.
- [91] HUANG, H. ; CHANG, B.H. ; DU, D.: Effect of superimposed ultrasound on mechanical properties of copper. In: *Materials Science and Technology* 27 (2011), pp. 1117–1122.

- [92] UNGER, A. ; SEXTRO, W. ; ALTHOFF, S. ; MEYER, T. ; NEUMANN, K. ; REINHART, R.F. ; BROEKELMANN, M. ; GUTH, K. ; BOLOWSKI, D.: Data-driven modeling of the ultrasonic softening effect for robust copper wire bonding. In: *8th International Conference on Integrated Power Systems*, 2014, pp. 1–11.
- [93] JI, H. ; LI, M. ; WANG, C.: Interfacial characterization and bonding mechanism of ultrasonic wedge bonding. In: *7th International Conference on Electronic Packaging Technology*, 2006, pp. 1–5.
- [94] MURALI, S. ; SRIKANTH, N. ; WONG, Y.M. ; VATH, C.J.: Fundamentals of thermo-sonic copper wire bonding in microelectronics packaging. In: *Journal of Materials Science* 42 (2007), pp. 615–623.
- [95] GEISSLER, U. ; FUNCK, Schneider-Ramelow M. ; ENGELMANN, H-J. ; ROOCH, I. ; MÜLLER, W.H. ; REICHL, H.: Interface formation in the US-wedge/wedge-bond process of AlSi1/CuNiAu contacts. In: *Journal of electronic materials* 40 (2011), pp. 239–246.
- [96] SEPPÄNEN, H. ; KURPPA, R. ; MERILÄINEN, A. ; HÆGGSTRÖM, E.: Real time contact resistance measurement to determine when microwelds start to form during ultrasonic wire bonding. In: *Microelectronic Engineering* 104 (2013), pp. 114–119.
- [97] GRIGORASCHWILI, J. ; SCHEEL, W. ; THIEDE, M.: Charakterisierung von Ultraschall-Schweißverbindungen durch Messen des elektrischen Durchgangswiderstands. In: *Schweißtechnik*. v34 i10 (1984), pp. 468–470.
- [98] ZHOU, Y. ; LI, X. ; NOOLU, N.J.: A footprint study of bond initiation in gold wire crescent bonding. In: *IEEE Transactions on Components and Packaging Technologies* 28 (2005), pp. 810–816.
- [99] MAEDA, M. ; YAMANE, K. ; MATSUSAKA, S. ; TAKAHASHI, Y.: Relation between Vibration of Wedge-Tool and Adhesion of Wire to Substrate during Ultrasonic Bonding. In: *Quarterly Journal of the Japan Welding Society* 27 (2009), pp. 200–203.
- [100] LI, M. ; JI, H. ; WANG, C. ; BANG, H.S. ; BANG, H.S.: Interdiffusion of Al–Ni system enhanced by ultrasonic vibration at ambient temperature. In: *Ultrasonics* 45 (2006), pp. 61–65.
- [101] SBEITI, M. ; MÜLLER, W.H. ; SCHNEIDER-RAMELOW, M. ; GEISSLER, U. ; SCHMITZ, S.: Quantifying diffusion for an ultrasonic wire bonding process by applying the theory of material forces. In: *PAMM* 12 (2012), pp. 369–370.
- [102] KULEMIN, A.B. ; MISKEVICH, A.M.: Diffusion in Metals under the Influence of Ultrasound. In: *7th International Congress on Acoustics* (1971), pp. 245.
- [103] ABRAMOV, O.V.: *Ultrasound in liquid and solid metals*. CRC press, 1994.
- [104] TAKAHASHI, Y. ; UESUGI, K.: Stress induced diffusion along adhesional contact interfaces. In: *Acta Materialia* 51 (2003), pp. 2219–2234.

- [105] LI, J.H. ; HAN, L. ; DUAN, J.A. ; ZHONG, J.: Microstructural characteristics of Au/Al bonded interfaces. In: *Materials characterization* 58 (2007), pp. 103–107.
- [106] JOHNSON, K.E.: *Interlaminar subgrain refinement in ultrasonic consolidation*. Dissertation, Olivet Nazarene University, 2008.
- [107] ZHONG, Z.W.: Overview of wire bonding using copper wire or insulated wire. In: *Microelectronics Reliability* 51 (2011), pp. 4–12.
- [108] TIAN, Y. ; WANG, C. ; LUM, I. ; MAYER, M. ; JUNG, J.P. ; ZHOU, Y.: Investigation of ultrasonic copper wire wedge bonding on Au/Ni plated Cu substrates at ambient temperature. In: *Journal of materials processing technology* 208 (2008), pp. 179–186.
- [109] JI, H. ; LI, M. ; KIM, J.M. ; KIM, D.W. ; WANG, C.: Nano features of Al/Au ultrasonic bond interface observed by high resolution transmission electron microscopy. In: *Materials Characterization* 59 (2008), pp. 1419–1424.
- [110] MÜLLER, W.H. ; SBEITI, M. ; SCHNEIDER-RAMELOW, M. ; GEISSLER, U.: Thermo-mechanical description of material diffusion during an ultrasonic wire bonding process. In: *PAMM* 11 (2011), pp. 427–428.
- [111] SBEITI, M.: *Thermomechanische Beschreibung der Ausbildung einer intermetallischen Phase beim Ultraschall-Wedge-, Wedge-Drahtbonden im Rahmen der Theorie der materiellen Kräfte*. Cuvillier, Dissertation, Technical University of Berlin, 2013.
- [112] PEDERSEN, Kristian B. ; BENNING, D. ; KRISTENSEN, P.K. ; POPOK, V.N. ; PEDERSEN, K.: Interface structure and strength of ultrasonically wedge bonded heavy aluminium wires in Si-based power modules. In: *Journal of Materials Science: Materials in Electronics* 25 (2014), pp. 2863–2871.
- [113] KHATIBI, G. ; WEISS, B. ; BERNARDI, J. ; SCHWARZ, S.: Microstructural investigation of interfacial features in Al wire bonds. In: *Journal of electronic materials* (2012), pp. 1–11.
- [114] LI, R. ; LU, S. ; KIM, D. ; SCHÖNECKER, S. ; ZHAO, J. ; KWON, S. ; VITOS, L.: Stacking fault energy of face-centered cubic metals: thermodynamic and ab initio approaches. In: *Journal of Physics: Condensed Matter* 28 (2016), pp. 395001.
- [115] GALLAGHER, P.C.J.: The influence of alloying, temperature, and related effects on the stacking fault energy. In: *Metallurgical Transactions* 1 (1970), pp. 2429–2461.
- [116] WANG, F.L. ; LI, J.H. ; LEI, H. ; ZHONG, J.: Effect of ultrasonic power on wedge bonding strength and interface microstructure. In: *Transactions of Nonferrous Metals Society of China* 17 (2007), pp. 606–611.
- [117] GAO, R.Z. ; HAN, L.: Experimental Studies of Bonding Pressure on Heavy Aluminum Wire Bonding Strength. In: *Piezoelectrics & Acoustooptics* 3 (2007), pp. 039.
- [118] WANG, F.L. ; LI, J.H. ; LEI, H. ; ZHONG, J.: Effects of ultrasonic bonding time on heavy aluminum wire wedge bonding strength. In: *Transactions of Nonferrous Metals Society of China* 27 (2007), pp. 47–51.

- [119] CHAN, Y.H. ; KIM, J.K. ; LIU, D. ; LIU, .C. ; CHEUNG, Y.M. ; NG, M.W.: Process windows for low-temperature Au wire bonding. In: *Journal of electronic materials* 33 (2004), pp. 146–155.
- [120] KAESTLE, C. ; FRANKE, J.: Comparative analysis of the process window of aluminum and copper wire bonding for power electronics applications. In: *International Conference on Electronics Packaging*, 2014, pp. 335–340.
- [121] XI, J. ; ZHANG, F.: Effect of Substrate Surface Smoothness on Thin Al Wire Wedge Bonding Strength. In: *Semiconductor Technology* 11 (2009), pp. 1070–1073.
- [122] RIBEN, AR ; SHERMAN, SL ; LAND, WV ; GEISLER, R: Microbonds for hybrid microcircuits. In: *5th Annual Symposium on the Physics of Failure in Electronics*, 1966, pp. 534–556.
- [123] ONUKI, J. ; KOIZUMI, M. ; YOSHIOKA, O.: Bonding Strength between Al-Wires and Ni-P Plated Lead Frames. In: *Materials Transactions, JIM* 34 (1993), pp. 976–981.
- [124] KHAJA, A.S. ; KAESTLE, C. ; FRANKE, J.: Reliable packaging technologies for power electronics: Diffusion soldering and heavy copper wire bonding. In: *Electric Drives Production Conference*, 2013, pp. 1–6.
- [125] JENG, Y.R. ; HORNG, J.H.: A microcontact approach for ultrasonic wire bonding in microelectronics. In: *Journal of tribology* 123 (2001), pp. 725–731.
- [126] PETZOLD, M. ; BERTHOLD, L. ; KATZER, D. ; KNOLL, H. ; MEMHARD, D. ; MEIER, P. ; LANG, K.D.: Surface oxide films on Aluminum bondpads: Influence on thermosonic wire bonding behavior and hardness. In: *Microelectronics Reliability* 40 (2000), pp. 1515–1520.
- [127] LONG, Y. ; TWIEFEL, J. ; ROTH, J. ; WALLASCHEK, J.: Real-Time Observation of Interface Relative Motion during Ultrasonic Wedge-Wedge Bonding Process. In: *International Symposium on Microelectronics*, 2015, pp. 419–424.
- [128] LONG, Y. ; SCHNEIDER, F. ; LI, C. ; HERMSDORF, J. ; TWIEFEL, J. ; WALLASCHEK, J.: Quantification of the Energy Flows During Ultrasonic Wire Bonding Under Different Process Parameters. In: *International Journal of Precision Engineering and Manufacturing-Green Technology*, 2019, <https://doi.org/10.1007/s40684-019-00061-0>.
- [129] LONG, Y. ; DENCKER, F. ; WURZ, M. ; FELDHOFF, A. ; TWIEFEL, J.: A deeper understanding on the motion behaviors of wire during ultrasonic wedge-wedge bonding process. In: *International Symposium on Microelectronics*, 2016, pp. 427–432.
- [130] ILLE, I. ; TWIEFEL, J.: Model-based feedback control of an ultrasonic transducer for ultrasonic assisted turning using a novel digital controller. In: *Physics Procedia* 70 (2015), pp. 63–67.

- [131] COMANICIU, D. ; MEER, P.: Mean shift: A robust approach toward feature space analysis. In: *IEEE Transactions on pattern analysis and machine intelligence* 24 (2002), pp. 603–619.
- [132] LONG, Y. ; DENCKER, F. ; ISAAK, A. ; LI, C. ; WURZ, M. ; TWIEFEL, J. ; WALLASCHEK, J. ; SCHNEIDER, F. ; HERMSDORF, J.: Analysis of the wire/substrate interface during ultrasonic bonding process. In: *IEEE CPMT Symposium Japan, 2017*, pp. 203–206.
- [133] LONG, Y. ; DENCKER, F. ; ISAAK, A. ; SCHNEIDER, F. ; HERMSDORF, J. ; WURZ, M. ; TWIEFEL, J.: Visualization of oxide removal during ultrasonic wire bonding process. In: *Electronics Packaging Technology Conference, 2017*, pp. 1–4.
- [134] LONG, Y. ; DENCKER, F. ; ISAAK, A. ; LI, C. ; SCHNEIDER, F. ; HERMSDORF, J. ; WURZ, M. ; TWIEFEL, J. ; WALLASCHEK, J.: Revealing of ultrasonic wire bonding mechanisms via metal-glass bonding. In: *Materials Science and Engineering: B* 236 (2018), pp. 189–196.
- [135] LONG, Y. ; DENCKER, F. ; ISAAK, A. ; HERMSDORF, J. ; WURZ, M. ; TWIEFEL, J.: Self-cleaning mechanisms in ultrasonic bonding of Al wire. In: *Journal of Materials Processing Technology* 258 (2018), pp. 58–66.
- [136] LONG, Y. ; DENCKER, F. ; SCHNEIDER, F. ; EMDE, B. ; LI, C. ; HERMSDORF, J. ; WURZ, M. ; TWIEFEL, J.: Investigations on the oxide removal mechanism during ultrasonic wedge-wedge bonding process. In: *Electronics Packaging Technology Conference, 2016*, pp. 405–410.
- [137] LANGENECKER, B.: Effects of ultrasound on deformation characteristics of metals. In: *IEEE transactions on sonics and ultrasonics* 13 (1966), pp. 1–8.
- [138] BLAU, P.J.: *Friction science and technology: from concepts to applications*. CRC press, 2008.
- [139] ANTLE, W.: Friction technique for optimum thermocompression bonds. In: *IEEE Transactions on Component Parts* 11 (1964), pp. 25–29.

Curriculum Vitae

Personal data

Name	Yangyang Long
Geburtsdatum	07.02.1988
Geburtsort	Shandong, China
Nationality	China

Career history

09/2005-07/2009	Bachelor in Mechanical Engineering at Shandong University
09/2007-07/2008	Exchange student at Harbin Institute of Technology
08/2009-08/2011	Master in Manufacturing Engineering at The University of Texas-Pan American
from 07/2013	Research assistant at Institute of Dynamics and Vibration Research, Leibniz Universität Hannover